Ultrasound-Mediated Drug Delivery: From Bubble Physics to Cancer Therapy

Sara Burnette Keller

A dissertation

submitted in partial fulfillment of the

requirements for the degree of

Doctor of Philosophy

University of Washington

2021

Reading Committee:

Mike Averkiou, Chair

Tom Matula

Matt O'Donnell

Program Authorized to Offer Degree:

Bioengineering

University of Washington

Abstract

Ultrasound Mediated Drug Delivery: From Bubble Physics to Cancer Therapy

Sara Burnette Keller

Chair of the Supervisory Committee:

Mike Averkiou

Department of Bioengineering

Beyond diagnostic imaging and contrast-enhanced ultrasound, microbubbles have shown immense promise in the field of drug delivery. In this work, we present several investigations of how ultrasound and microbubble physics may be exploited for imaging and therapy. We begin with an introduction on the challenges of drug delivery for cancer and how microbubble cavitation behavior may be exploited as a therapeutic strategy for overcoming these barriers (**Chapter 1**). We then describe how inertial cavitation, which is critical in many therapeutic applications of ultrasound, may be visualized in real-time with a clinical ultrasound scanner (**Chapter 2**). We then present evidence that unique microbubble nonlinear dynamics can produce a phase response that can be used to improve contrast imaging (**Chapter 3**). We then show a study of microbubble diffusion and destruction during therapeutic pulsing schemes in a common *in vitro* setup (**Chapter 4**). These above results present the building blocks to study ultrasound-mediated drug delivery *in vivo* using a clinical ultrasound scanner to evaluate efficacy in a murine model of hepatocellular carcinoma (**Chapter 5**) and safety in a healthy porcine model (**Chapter 6**). We conclude with a summary of the accomplishments and future directions of this work (**Chapter 7**).

TABLE OF CONTENTS

LIST OF FIGURES

LIST OF TABLES

ACKNOWLEGEMENTS

This work was supported by a grant from the US Department of Defense (CA160415/PRCRP) and TL1 TR002318. All acknowledgements to individuals are included following their respective chapters.

I am foremost grateful to my advisor, **Mike Averkiou**, for being a ceaselessly excited, endlessly interested, and constantly supportive mentor. You have taught me the value of hard work, attention to detail (in experiments and lab organization), and scientific integrity. I chose to come to UW to work for you, because I could tell you were a hands-on mentor who cared about his students. I am so glad to have made that decision. I would also like to thank my Supervisory Committee: **Tom Matula**, **Matt O'Donnell**, and **Lilo Pozzo** for their helpful insights throughout this process.

Of course, the path to a PhD is not just limited to what happens in the committee. I have been shaped by the relationships that I have forged during my time at UW. I am specifically grateful to the following people:

To my first real mentor at Vanderbilt who started me on this path, **Amanda Buck,** for treating me like an equal even as I was just beginning my research career. You taught me to never undervalue my own scientific worth.

To my earliest mentors at UW, **Ine De Cock**, **Richard Zong,** and **David Li**, for welcoming me into the 5-year long Ben Hall party and for helping me find my feet in the lab. Similarly, thank you to **Matt Bruce** for your research and career advice as well as your wealth of digital signal processing and imaging knowledge.

To my collaborator and mentor **Yak-Nam Wang** for inspiring me not only to become a better scientist but, more importantly, a more ultralight backpacker. I am so grateful for your guidance (and tolerance of my many, *many* questions) and it is fair to say that I could not have accomplished much of the work in this thesis without you. Thank you also to collaborators **Heidi Kenerson** and **Raymond Yeung**, who provided useful guidance and critique on the biological aspects of my work.

To my lab mates **Ting-Yu Lai**, **Eric Juang**, **Alicia Clark**, **Dingjie Suo**, and the rest of the **Averkiou Lab** for your support and comradery through the years. You have been wonderful scientists to learn and grow (and gripe) with.

To my Seattle friends too numerous to name for continually inspiring me to push myself to ever increasing heights (like, say, 14,411 ft…). I am very grateful to have found a surrogate family through all of you. Our trips to breweries, alpine lakes, music festivals, volcanoes, hot springs, etc. etc. ad nauseum made graduate school the best five years of my life so far (really).

To my (in order of importance) housemate, friend, and co-cat parent, **Meilyn Sylvestre**, for your open ears and your compassion. I am lucky to have found someone to share this journey with and you have inspired me to be both a more dedicated scientist and a more empathetic friend. A secondary thank you to our cat **Eleanor Sylvestre-Keller** for the cuddles.

To my brother **Ryan** for showing me what it means to have humble intelligence and calm competency. I am grateful to have you as a role model and a friend.

To my grandma **Edith** for always cheering me on. I am so fortunate to have had you be such a big presence in my life, and I feel like now is as good a time as any to thank you for all the rides home from school when I really should have just walked.

To my partner **David Peeler** for your unquestioning confidence in me as a scientist and as a human. You have inspired me to reach for a future I had trouble believing I was worthy of having. My life is better with you in it.

Finally, to my mother **Gina** and my father **Mark** for their love and support throughout my life and during my PhD. You provided the model for who I wanted to (and have, I hope) become.

DEDICATION

To the original Dr. Keller (Frederick, that is):
Sorry, you are not the only one now.

Chapter 1. ULTRASOUND-MEDIATED DRUG DELIVERY: FROM BUBBLE PHYSICS TO CANCER THERAPY

Abstract

Cancer is the second leading cause of death in the United States, which represents an enormous healthcare burden. One barrier towards effective cancer treatment can be attributed to the difficulties imposed by the tumor microenvironment, including irregular vascular geometries, high interstitial fluid pressure, and immunosuppressive cell populations. Ultrasound and microbubbles are currently under investigation as drug delivery vehicles and vascular modulation agents. Briefly, under an ultrasound field, microbubbles oscillate, which can provide signal for contrast enhancement in imaging as well as microscale forces suitable for treatment options. In this chapter, the background and barriers of cancer treatments for solid tumors, in addition to several methods in which ultrasound with or without microbubbles can be used to overcome them, will be covered. Additionally, the overall research aim of the project will be presented.

1.1 CHALLENGE OF DELIVERING THERAPEUTICS TO SOLID TUMORS

1.1.1 *Global burden of cancer*

According to the Center for Disease Control, cancer is the second leading causes of death in the United States [1], and cancer incidence and mortality are rapidly growing, in part due to increased life expectancy. By 2030, it is anticipated that the cancer incidence rate in the United States will be 2.3 million, many of whom will be elderly Americans and minorities [2]. This presents an enormous economic burden; it was expected that the total financial costs of cancer would rise to 158 billion dollars by 2020, which represents a 29% increase from 2010 [3].

While the overall 5-year survival rate of a cancer diagnosis is nearly 70% [4], certain types of cancer have much worse clinical outcome, such as pancreatic cancer and liver cancer, which have 5-year survival rates of 10% [5] and 20% [6], respectively. One major challenge to effective treatment of these cancers is that the chemotherapy dosages needed to effectively eradicate cancerous tissue can be toxic to non-cancerous tissue. The harsh and painful side effects of

chemotherapy plainly motivate the need for a more targeted therapy that can increase local efficacy and minimize systemic damage.

1.1.2 *The tumor microenvironment as a barrier to drug delivery*

Over 85% of cancer mortalities are due to solid tumors [7], which have a unique microenvironment that constitutes a major barrier to drug delivery. In general, cancer therapeutics are introduced into the body systemically/intravenously. Getting drugs to the correct cells is therefore a multistep process: first, the drug must traverse the vasculature to the tumor; second, the drug must extravasate beyond blood vessel walls; and third, it must travel across the interstitial space to reach the cells of interest [8]. Although many cancer therapeutics are small molecule drugs that are readily able to diffuse beyond the vasculature and into cells, the cancer biology of solid tumors can still limit effective therapeutic delivery, especially when novel, larger drugs or biologics are considered [8].

The connective tissue in the body is composed of interstitial fluid and the extracellular matrix (ECM) [9]. The ECM consists of a collagen framework, glycosaminoglycans to form a hydrophilic gel, and other key proteins, including elastin and plasma proteins [10]. Collectively, the purpose of the ECM is to provide structural support for organs and cells. In solid tumors, the ECM tends to be highly desmoplastic, characterized by fibrosis and excessive collagen, which is associated with poor clinical prognosis [11]. In addition to the abnormalities in the ECM, blood vessels within tumors tend to be “leaky”, due to the enhanced permeability and retention (EPR) effect [12], and there is poor lymphatic drainage [13]. These vascular abnormalities combined with dense stromal deposition within the ECM results in increased fluid diffusion into the tumor but reduced drainage out of the tumor [14]. This leads to an elevated interstitial fluid pressure (IFP) within the tumor that limits overall penetration and effectiveness of drugs [8] (**Fig. 1.1**).

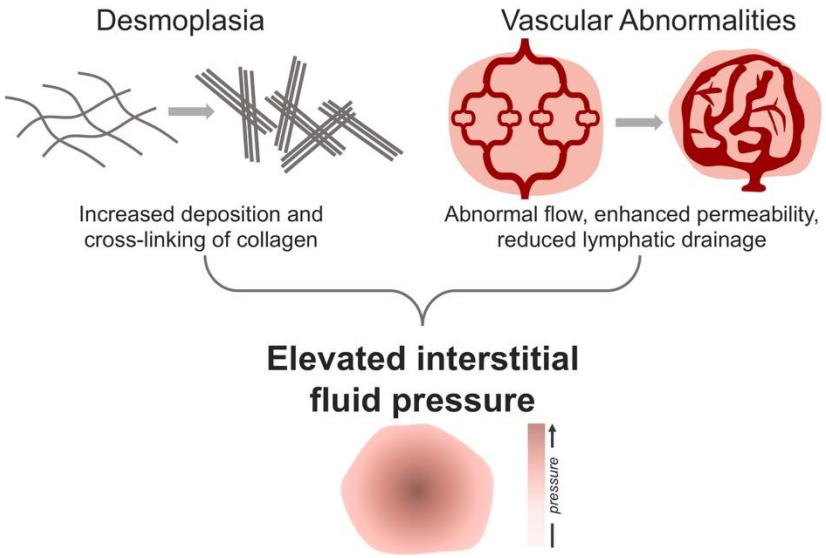

Fig. 1.1: The tumor microenvironment hinders effective drug delivery.

Desmoplasia (growth of fibrotic tissue) combined with vascular anomalies, including enhanced permeability with limited drainage, leads to an elevated interstitial fluid pressure within solid tumors. Elevated interstitial fluid pressure is a barrier to effective drug delivery

1.1.3 *Current strategies to treat solid tumors*

Because of the difficulties associated with the tumor microenvironment, alternate strategies have been proposed to enhance the efficacy of chemotherapy by targeting the ECM or the vasculature. These can include anti-angiogenic treatments, vascular disrupting agents, and novel repurposing of antihistamines or anti-inflammatories. These have all been performed with the intent of "normalization" or remodeling of the ECM and vasculature to have a more consistent blood supply network to aid drug delivery [15]. Furthermore, methods to alleviate interstitial fluid pressure and stress on the tumor vasculature may also augment chemotherapy delivery [16].

1.1.3.1 Anti-angiogenic treatments

Several strategies have been proposed to eradicate cancer cells within solid tumors by targeting the vasculature. Given that many tumors are hypervascular and angiogenic in nature, one therapeutic strategy is to limit the ability of a tumor to form new blood vessels in order to stop the growth of a tumor [17]. Clinically, this strategy has been combined with chemotherapy to destroy two aspects of cancer: the cancer cells themselves and the proliferation of new blood vessels [18].

Anti-angiogenic drugs are most commonly vascular endothelial growth factor (VEGF) inhibitors, which bind to the VEGF receptor and interfere with blood vessel formation [19]. However, a reduction in tumor blood flow can also yield less effective drug delivery in some cases [20]. Therefore, the timing regimen of combining antiangiogenics and chemotherapeutics must be optimized in such a way that they are able to provide a synergistic effect [21].

1.1.3.2 Vascular disrupting agents

Another strategy is to "starve" the tumor of blood supply. Small-molecule vascular disruption agents (VDAs), such as combrestatin A-4 phosphate (CA4P) and 5, 6-dimethylxanthenone-4-acetic acid (DMXAA) have been proposed to treat highly angiogenic tumors due to their ability to cause selective shutdown of the vasculature within tumors [22], [23]. However, similar to liberal and/or ill-timed use of antiangiogenic agents, VDAs can compromise the ability of drugs to penetrate through tumors. Even more problematic, vascular disruption can be ineffective at eliminating the highly proliferative outer rim of tumors, and remaining cells tend to be more aggressive and chemoresistant which can lead to a greater likelihood of recurrence and metastasis [24].

1.1.3.3 Repurposing of drugs for mechanical modulation

Recently, new methods of "mechanical modulation" of the tumor microenvironment have been proposed. These may include antihistamines [25], anti-hypertensives [26], or anti-inflammatory drugs, such as dexamethasone [27]. The purpose behind these "mechanotherapies" is to reduce interstitial and solid stresses within tumors that arise as a result of stromal deposition. This normalization of the stroma can reduce compression on tumor microvessels in order to enhance blood flow in tumors to aid normalization efforts [28]. Mechanotherapy using blood vessel or stroma normalization has been shown to have clinical efficacy when administered along with chemotherapy [29].

However, all techniques previously mentioned are generally not targeted to tumor tissue and also take a variable amount of time to take effect [13]. Ultrasound-based methods of modulating the tumor microenvironment are an attractive alternative, as ultrasound is non-invasive, targeted, can be combined with real-time image guidance, and can produce a biological effect within a short timeframe, rendering drug dosing and timing much easier to manage [30]–[33].

1.2 MICROBUBBLES: ACOUSTIC CONTRAST AGENTS

While it was known that ultrasound could spontaneously induce the creation of cavitation nuclei that generated nonlinear echoes [34], it was not until 1968 that Gramiak and Shah discovered that micro-scale bubbles could be used as a source of ultrasound contrast [35]. The first FDA approved ultrasound contrast agent still used micro-scale bubbles as the source of signal contrast, but stabilized by an albumin shell, called Albunex [36]. Since then, the field of contrast-enhanced ultrasound has advanced in the development of novel contrast agents [37], microbubble imaging methods [38], and drug delivery [39]. Microbubbles are a blood pool agent since they are similar in size to red blood cells which allows them to provide contrast enhancement in capillaries and microvessels, both of which are smaller than the resolution of standard ultrasound scanners. Therefore, microbubbles are able to provide micrometer sensitivity, if not micrometer resolution, and are an excellent diagnostic tool for observing real-time blood perfusion.

1.2.1 *Microbubble and nanodroplet formulations*

Microbubble contrast agents that are approved for clinical use consist of an inert (generally a perfluorocarbon) gas surrounded by a stabilizing layer of a lipid, protein or polymer shell. The most common clinical microbubbles are Definity (Lantheus Medical Imaging), Sonazoid (GE Healthcare), SonoVue which is marketed in the US as Lumason (Bracco Suisse), and Optison (GE Healthcare). Definity, Sonazoid and SonoVue have a phospholipid shell, while Optison has a protein shell composed of human serum albumin. All have an average radius between 1-10 μm, but exist as polydisperse solutions, so standard deviations in size may vary widely. Beyond commercial formulations, microbubbles can also be easily made by dissolving the lipid shell components in a solvent, introducing the gas that comprises the core, and sonicating, or shaking the mixture until bubbles are formed [40]. The simplicity of formulation has allowed many variants in composition, including drug-loaded and/or receptor targeted microbubbles [41], [42].

There have also been recent innovations in the development of novel contrast agents that are under investigation for their acoustic as well as their therapeutic properties. Among these include phase change contrast agents, or nanodroplets. Microbubbles are confined to systemic circulation due to their size, which make them useful for microvascular imaging but limits their ability to directly

extravasate beyond blood vessels. Nanodroplets, which are microbubbles condensed to their liquid phase, have been designed to combat these size limitations [43], [44]. They are an order of magnitude smaller than microbubbles and are therefore able to diffuse past endothelial barriers and are also more stable in circulation. Other novel contrast agents include genetically encoded gas vesicles, first published by Shapiro et al. in 2014, which can be utilized as "reporter genes" similar to GFP or luciferase in microbiology applications [45], [46].

1.2.2 *Cavitation dynamics of microbubbles during imaging*

In the presence of an acoustic wave, microbubbles undergo volumetric oscillations that provide signal for contrast enhancement or microscale mechanical forces for therapy [47]. When the driving pressure is higher than ambient pressure, the microbubble contracts, whereas when the driving pressure is lower than ambient pressure, the microbubble expands [48]. Ultrasound imaging typically utilizes acoustic pressures between 0-1 MPa and short pulse durations. Under standard imaging regimes, microbubbles scatter the transmitted frequency (f_0) as well as harmonics of the transmitted frequency ($n*f_0$, where n is an integer). Microbubbles are therefore considered nonlinear scatterers, as they have frequency emissions that are distinct from the ultrasound parameters that excite them.

The phenomenon in which higher pressure excitation results in a greater nonlinear response is known as amplitude-dependent nonlinearity, and can be used a source of microbubble contrast [49]. When microbubbles are used for imaging as a contrast agent, nonlinear pulsing schemes have been developed to exploit these properties of microbubbles in order to isolate specific frequency components (generally the second harmonic) for creating images solely of the microbubbles [38]. Traditionally, these include pulse inversion, power (or amplitude) modulation, or some combination thereof (**Fig. 1.2**). Since at low ultrasound pressures, tissue is unlikely to generate sufficiently high harmonic signals to be detectable by ultrasound scanners, these pulsing schemes are able to accentuate just microbubble signal, and null out tissue signal. Therefore, contrast enhanced ultrasound is most often used clinically for evaluation of microvascular perfusion. It should be noted that at high ultrasound pressures (still within FDA limits for imaging), nonlinear propagation of sound in tissue results in the generation of harmonics due to distortion of the sound

wave. These harmonics can be utilized for imaging in a mode called tissue harmonic imaging (THI) [50]; however, the tissue nonlinear signals can result in incomplete tissue cancellation and act as noise during contrast imaging [51]. Later in this thesis we show that microbubble contrast may be further enhanced by an amplitude dependent difference in phase [51]. Utilizing phase difference to segment bubbles from tissue can therefore be implemented as an additional method of tissue suppression, which can generate higher contrast in CEUS imaging [51], as AM sequences in tissue are again not expected to result in the same degree of phase change. We will investigate the phase response of microbubbles and tissue for phase segmentation further in **Chapter 3**.

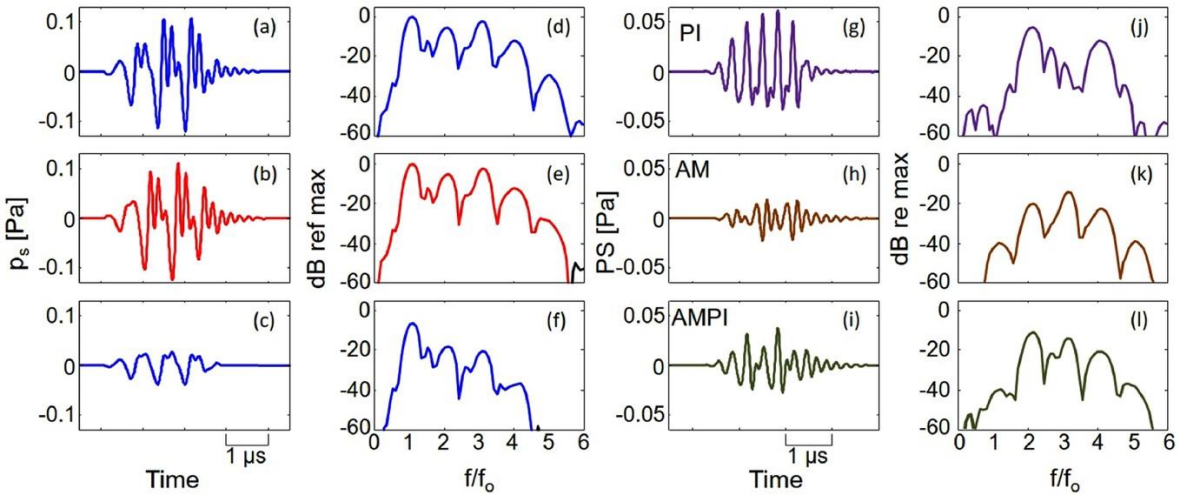

Fig. 1.2: Microbubble pulsing schemes.

Process of pulse inversion (PI) (g), amplitude modulation (AM) (h) and amplitude-modulated pulse inversion (AMPI) (i) from simulated microbubble echoes (a-c). In pulse inversion, a pulse and an inverted form of that pulse are used to insonify the imaging line. In power modulation, a full pulse and two half pulses are used to insonify the imaging line. Finally, in amplitude modulated pulse inversion, an inverted full pulse and two half pulses are used to insonify the imaging line. These imaging schemes result in isolation of the nonlinear components of microbubble signal. Figure reprinted from [38] with permission.

1.2.3 *Cavitation dynamics for therapeutic ultrasound*

At low excitation pressures, microbubbles undergo linear oscillation, in which they emit the fundamental frequency (f_0) and harmonics ($n*f_0$, where n is an integer). In general, this is what is used for contrast-enhanced ultrasound imaging. At higher ultrasound pressures, microbubble behavior is usually classified into either stable or inertial cavitation. Stable cavitation is defined

by the presence of sub- and ultraharmonics (f_0/n or $n/2*f_0$, respectively, where n is an integer), while inertial cavitation is defined by the onset of broadband noise, or signal that contains many frequencies. Types of cavitation and their corresponding frequency spectra may be seen in **Fig. 1.3**.

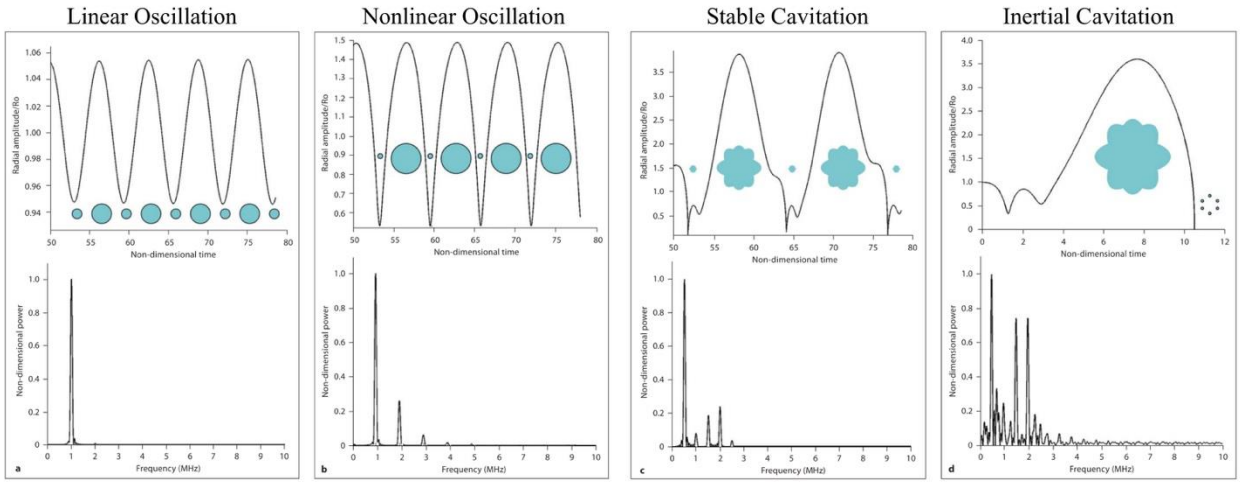

Fig. 1.3: Frequency response of microbubble emissions.

Linear oscillations scatter only the fundamental frequency. Nonlinear oscillations (used for contrast imaging) scatter the fundamental frequency and its harmonics. Stable cavitation emits sub- and ultraharmonics, and inertial cavitation emits broadband noise. Figure reprinted from [48] with permission from the publisher, S. Karger AG, Basel.

There are other physical phenomena that are important when considering therapeutic ultrasound, including: radiation (Bjerknes) force, microstreaming, microjetting, inertial collapse, and thermal effects [48]. Primary and secondary radiation force induce microbubble translation in the path of the ultrasound beam, and may be used as a method of guiding, or targeting microbubbles to a certain location [52]. Microstreaming and microjetting are both a result of a microbubble changing conformation near a wall (ie, a cell membrane), and can induce shear stresses or high velocity jetting that may have a variety of wanted [53] or unwanted [54] effects. Sufficiently high amplitudes may cause inertial collapse, in which a microbubble implodes, generating shock waves that may be damaging to the surrounding area. Finally, microbubble cavitation has shown to elevate temperature within tissues through thermoviscous absorption [55], [56], which could be used as a method of mild hyperthermia or as a catalyst for heat sensitive materials.

1.2.4 *Cavitation detection*

Given that microbubbles emit distinct frequency signatures when undergoing linear oscillation, stable cavitation, or inertial cavitation, frequency-dependent cavitation imaging has become an important component of real-time therapy monitoring. By tracking specific frequency features, ie, sub- and ultraharmonics for stable cavitation, and broadband noise for inertial cavitation, unintended harmful biological effects can possibly be avoided, and intended ablative effects can be enhanced. While currently cavitation detection is performed using either single-element ultrasound transducers for passive cavitation detection (ie, solely receiving scattered microbubble echoes) [57], [58], which have excellent temporal resolution but lack spatial resolution, recent work in this area has sought to map where the cavitation activity occurs in real time through novel beamforming approaches on research scanners [59], [60]. Unfortunately, both of these methods are difficult to implement in clinical scenarios, due to bulky hardware and lack of FDA approval. We therefore introduce an alternative method of cavitation detection in **Chapter 2**, in which a clinical ultrasound transducer was modified to observe inertial cavitation in real time [61]. This work provides an excellent opportunity to perform therapy monitoring with tools readily available in the clinic.

1.2.5 *Super-resolution imaging*

As mentioned above, microbubbles are able to generate micrometer sensitivity but generally not micrometer resolution. This is because ultrasound resolution is limited to half the duration of the transmitted ultrasound pulse [62]. However, recent advances in ultrafast imaging and image reconstruction have enabled imaging beyond this resolution limit. Super-resolution ultrasound imaging involves detection, localization, tracking, and ultimately mapping of microbubbles within microvessels [63]. This has resulted in extremely high-resolution maps of the vasculature within the brain [64], kidneys [65], and tumors [66], and has promising future applications in oncology and neurology.

1.3 BIOLOGICAL EFFECTS OF ULTRASOUND CAVITATION IN THE PRESENCE OF MICROBUBBLES

1.3.1 *Sonoporation*

One of the first explorations into using microbubbles as drug delivery vehicles was in 1997, when Bao, et. al used ultrasound in combination with Albunex to transfect luciferase into cells [67]. The physical mechanism was named 'sonoporation' or the use of sound to transiently permeate cell membranes. The principle behind sonoporation is that, as a microbubble expands and contracts, it generates forces, due to microstreaming or microjetting for example, that are able to disrupt cell membrane integrity. Cells have developed complex mechanisms to keep undesirable materials from entering; including channels for specific materials, as well as the endolysosomal pathway that shuttles macromolecules directly into the lysosome to be degraded. Due to the growing relevancy of delivering macromolecular therapeutics directly into cells, including proteins [68] and nucleic acids [69], the ability to physically disrupt cell membranes is therefore of high value. This technique has been extensively studied, both on cancer cells [40] and endothelial cells [54], [70]. However, by definition, sonoporation requires microbubbles to be oscillating next to the cells they intend to permeate. Due to the size limitations of microbubbles, they will generally only interact with endothelial cells, not necessarily cancer or diseased cells. While this might be useful for enhancing transcytosis, macromolecule delivery such as gene delivery requires direct cell permeation. Therefore, despite the wide variety of literature available on the topic of single cell sonoporation *in vitro*, it is somewhat unlikely that these mechanisms translate to the *in vivo* scenario, although it could be argued that many cancerous tumors (including hepatocellular carcinoma studied in **Chapter 5**) can occasionally have cancer cells lining blood vessel walls [71]. Furthermore, *in vitro* sonoporation relies on test setups that result in complex acoustic environments, which can further complicate full understanding of *in vivo* mechanisms. This is discussed more in depth in **Chapter 3**. Methods of microbubble-mediated bioeffects may be seen in **Fig. 1.4**.

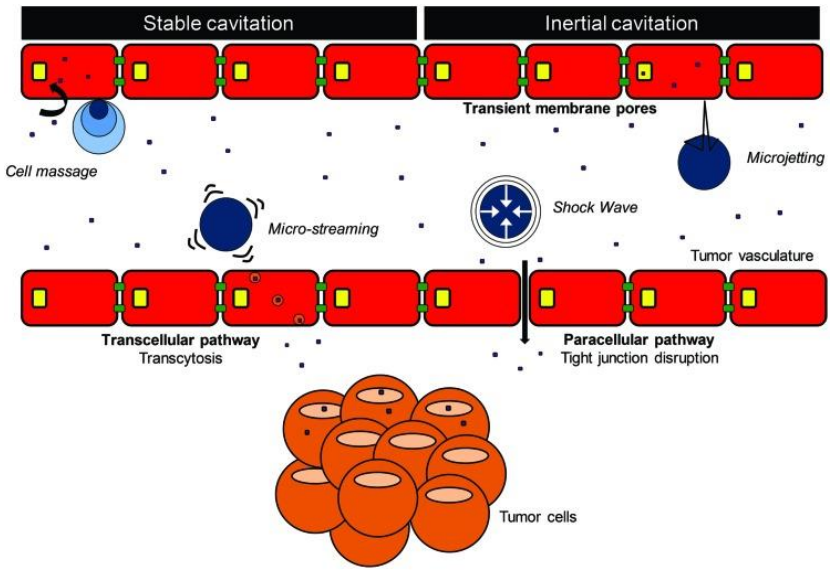

Fig. 1.4: The bioeffects of ultrasound and microbubbles.

Inertial cavitation generally results in more dramatic effects. Figure reprinted from [72] under the terms of the Creative Commons Attribution (CC BY) License.

1.3.2 *Drug penetration*

On a macroscopic level, enhanced drug penetration beyond vessel walls has been observed in preclinical *in vivo* studies of ultrasound-mediated drug delivery. It is hypothesized that through mechanical and/or thermal mechanisms, ultrasound and microbubbles may enhance vascular permeability and extravasation beyond vessel boundaries [30]. Several prior studies have shown enhanced chemotherapy delivery to solid tumors following treatment with ultrasound and microbubbles, including with Docetaxel [58] and in a Phase I clinical trial with Gemcitibine [73]. However, due to the physiology of solid tumors, including abnormal vascular geometries and high interstitial pressure, the ability to delivery drugs to the tumor core can be much more difficult than the tumor rim [74]. It is hypothesized, therefore, that the results observed from these studies are likely in combination with some type of interaction with the extracellular matrix.

1.3.3 *Modulation of the extracellular matrix and vasculature*

Although sonoporation and drug extravasation continue to be active areas of research, studies using realistic tumor models have shown that ultrasound may interact directly more with the tumor microenvironment (ECM and vasculature) than individual cancer cells or blood vessels [58], [75], [76]. It has recently been hypothesized that microbubbles may play a role in modulating the tumor

ECM which aids drug penetration [77]. It has been shown that use of ultrasound and microbubbles yields a reduction in tumor IFP with moderate acoustic pressures between 3-5 MPa , ultrasound frequencies between 1-3 MHz, and low duty cycles [78], [79], although the mechanism remains to be elucidated. No studies utilizing microbubbles show an obvious reduction in collagen content observed through histology [78], [79]. It is possible that the same microscale pore formations may be occurring within the collagen matrix, although more studies would be required to confirm this hypothesis. Regardless, the mechanism is thought to be primarily mechanical. Although literature exists on microbubble-enhanced hyperthermia [80]–[82], it is generally inefficient because the high microbubble concentrations required to cause heating also yield significant pressure attenuation [82], [83]. That being said, mild heating has been shown previously to be an effective catalyst for heat-sensitive materials, including thermosensitive liposomes [84]–[87] or magnetic nanoparticles [88], and can be a highly effective form of local drug release in tumors.

There is a slightly wider variety of work showing a contradictory reduction in tumor microvascular flow with simultaneous enhanced drug penetration following treatment with focused ultrasound, microbubbles, and a systemically delivered drug [33], [58], [89]. In general, these results occur in the absence of any other histological explanation [90]. These opposing outcomes are partially explained by heterogeneity in vessel sizes: mechanical cavitation in smaller, immature vessels is more likely to result in vascular disruption [91], while mechanical cavitation in larger vessels is more likely to result in greater drug penetration distances [89]. When taken in combination with the observations that focused ultrasound and microbubbles lower tumor IFP [78], [79], it seems possible that these mechanisms may act synergistically. Indeed, the studies that observed a reduction in IFP also observed vascular disruption [79] and/or drug penetration [78]. Both the selective depletion (“pruning”) of the immature vasculature and a reduction in IFP could return the tumor to a more “normalized”, and therefore more bioaccessable, phenotype [7].

With the advent of super-resolution contrast imaging as mentioned above [64], it may be possible to further investigate this vascular selectivity using imaging techniques. It is possible to separate vessels within a region based on their blood velocity using high frequency ultrasound and novel Doppler processing [92]. This could help confirm on the whole-tumor scale which vessels are more

sensitive to the effects of ultrasound and microbubbles. In addition to IFP measurements and histology, a clearer picture of mechanism might be possible.

1.4 RESEARCH OBJECTIVES

Overall, ultrasound poses high promise for diagnosis and treatment of cancer. The objectives of this work cover all aspects of image-guided therapy with ultrasound from diagnostic imaging to treatment and therapy monitoring. We first seek to investigate microbubble behavior during treatment in order to improve real-time cavitation monitoring and optimize therapeutic ultrasound parameters. Secondly, we aim to understand microbubble dynamics during imaging in order to develop methods of improving imaging contrast and ultimately diagnostic potential. Finally, we aim to utilize these optimized cavitation dynamics to implement treatment ultrasound protocols *in vivo* in both an efficacy study in mice and a safety study in pigs. Understanding how microbubble dynamics can affect biological outcomes could elucidate new techniques and broader mechanistic insight into their therapeutic efficacy. A secondary goal is to utilize mostly clinically available tools and reagents for both imaging and therapy. We believe that an adaptation of commercial equipment for image-guided therapy, along with a strong knowledge of the connection between physical phenomena and biological response, could help pave the way for clinical translation of this technique.

1.5 SUMMARY

The physiology of solid tumors, including abnormal blood vessels, high interstitial fluid pressure, and immunosuppressive cell populations, make them a difficult target for therapy. Ultrasound-mediated microbubble cavitation can be effectively exploited as a method of targeting drugs to solid tumors and improving drug efficacy and consequently therapy outcomes. Microbubbles can also generate microscale forces at high excitation pressures beyond scattering nonlinear echoes for contrast at low excitation pressures. These forces may be used to improve drug delivery and to modulate the extracellular matrix and tumor vasculature. Furthermore, microbubbles are noninvasively activated and can selectively target small, abnormal vessels within tumors. The use of focused ultrasound and microbubbles is therefore a promising technique that could have broad clinical applications in the field of cancer therapy.

1.6 REFERENCES

[1] "An Update on Cancer Deaths in the United States | CDC." [Online]. Available: https://www.cdc.gov/cancer/dcpc/research/update-on-cancer-deaths/index.htm. [Accessed: 12-Aug-2021].

[2] B. D. Smith, G. L. Smith, A. Hurria, G. N. Hortobagyi, and T. A. Buchholz, "Future of Cancer Incidence in the United States: Burdens Upon an Aging, Changing Nation," *J Clin Oncol*, vol. 27, pp. 2758–2765.

[3] A. B. Mariotto, K. R. Yabroff, Y. Shao, E. J. Feuer, and M. L. Brown, "Projections of the cost of cancer care in the United States: 2010-2020.," *J. Natl. Cancer Inst.*, vol. 103, no. 2, pp. 117–28, Jan. 2011.

[4] "Cancer of Any Site — Cancer Stat Facts." [Online]. Available: https://seer.cancer.gov/statfacts/html/all.html. [Accessed: 18-Jun-2020].

[5] "Pancreatic Cancer — Cancer Stat Facts." [Online]. Available: https://seer.cancer.gov/statfacts/html/pancreas.html. [Accessed: 18-Jun-2020].

[6] "Liver and Intrahepatic Bile Duct Cancer — Cancer Stat Facts." [Online]. Available: https://seer.cancer.gov/statfacts/html/livibd.html. [Accessed: 18-Jun-2020].

[7] R. K. Jain, "Normalization of Tumor Vasculature: An Emerging Concept in Antiangiogenic Therapy," *Science (80-.).*, vol. 307, no. 5706, pp. 58–62, Jan. 2005.

[8] R. K. Jain and T. Stylianopoulos, *Delivering nanomedicine to solid tumors*, vol. 7, no. 11. Nature Publishing Group, 2010, pp. 653–664.

[9] E. Sassaroli and B. E. O'Neill, "Modulation of the interstitial fluid pressure by high intensity focused ultrasound as a way to alter local fluid and solute movement: Insights from a mathematical model," *Phys. Med. Biol.*, vol. 59, no. 22, pp. 6775–6795, Nov. 2014.

[10] K. Aukland and R. K. Reed, "Interstitial-Lymphatic Mechanisms in the Control of Extracellular Fluid Volume," 1993.

[11] E. Henke, R. Nandigama, and S. Ergün, "Extracellular Matrix in the Tumor Microenvironment and Its Impact on Cancer Therapy," *Frontiers in Molecular Biosciences*, vol. 6. Frontiers Media S.A., p. 160, 31-Jan-2020.

[12] H. Maeda, J. Wu, T. Sawa, Y. Matsumura, and K. Hori, "Tumor vascular permeability and the EPR effect in macromolecular therapeutics: A review," *J. Control. Release*, vol. 65, no. 1–2, pp. 271–284, Mar. 2000.

[13] C.-H. Heldin, K. Rubin, K. Pietras, and A. Östman, "High interstitial fluid pressure — an obstacle in cancer therapy," *Nat. Rev. Cancer 2004 410*, vol. 4, no. 10, pp. 806–813, 2004.

[14] T. Stylianopoulos, L. L. Munn, and R. K. Jain, "Reengineering the Physical Microenvironment of Tumors to Improve Drug Delivery and Efficacy: From Mathematical Modeling to Bench to Bedside," *TRENDS in CANCER*, vol. 4, pp. 292–319, 2018.

[15] P. Carmeliet and R. K. Jain, "Principles and mechanisms of vessel normalization for cancer and other angiogenic diseases," *Nat. Rev. Drug Discov.*, vol. 10, no. 6, pp. 417–427, Jun. 2011.

[16] R. K. Jain, J. D. Martin, and T. Stylianopoulos, "The role of mechanical forces in tumor growth and therapy," *Annu. Rev. Biomed. Eng.*, vol. 16, p. 321, 2014.

[17] K. Liu *et al.*, "Targeting the vasculature in hepatocellular carcinoma treatment: Starving versus normalizing blood supply.," *Clin. Transl. Gastroenterol.*, vol. 8, no. 6, p. e98, Jun.

2017.
[18] B. A. Teicher, “A systems approach to cancer therapy,” *Cancer Metastasis Rev.*, vol. 15, no. 2, pp. 247–272, Jun. 1996.
[19] N. Ferrara, K. J. Hillan, H.-P. Gerber, and W. Novotny, “Discovery and development of bevacizumab, an anti-VEGF antibody for treating cancer,” *Nat. Rev. Drug Discov.*, vol. 3, no. 5, pp. 391–400, May 2004.
[20] J. Ma, S. Pulfer, S. Li, J. Chu, K. Reed, and J. M. Gallo, “Pharmacodynamic-mediated reduction of temozolomide tumor concentrations by the angiogenesis inhibitor TNP-470.,” *Cancer Res.*, vol. 61, no. 14, pp. 5491–8, Jul. 2001.
[21] J. Ma and D. J. Waxman, “Combination of antiangiogenesis with chemotherapy for more effective cancer treatment.,” *Mol. Cancer Ther.*, vol. 7, no. 12, pp. 3670–84, Dec. 2008.
[22] W. Liang, Y. Ni, and F. Chen, “Tumor resistance to vascular disrupting agents: Mechanisms, imaging, and solutions,” *Oncotarget*, vol. 7, no. 13, pp. 15444–15459, Mar. 2016.
[23] J. H. Gill, K. L. Rockley, C. De Santis, and A. K. Mohamed, “Vascular Disrupting Agents in cancer treatment: Cardiovascular toxicity and implications for co-administration with other cancer chemotherapeutics,” *Pharmacol. Ther.*, vol. 202, pp. 18–31, Oct. 2019.
[24] G. M. Tozer, C. Kanthou, and B. C. Baguley, *Disrupting tumour blood vessels*, vol. 5, no. 6. Nature Publishing Group, 2005, pp. 423–435.
[25] M. Panagi *et al.*, “TGF-β inhibition combined with cytotoxic nanomedicine normalizes triple negative breast cancer microenvironment towards anti-tumor immunity.,” *Theranostics*, vol. 10, no. 4, pp. 1910–1922, 2020.
[26] V. P. Chauhan *et al.*, “Angiotensin inhibition enhances drug delivery and potentiates chemotherapy by decompressing tumour blood vessels.,” *Nat. Commun.*, vol. 4, p. 2516, 2013.
[27] J. D. Martin *et al.*, “Dexamethasone Increases Cisplatin-Loaded Nanocarrier Delivery and Efficacy in Metastatic Breast Cancer by Normalizing the Tumor Microenvironment,” *ACS Nano*, vol. 13, no. 6, pp. 6396–6408, Jun. 2019.
[28] F. Mpekris *et al.*, “Normalizing the Microenvironment Overcomes Vessel Compression and Resistance to Nano-immunotherapy in Breast Cancer Lung Metastasis,” *Adv. Sci.*, vol. 8, no. 3, p. 2001917, Feb. 2021.
[29] L. VA, C. J, D. M, Y. JL, and J. RK, “Effect of angiotensin system inhibitors on survival in newly diagnosed glioma patients and recurrent glioblastoma patients receiving chemotherapy and/or bevacizumab,” *J. Neurooncol.*, vol. 134, no. 2, pp. 325–330, Sep. 2017.
[30] C.-Y. Lai, B. Z. Fite, and K. W. Ferrara, “Ultrasonic Enhancement of Drug Penetration in Solid Tumors,” *Front. Oncol.*, vol. 3, p. 204, Aug. 2013.
[31] V. Frenkel, “Ultrasound mediated delivery of drugs and genes to solid tumors,” *Advanced Drug Delivery Reviews*, vol. 60, no. 10. Elsevier, pp. 1193–1208, 30-Jun-2008.
[32] S. Mo, C. C. Coussios, L. Seymour, and R. Carlisle, “Ultrasound-enhanced drug delivery for cancer,” *Expert Opinion on Drug Delivery*, vol. 9, no. 12. Taylor & Francis, pp. 1525–1538, Dec-2012.
[33] S. B. Keller, D. Suo, Y.-N. Wang, H. Kenerson, R. S. Yeung, and M. A. Averkiou, “Image-Guided Treatment of Primary Liver Cancer in Mice Leads to Vascular Disruption and Increased Drug Penetration,” *Front. Pharmacol.*, vol. 11, p. 1526, Sep. 2020.
[34] B. E. Noltingk and E. A. Neppiras, “Cavitation produced by Ultrasonics,” *Proc. Phys.*

Soc. Sect. B, vol. 63, no. 9, pp. 674–685, Sep. 1950.
[35] R. Gramiak and P. M. Shah, "Echocardiography of the aortic root.," *Invest. Radiol.*, vol. 3, no. 5, pp. 356–66, 1968.
[36] S. B. Feinstein *et al.*, "Two-dimensional contrast echocardiography. I. In vitro development and quantitative analysis of echo contrast agents.," *J. Am. Coll. Cardiol.*, vol. 3, no. 1, pp. 14–20, Jan. 1984.
[37] E. Stride *et al.*, "Microbubble Agents: New Directions.," *Ultrasound Med. Biol.*, vol. 46, no. 6, pp. 1326–1343, Jun. 2020.
[38] M. A. Averkiou, M. F. Bruce, J. E. Powers, P. S. Sheeran, and P. N. Burns, *Imaging Methods for Ultrasound Contrast Agents*, vol. 46, no. 3. 2020, pp. 498–517.
[39] K. Kooiman *et al.*, "Ultrasound-Responsive Cavitation Nuclei for Therapy and Drug Delivery.," *Ultrasound Med. Biol.*, vol. 46, no. 6, pp. 1296–1325, Jun. 2020.
[40] I. De Cock *et al.*, "Ultrasound and microbubble mediated drug delivery: acoustic pressure as determinant for uptake via membrane pores or endocytosis," *J. Control. Release*, vol. 197, pp. 20–28, 2015.
[41] R. E. Vandenbroucke, I. Lentacker, J. Demeester, S. C. De Smedt, and N. N. Sanders, "Ultrasound assisted siRNA delivery using PEG-siPlex loaded microbubbles," *J. Control. Release*, vol. 126, no. 3, pp. 265–273, Mar. 2008.
[42] C.-H. Fan *et al.*, "Antiangiogenic-targeting drug-loaded microbubbles combined with focused ultrasound for glioma treatment," *Biomaterials*, vol. 34, no. 8, pp. 2142–2155, Mar. 2013.
[43] P. S. Sheeran, S. Luois, P. A. Dayton, and T. O. Matsunaga, "Formulation and Acoustic Studies of a New Phase-Shift Agent for Diagnostic and Therapeutic Ultrasound," 2011.
[44] P. S. Sheeran and P. A. Dayton, "Phase-Change Contrast Agents for Imaging and Therapy."
[45] M. G. Shapiro *et al.*, "Biogenic gas nanostructures as ultrasonic molecular reporters," 2014.
[46] R. W. Bourdeau *et al.*, "Acoustic reporter genes for noninvasive imaging of microorganisms in mammalian hosts," *Nature*, vol. 553, no. 7686, pp. 86–90, Jan. 2018.
[47] K. Ferrara, R. Pollard, and M. Borden, "Ultrasound Microbubble Contrast Agents: Fundamentals and Application to Gene and Drug Delivery," *Annu. Rev. Biomed. Eng*, vol. 9, pp. 415–47, 2007.
[48] E. Stride, "Physical principles of microbubbles for ultrasound imaging and therapy," *Cerebrovasc. Dis.*, vol. 27, no. SUPPL. 2, pp. 1–13, 2009.
[49] R. J. Eckersley, C. T. Chin, and P. N. Burns, "Optimising phase and amplitude modulation schemes for imaging microbubble contrast agents at low acoustic power.," *Ultrasound Med. Biol.*, vol. 31, no. 2, pp. 213–9, Feb. 2005.
[50] M. A. Averkiou, "Tissue harmonic imaging," in *2000 IEEE Ultrasonics Symposium. Proceedings. An International Symposium (Cat. No.00CH37121)*, vol. 2, pp. 1563–1572.
[51] C. Tremblay-Darveau *et al.*, "The Role of Microbubble Echo Phase Lag in Multipulse Contrast-Enhanced Ultrasound Imaging," *IEEE Trans. Ultrason. Ferroelectr. Freq. Control*, vol. 65, no. 8, pp. 1389–1401, Aug. 2018.
[52] S. Zhao, M. Borden, S. H. Bloch, D. Kruse, K. W. Ferrara, and P. A. Dayton, "Radiation-force assisted targeting facilitates ultrasonic molecular imaging.," *Mol. Imaging*, vol. 3, no. 3, pp. 135–48, Jul. 2004.
[53] J. Wu, J. P. Ross, and J.-F. Chiu, "Reparable sonoporation generated by microstreaming,"

J. Acoust. Soc. Am., vol. 111, no. 3, pp. 1460–1464, Mar. 2002.
[54] T. van Rooij *et al.*, "Viability of endothelial cells after ultrasound-mediated sonoporation: Influence of targeting, oscillation, and displacement of microbubbles," *J. Control. Release*, vol. 238, pp. 197–211, 2016.
[55] N. J. McDannold, N. I. Vykhodtseva, and K. Hynynen, "Microbubble contrast agent with focused ultrasound to create brain lesions at low power levels: MR imaging and histologic study in rabbits.," *Radiology*, vol. 241, no. 1, pp. 95–106, Oct. 2006.
[56] K. Hynynen, "The threshold for thermally significant cavitation in dog's thigh muscle in vivo.," *Ultrasound Med. Biol.*, vol. 17, no. 2, pp. 157–69, 1991.
[57] W.-S. Chen, A. A. Brayman, T. J. Matula, L. A. Crum, and M. W. Miller, "The pulse length-dependence of inertial cavitation dose and hemolysis," *Ultrasound Med. Biol.*, vol. 29, no. 5, pp. 739–748, May 2003.
[58] D. E. Goertz *et al.*, "Antitumor Effects of Combining Docetaxel (Taxotere) with the Antivascular Action of Ultrasound Stimulated Microbubbles," *PLoS One*, vol. 7, no. 12, p. e52307, Dec. 2012.
[59] K. J. Haworth, K. B. Bader, K. T. Rich, C. K. Holland, and T. D. Mast, "Quantitative Frequency-Domain Passive Cavitation Imaging," *IEEE Trans. Ultrason. Ferroelectr. Freq. Control*, vol. 64, no. 1, pp. 177–191, Jan. 2017.
[60] E. Lyka, C. M. Coviello, C. Paverd, M. D. Gray, and C.-C. Coussios, "Passive Acoustic Mapping using Data-Adaptive Beamforming Based on Higher-Order Statistics," *IEEE Trans. Med. Imaging*, pp. 1–1, 2018.
[61] S. B. Keller, P. S. Sheeran, and M. A. Averkiou, "Cavitation Therapy Monitoring of Commercial Microbubbles With a Clinical Scanner," *IEEE Trans. Ultrason. Ferroelectr. Freq. Control*, vol. 68, no. 4, pp. 1144–1154, Apr. 2021.
[62] T. Ilovitsh, A. Ilovitsh, J. Foiret, B. Z. Fite, and K. W. Ferrara, "Acoustical structured illumination for super-resolution ultrasound imaging," *Commun. Biol.*, vol. 1, no. 1, Dec. 2018.
[63] K. Christensen-Jeffries *et al.*, "Super-resolution Ultrasound Imaging," *Ultrasound Med. Biol.*, vol. 46, no. 4, pp. 865–891, Apr. 2020.
[64] C. Errico *et al.*, "Ultrafast ultrasound localization microscopy for deep super-resolution vascular imaging," *Nature*, vol. 527, no. 7579, pp. 499–502, Nov. 2015.
[65] J. Foiret, H. Zhang, T. Ilovitsh, L. Mahakian, S. Tam, and K. W. Ferrara, "Ultrasound localization microscopy to image and assess microvasculature in a rat kidney," *Sci. Reports 2017 71*, vol. 7, no. 1, pp. 1–12, Oct. 2017.
[66] F. Lin, S. E. Shelton, D. Espíndola, J. D. Rojas, G. Pinton, and P. A. Dayton, "3-D Ultrasound Localization Microscopy for Identifying Microvascular Morphology Features of Tumor Angiogenesis at a Resolution Beyond the Diffraction Limit of Conventional Ultrasound," *Theranostics*, vol. 7, no. 1, p. 196, 2017.
[67] S. Bao, B. D. Thrall, and D. L. Miller, "Transfection of a reporter plasmid into cultured cells by sonoporation in vitro.," *Ultrasound Med. Biol.*, vol. 23, no. 6, pp. 953–9, Jan. 1997.
[68] R. Bekeredjian, S. Chen, P. A. Grayburn, and R. V Shohet, "Augmentation of cardiac protein delivery using ultrasound targeted microbubble destruction.," *Ultrasound Med. Biol.*, vol. 31, no. 5, pp. 687–91, May 2005.
[69] R. Suzuki, Y. Oda, N. Utoguchi, and K. Maruyama, "Progress in the development of ultrasound-mediated gene delivery systems utilizing nano- and microbubbles," *J. Control.*

Release, vol. 149, no. 1, pp. 36–41, Jan. 2011.
[70] B. Helfield, X. Chen, S. C. Watkins, and F. S. Villanueva, "Biophysical insight into mechanisms of sonoporation," *Proc. Natl. Acad. Sci.*, p. 201606915, 2016.
[71] T. Takayama *et al.*, "Early hepatocellular carcinoma: pathology, imaging, and therapy.," *Ann. Surg. Oncol.*, vol. 15, no. 4, pp. 972–8, 2008.
[72] B. H. A. Lammertink, C. Bos, R. Deckers, G. Storm, C. T. W. Moonen, and J.-M. Escoffre, "Sonochemotherapy: From bench to bedside," *Front. Pharmacol.*, vol. 6, no. JUN, 2015.
[73] G. Dimcevski *et al.*, "A human clinical trial using ultrasound and microbubbles to enhance gemcitabine treatment of inoperable pancreatic cancer," *J. Control. Release*, vol. 243, pp. 172–181, Dec. 2016.
[74] E. K. Rofstad, K. Galappathi, and B. S. Mathiesen, "Tumor interstitial fluid pressure-a link between tumor hypoxia, microvascular density, and lymph node metastasis.," *Neoplasia*, vol. 16, no. 7, pp. 586–94, Jul. 2014.
[75] K. D. Watson *et al.*, "Ultrasound increases nanoparticle delivery by reducing intratumoral pressure and increasing transport in epithelial and epithelial-mesenchymal transition tumors.," *Cancer Res.*, vol. 72, no. 6, pp. 1485–93, Mar. 2012.
[76] A. Mohammadabadi *et al.*, "Pulsed focused ultrasound lowers interstitial fluid pressure and increases nanoparticle delivery and penetration in head and neck squamous cell carcinoma xenograft tumors," *Phys. Med. Biol.*, vol. 65, no. 12, p. 125017, Jun. 2020.
[77] M. Bazan-Peregrino, C. D. Arvanitis, B. Rifai, L. W. Seymour, and C.-C. Coussios, "Ultrasound-induced cavitation enhances the delivery and therapeutic efficacy of an oncolytic virus in an in vitro model," *J. Control. Release*, vol. 157, pp. 235–242, 2012.
[78] N. Xiao, J. Liu, L. Liao, J. Sun, W. Jin, and X. Shu, "Ultrasound Combined With Microbubbles Increase the Delivery of Doxorubicin by Reducing the Interstitial Fluid Pressure," *Ultrasound Q.*, vol. 35, no. 2, pp. 103–109, Jun. 2019.
[79] Q. Zhang *et al.*, "Effect of ultrasound combined with microbubble therapy on interstitial fluid pressure and VX2 tumor structure in rabbit," *Front. Pharmacol.*, vol. 10, no. JUN, 2019.
[80] S. Umemura, K. Kawabata, and K. Sasaki, "In vivo acceleration of ultrasonic tissue heating by microbubble agent," *IEEE Trans. Ultrason. Ferroelectr. Freq. Control*, vol. 52, no. 10, pp. 1690–1698, Oct. 2005.
[81] R. G. Holt and R. A. Roy, "Measurements of bubble-enhanced heating from focused, mhz-frequency ultrasound in a tissue-mimicking material," *Ultrasound Med. Biol.*, vol. 27, no. 10, pp. 1399–1412, Oct. 2001.
[82] A. Clark, S. Bonilla, D. Suo, Y. Shapira, and M. Averkiou, "Microbubble-Enhanced Heating: Exploring the Effect of Microbubble Concentration and Pressure Amplitude on High-Intensity Focused Ultrasound Treatments," *Ultrasound Med. Biol.*, May 2021.
[83] S. Keller, M. Bruce, and M. A. Averkiou, "Ultrasound Imaging of Microbubble Activity during Sonoporation Pulse Sequences," *Ultrasound Med. Biol.*, vol. 45, no. 3, pp. 833–845, Jan. 2019.
[84] R. Staruch, R. Chopra, and K. Hynynen, "Localised drug release using MRI-controlled focused ultrasound hyperthermia," *Int. J. Hyperth.*, vol. 27, no. 2, pp. 156–171, Mar. 2011.
[85] H. Grüll and S. Langereis, "Hyperthermia-triggered drug delivery from temperature-sensitive liposomes using MRI-guided high intensity focused ultrasound," *J. Control.*

Release, vol. 161, no. 2, pp. 317–327, Jul. 2012.
[86] J. Escoffre *et al.*, "Doxorubicin liposome-loaded microbubbles for contrast imaging and ultrasound-triggered drug delivery," *IEEE Trans. Ultrason. Ferroelectr. Freq. Control*, vol. 60, no. 1, Jan. 2013.
[87] C. Mannaris, E. Efthymiou, M.-E. Meyre, and M. A. Averkiou, "In vitro localized release of thermosensitive liposomes with ultrasound-induced hyperthermia.," *Ultrasound Med. Biol.*, vol. 39, no. 11, pp. 2011–20, Nov. 2013.
[88] K. Kaczmarek, T. Hornowski, M. Kubovčíková, M. Timko, M. Koralewski, and A. Józefczak, "Heating Induced by Therapeutic Ultrasound in the Presence of Magnetic Nanoparticles," *ACS Appl. Mater. Interfaces*, vol. 10, no. 14, pp. 11554–11564, Apr. 2018.
[89] Y.-J. Ho, T.-C. Wang, C.-H. Fan, and C.-K. Yeh, "Spatially Uniform Tumor Treatment and Drug Penetration by Regulating Ultrasound with Microbubbles," *ACS Appl. Mater. Interfaces*, vol. 10, no. 21, p. acsami.8b05508, May 2018.
[90] X. Hu *et al.*, "Insonation of targeted microbubbles produces regions of reduced blood flow within tumor vasculature.," *Invest. Radiol.*, vol. 47, no. 7, pp. 398–405, Jul. 2012.
[91] J. Wang *et al.*, "Selective depletion of tumor neovasculature by microbubble destruction with appropriate ultrasound pressure," *Int. J. Cancer*, vol. 137, no. 10, pp. 2478–2491, Nov. 2015.
[92] M. Bruce *et al.*, "High-Frequency Nonlinear Doppler Contrast-Enhanced Ultrasound Imaging of Blood Flow," *IEEE Trans. Ultrason. Ferroelectr. Freq. Control*, vol. 67, no. 9, pp. 1776–1784, Sep. 2020.

Chapter 2. CAVITATION THERAPY MONITORING OF COMMERCIAL MICROBUBBLES WITH A CLINICAL SCANNER[1]

Abstract

The ability to monitor cavitation activity during ultrasound and microbubble-mediated procedures is of high clinical value. However, there has been little reported literature comparing the cavitation characteristics of different clinical microbubbles, nor have current clinical scanners been used to perform passive cavitation detection in real time. The goal of this work was to investigate and characterize standard microbubble formulations (Optison, SonoVue, Sonazoid, and a custom microbubble made with similar components as Definity) with a custom passive cavitation detector (2 confocal single element focused transducers) and with a Philips EPIQ scanner with a C5-1 curvilinear probe passively listening. We evaluated three different methods for investigating cavitation thresholds, two from previously reported work and one developed in the present work. For all three techniques, it was observed that the inertial cavitation thresholds were between 0.1 – 0.3 MPa for all agents when detected with both systems. Notably, we found that most microbubble formulations in bulk solution behaved generally similarly, with some differences. We show that these characteristics and thresholds are maintained when using a diagnostic ultrasound system for detecting cavitation activity. We believe that a systematic evaluation of the frequency response of the cavitation activity of different microbubbles in order to inform real-time therapy monitoring using a clinical ultrasound device could make an immediate clinical impact.

2.1 INTRODUCTION

Ultrasound-mediated drug uptake enhancement using microbubbles is a promising technique that can lead to enhanced local therapeutic effect or macromolecule transport. The biological mechanism is often thought to be a result of cavitation events at the site of interest [1], [2]. Depending on the desired therapeutic outcome, different types of cavitation, stable or inertial, may be preferred [3]. Whether a microbubble is oscillating stably or inertially may be determined by

[1] *Reprinted with permission from Keller, SB, et al. "Cavitaiton therapy monitoring of commercial microbubbles with a clinical scanner." IEEE Trans. Ultrason. Freq. Control.,* ***68****, 1144-1154 (2021). Copyright 2021 IEEE*

examining the frequency spectrum of scattered sound, where stable cavitation is defined by the presence of sub- and ultraharmonics [4] and inertial cavitation is defined by the onset of broadband noise [5]. Both stable [6] and inertial cavitation [7] have been shown to have therapeutic efficacy, including in the clinic [8]; however, inertial cavitation is sometimes avoided due to the likelihood of adverse bioeffects, e.g. when opening the blood brain barrier [9]–[11].

In order for microbubble-mediated ultrasound therapies to be clinically relevant, it is important to differentiate cavitation activity generated by various clinically approved contrast agents such as Optison, Definity, SonoVue, and Sonazoid. While cavitation detection and classification have been performed previously on certain individual contrast agents, there are very few studies that have compared the frequency responses of multiple commercial contrast agents in a standardized and reproducible manner. Indeed, Hyvelin et al. reported that this lack of output may be "the result of a favorable competitive environment" in a study that compared just the echogenicity of the contrast agents, and not their scattered frequency response [12]. Tremblay-Darveau et al. compared Definity, Sonazoid, and Optison for their response to nonlinear pulsing schemes, which is not necessarily applicable to ultrasound therapy [13] and did not identify inertial cavitation thresholds. Therefore, despite the fact that these microbubbles have been extensively used, a standardized comparison of the cavitation characteristics of commercial microbubbles in bulk solutions has not been sufficiently reported.

The studies that have shown comparison of microbubbles during ultrasound therapy generally only compare the "inertial cavitation dose" (ICD) [5], [14], [15]. To calculate ICD, each microbubble scatter over the duration of the treatment period (multiple firings) is filtered at either a sub/ultraharmonic (for stable cavitation) or a broadband frequency band (for inertial cavitation). The root mean square (RMS) of each filtered signal is calculated and plotted as a function of time over the sonication duration. ICD is the integral of the filtered RMS versus time curve. While useful at determining whether a total treatment regimen induces inertial cavitation, as a method of threshold detection, ICD is biased by pulsing parameters including pulse repetition period and total length of insonation, which may vary widely based on therapeutic procedures. We hypothesize that evaluating microbubble echoes on a per-scatter basis is more useful for real-time monitoring. One goal of the present work was to compare various methods of evaluating individual

microbubble echoes for determining inertial cavitation thresholds, both methods that have been previously reported [16], [17] and a novel cavitation analysis method developed here.

Further, for cavitation therapy monitoring to be informative, it relies on appropriate detection and subsequent delineation of inertial cavitation. Currently, most passive cavitation detection schemes are done with custom setups and single element transducers [7], [18], [19], which do not have the ability to spatially localize the source of cavitation events and tend to require complex hardware and challenging alignment schemes, or with research scanners with GPUs and/or specialized ultrasound scanners [20], [21] that are not necessarily ready for immediate patient use. In the clinic, generally the only informative option for therapeutic monitoring has been loss of echogenicity of contrast agents, which is not necessarily related to the onset of inertial cavitation [17]. Those that have used diagnostic ultrasound systems typically employ offline processing to show cavitation behavior in specialized applications which may not be translatable to broader microbubble-mediated therapies [22], [23]. Furthermore, the differences in cavitation behavior of different microbubbles have generally not been considered when performing cavitation detection using arrays. More importantly, a validation that microbubble frequency response can be appropriately recapitulated when transitioning from using single-element transducers to imaging arrays for the detection of inertial cavitation has not been reported.

The overall goal of this work was to investigate and characterize standard microbubble formulations (Optison, SonoVue, Sonazoid, and a custom "Definity-like" agent) and use this knowledge to perform real-time cavitation monitoring using a Philips EPIQ with a C5-1 curvilinear probe. We chose to focus on pulsing parameters that are relevant to microbubble-mediated drug delivery; 1 MHz transmit frequency, moderate 40 cycle pulse length, and pressures ranging from 0.1 – 1 MPa [15], [19], [24]. We perform three inertial cavitation detection schemes: two reported previously [16], [17] and the third proposed here. We further show that the same characteristics and thresholds may also be detected when using a clinical ultrasound scanner for passively detecting cavitation data. While still lacking precise spatial localization as developed in other novel beamforming-related work (including Capon and Robust Capon Beamforming algorithms described elsewhere [20], [25]), our technique allows for immediate observation of cavitation presence based on accurately defined thresholds on commercially available machines. We believe

that a systematic evaluation of the frequency response of the cavitation activity of different microbubbles in order to inform real-time therapy monitoring using a clinical ultrasound scanner could make an immediate clinical impact.

2.2 MATERIALS AND METHODS

2.2.1 *Experimental Setup*

SonoVue (Bracco Suisse SA, Geneva, Switzerland), Sonazoid (GE Healthcare, Chicago, IL, USA), and Optison (GE Healthcare, Chicago, IL, USA) were resuspended according to the manufacturer's instructions. Another contrast agent considered was custom microbubbles composed of DPPC (1,2-dipalmitoyl-sn-glycero-3-phosphocholine) and DSPE-PEG (1,2-distearoyl-sn-glycero-3-phosphoethanolamine-N-[methoxy(polyethylene glycol)-2000]) (Avanti Polar Lipids Inc, Alabaster, AL) in a 95:5 molar ratio that were prepared as described previously [26] as a model for a "Definity-like" microbubble due to similarities in material composition. Microbubble concentration and size by number and by volume were measured using a Multisizer 3 (Beckman Coulter, Brea, CA, USA) using a 30 μm aperture tube that had lower and higher thresholds of 0.735 μm and 20 μm, respectively. Microbubbles were diluted in a 1:2000 ratio in Isoton II. Three measurements were taken for each formulation, and the averages and standard deviations are reported in **Table 2.1**.

Table 2.1: Physical characteristics of various microbubble formulations

	Concentration (MB/mL)	Mean Diameter (by number) (μm) ± S.D.	Mean Diameter (by volume) (μm) ± S.D.
Definity-like	1.19E9	1.59 ± 0.76	2.95 ± 1.24
Optison	4.33E8	1.24 ± 0.55	4.99 ± 4.64
SonoVue	2.86E8	1.82 ± 1.27	5.89 ± 3.07
Sonazoid	1.79E8	1.96 ± 0.70	3.67 ± 3.63

We recorded cavitation activity of the different microbubbles with two different passive cavitation detection setups: (a) with a single element focused transducer and (b) with a clinical curvilinear array of a diagnostic scanner operating in a passive listening mode. A 1 MHz focused transducer (V392, diameter = 3.81 cm, focal distance = 7.6 cm, Olympus NDT, Waltham, MA, USA) was

used as the source of cavitation excitation. A 5 MHz focused transducer (C308, diameter = 1.91 cm, focal distance = 5.1 cm, Olympus NDT, Waltham, MA, USA) or a C5-1 curvilinear probe (total array width = 4.96 cm, elevational focus = 6 cm, number of elements = 160) on a Philips EPIQ (Philips Healthcare, Bothell, WA, USA) was confocally aligned with the 1 MHz transducer at a 90-degree angle and used to passively acquire scattered signals (**Fig. 2.1**). The confocal zone of the single element PCD setup is approximated to be a spheroid with dimensions 4 mm x 1 mm (dimensions indicate 6 dB down transverse beam widths at their center frequency), depicted by the dashed line of **Fig. 2.1b**. The imaging probe was placed 6 cm with its axis perpendicular to that of the V392, such that the focal region of the V392 was about at the middle of the imaging depth of 12 cm. The azimuthal plane of the C5-1 was parallel to the propagation axis of the V392 and therefore the confocal area is assumed to be a spheroid merely with the 6 dB down dimensions of the V392 (4 mm x 2 mm). For the clinical scanner, we turned off the transmitted voltage and allowed only the receive process, described more in depth in Section II-C. Microbubbles were introduced as a bolus injection and were diluted in the water tank at a concentration of 10^4 microbubbles/mL, similar to the setup used by King et al. [27]. This concentration was determined by evaluating scattered RMS signal amplitude versus microbubble concentration with the C308 in setup (a) described above, using a 200 kPa transmit voltage in order to have sufficient signal to noise, but to limit pressure-dependent attenuation [28]. Microbubbles were drawn from the bottom of the vial, after they had settled for 60 s in order to limit inclusion of large bubbles. It was observed that signal amplitude increased up to 10^4 microbubbles/mL, at which point the signal amplitude started to decrease, indicating that significant acoustic attenuation occurred (**Fig. 2.2**). This agrees with prior observations that concentrations beyond 10^4 microbubbles/mL induce attenuation at 1 MHz [28], and therefore this concentration was used for each experiment, and confirmed each time with Coulter counter measurements. After introduction of microbubbles into the water tank, the fluid was continuously stirred (at low revolutions per minute) to ensure the presence of microbubbles throughout the duration of the experiment. A single vial was used per each individual microbubble experiment, which lasted approximately 1 hour, within an adequate time range to limit microbubble degradation. Although tubing [22] or phantoms [9], [29] have been used in prior experiments, we chose to evaluate microbubbles in the free field in order to minimize acoustic scattering from the tubing and reverberations. We carefully maintained the microbubble concentration by both stirring between trials and replenishing the microbubble supply between

pressure settings. We also validated microbubble presence by observing the oscilloscope and/or imaging system throughout the duration of the experiment and repeated sonications to confirm that scattered signal was being received with every pulse.

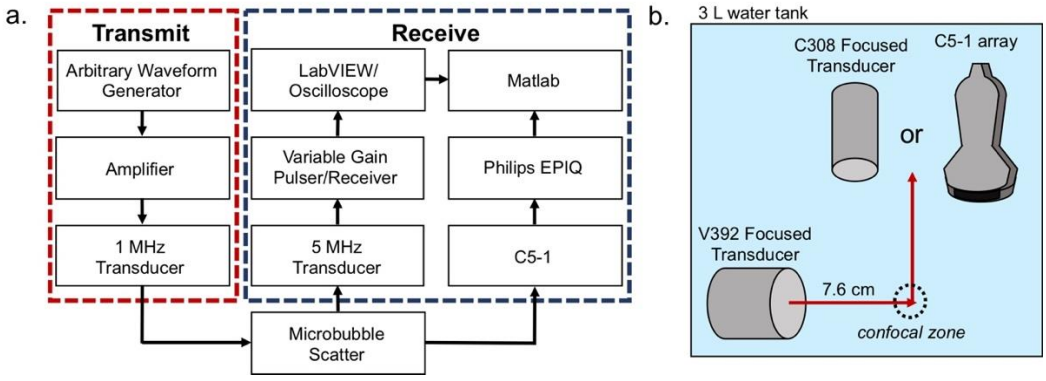

Fig. 2.1: Flowchart depicting the signal pathway for cavitation detection

A 1 MHz single element transducer transmits ultrasound pulses, and the scattered ultrasound echoes are received with either a 5 MHz single element focused transducer or C5-1 curvilinear array. (b) Pictorial depiction of experimental setup.

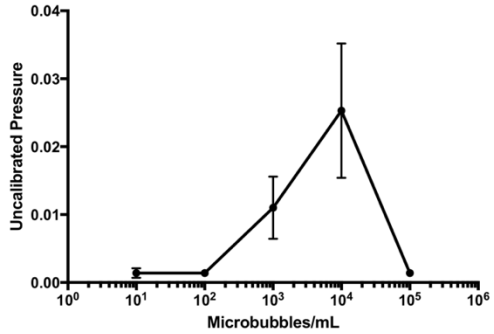

Fig. 2.2: Scattered ultrasound pressure versus microbubble concentration.

Received RMS pressure of microbubble echoes at increasing concentration from 50 waveforms using the single element transducer. Signal amplitude increases until the microbubble concentration reaches 1E4 microbubbles/mL, after which acoustic shadowing occurs. The error bars represent standard deviation of the 50 trials.

2.2.2 *Cavitation Signal Acquisition*

Tone bursts of 40 cycles reaching focal peak negative pressures of 0.1 to 1 MPa as calibrated using a 0.4 mm membrane hydrophone (Precision Acoustics Ltd., Dorchester, UK) were transmitted by the V392. We used a Tektronix AFG 3102 Arbitrary Waveform Generator (Tektronix, Inc., Beaverton, OR) to generate the tone bursts, and an ENI 2200L RF Amplifier (ENI, Rochester, NY)

to amplify the signal. For experiments with the C308 as a passive receiver, the received signals were amplified by 20 dB using a variable gain preamplifier (Panametrics, Waltham, MA, USA) and were digitized using a DPO7054C Oscilloscope (Tektronix, Inc., Beaverton, OR) with a sampling frequency of 200 MHz. A custom LabVIEW program (National Instruments, Austin, TX, USA) was used to acquire microbubble echoes, and waveforms were then analyzed in MATLAB (The MathWorks, Inc., Natick, MA, USA) as shown in **Fig. 2.1**. 50 scattered echoes were collected per pressure setting.

2.2.3 *Changes Made to the EPIQ for Offline Cavitation Detection*

When using the EPIQ scanner for offline waveform analysis, the C5-1 array replaced the single element C308 as the passive receiver (**Fig. 2.1b**) and just SonoVue and the "Definity-like" bubbles were compared for simplicity. In order to replicate true passive cavitation detection on the EPIQ, modifications were made to both the transmit and receive processes. Although modifications were made through engineering access in a custom software build, all were simple changes to pre-existing imaging schemes and post-processing algorithms within the EPIQ scanner software release 6.0, in B-mode and non-spatial compounding settings. On the transmit side, the output voltage was set to the lowest output available on the system (effectively 0 V). A specific port on the EPIQ that corresponded to a frame trigger was connected to the function generator, such that a trigger to the cavitation source was sent once per frame (therefore only one pulse was received per frame). The central line was chosen as the trigger signal so that the pulse was sent when the central line was received, and therefore received on that same line in the center of the frame. The position of the echo was based on the time-of-flight of sound from the V392 to the microbubbles and then the microbubbles to the C5-1. The duration of the transmit pulse (and therefore the received echo) was sufficiently short enough that it appeared only on one line; however, should we have used a pulse duration longer than the imaging pulse repetition interval, it is possible the echo would have also appeared on the subsequent line. The imaging frame rate was reduced to 2 Hz, by employing 500 ms delays between frames in order to ensure that any multipath reverberations had been eliminated. On the receive side, we modified a pre-existing abdominal imaging setting that avoided multiline, meaning that one receive line was formed for every transmit event. This imaging setting otherwise performed standard delay-and-sum beamforming. We additionally removed all digital and analog gains (including time-gain compensation) due to the

larger signals received with inertial cavitation (compared to typical tissue echoes). For offline processing, RF data were acquired using a research interface and analyzed in MATLAB for cavitation characteristics. RF data were post-beamformed, meaning that beamforming had already been applied on the acquired microbubble echoes. Therefore, each waveform that was received and subsequently analyzed was the raw data of a specific imaging line prior to envelope detection and log-compression. For real-time cavitation detection, display settings are described more in depth in **Section 2.2.5**.

2.2.4 *Process for Determining Cavitation Thresholds*

All waveforms from both the C308 and C5-1 were analyzed as shown in **Fig. 2.3**. Briefly, the waveforms were cropped (b) and windowed (c) with a Hamming window. A Fast Fourier Transform (FFT) was taken of each windowed waveform (d). FFTs from the 50 echoes were averaged, resulting in an average spectrum for each transmit pressure setting. Then, three separate methods of evaluating inertial cavitation thresholds were implemented, discussed below. All methods evaluated the appearance of broadband noise, or noise that is distributed over all frequencies, and is a result of inertial cavitation [30].

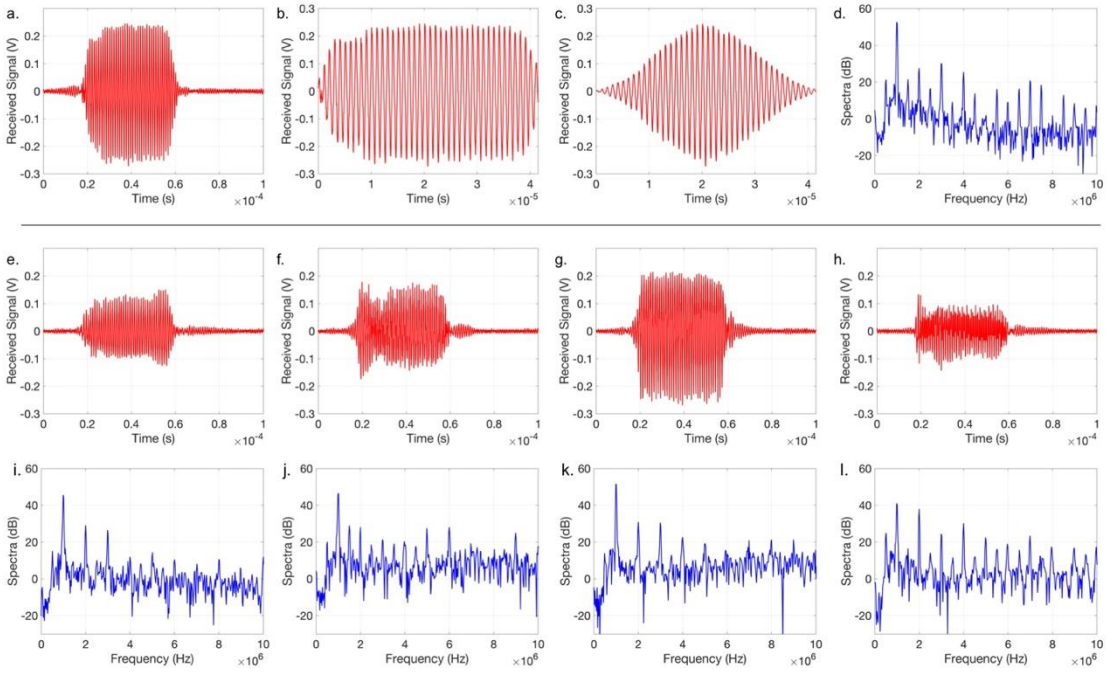

Fig. 2.3: Data analysis procedure for analyzing scattered microbubble emissions.

(a) raw signal acquisition from a single echo, (b) cropping to remove the tails, (c) windowing, and (d) FFT. (e) – (f) show examples of variability between trials for the same parameters, including

the untruncated time domain signal and frequency domain spectra after truncation/windowing. All pulses are scattered echoes from SonoVue excited at 300 kPa to allow for comparison.

2.2.4.1 Probability Method

The 'probability method' was performed based on the publication by Fabiilli, et al. [16]. Briefly, a narrow frequency band representing inertial cavitation was chosen. For our data, we chose to evaluate the frequency band between 3.1 to 3.4 MHz, to avoid harmonics and ultraharmonics. The 'integrated Fourier transform' (IFT) was calculated for each echo per pressure, which was simply the area under the curve of the Fourier transform between the narrow frequency range. To establish a baseline value, this was also performed per each pressure in degassed water. An echo was considered inertial cavitation if it satisfied the following equation:

$$IFT_{cav,\,P} \geq IFT_{w,\,P} + 9 \cdot \sigma_{w,\,P} \quad (2.1)$$

where $IFT_{cav,P}$ is the IFT of an individual trial, $IFT_{w,P}$ is the average degassed water IFT at a particular pressure, and $\sigma_{w,P}$ is the standard deviation of the degassed water IFT at that same pressure. Cavitation probability was calculated as the ratio of echoes per pressure that met the IC criteria over the total number of echoes, 50 in our case. A sigmoid curve was fit to the pressure versus probability data to determine the 50% crossing point, which signified the cavitation threshold. It should be noted that variations on this method have also been applied elsewhere [31].

2.2.4.2 Piecewise Method

The second method, which we called the 'piecewise method', is based on a publication by Radhakrishnan et al. [17]. The piecewise method involves filtering each cavitation scattered signal to isolate solely broadband noise, calculating the root mean square (RMS) of the filtered signal, and determining where the filtered RMS signal begins to increase linearly with increasing pressure. To accomplish this, we created a notch filter to remove all harmonics, subharmonics, and ultraharmonics, leaving only broadband noise. Then, we took the RMS of the filtered signal in time domain. We then subtracted the filtered RMS value of a baseline (degassed water) signal. We plotted the resultant RMS signal against transmit pressure and used the MATLAB toolbox 'slmengine' to fit a two-segment piecewise linear fit curve to the data. We forced the first segment to have a slope of 0. The inflection point of the piecewise function became the inertial cavitation threshold.

2.2.4.3 Ratio Method

As another method of characterizing cavitation thresholds, we define a new parameter, PV_{ratio}, to describe the point at which the rate of increase of broadband noise is faster than that of the harmonics and ultraharmonics. This method was chosen in order to be baseline independent. Shown in **Fig. 2.4**, broadband noise is the signal in the spectrum present at frequencies other than the harmonics (and subharmonics). We refer to the signal around the harmonics as the "peaks" and the broadband noise as the "valleys" and we define PV_{ratio} by the following equation,

$$PV_{ratio} = \frac{1}{N}\sum_{i=n}^{n+N-1} p_i - v_i \qquad (2.2)$$

where N is the total number of harmonics analyzed, n is the first harmonic to be analyzed, p_i is the n^{th} harmonic in decibels, and v_i is the minimum value of the broadband noise subsequent to the n^{th} harmonic but before the $(n+1)^{th}$ harmonic, also in decibels (**Fig. 2.4b**). For both the C308 transducer and C5-1 array, the analyses started at $n=3$, to avoid including the first and second harmonics that are present in nonlinear microbubble oscillations as well as tissue harmonic imaging. Three harmonics were analyzed $(N=3)$, which meant that the bandwidth considered was 3-6 MHz. This was primarily for comparison between the two receivers, as the C5-1 had a lower center frequency and bandwidth, 1.5 – 6 MHz. The cavitation threshold is the inflection point of the PV_{ratio}, ie, the pressure at which the ratio went from increasing (implying that the harmonics were increasing more quickly relative to broadband noise) to decreasing (where the broadband noise was increasing more quickly relative to the harmonics).

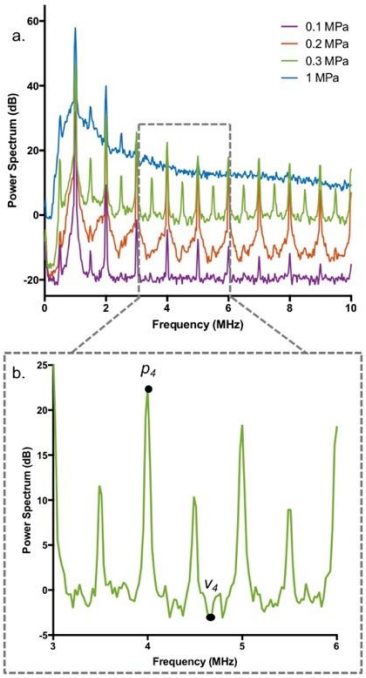

Fig. 2.4: Analysis procedure for determining PV_{ratio}.

(a) The average spectrum of SonoVue echoes at 4 different transmit pressures. (b) An example of calculating PV_{ratio} at index 4, where p_4 is the fourth harmonic, and v_4 is the minimum value between the fourth and fifth harmonics. PV_{ratio} is defined as the average difference between harmonic peaks and broadband noise valleys in decibels.

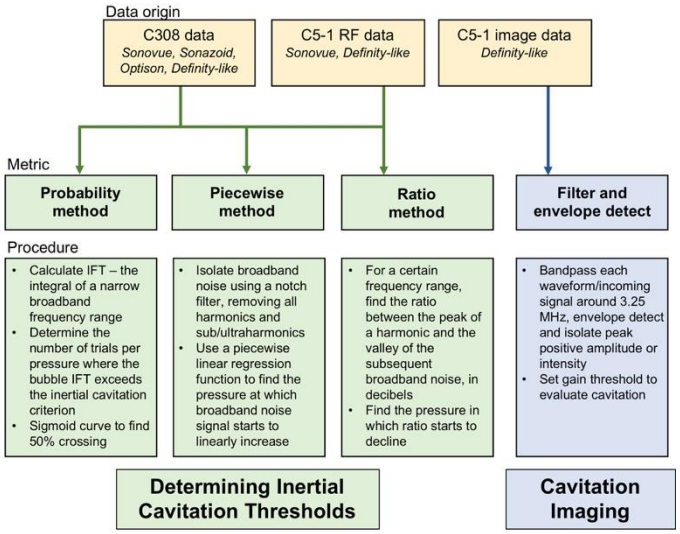

Fig. 2.5: Workflow of data analysis

Waveforms from the C308 single element transducer and C5-1 imaging array were used to determine inertial cavitation thresholds through three methods: the probability method (based on [16]), the piecewise method (based on [17]) and the proposed ratio method. Cavitation images

were formed based on a evaluating the increase in broadband noise at a particular bandwidth. The analyzed signal is therefore comparable to the methods explored.

2.2.5 *Real-time Cavitation Monitoring with Philips EPIQ*

While using the same transmit/receive sequences and triggering as in the offline processing, we chose to evaluate a variation on the above methods for real-time cavitation monitoring. A bandpass receive filter with center frequency of 3.25 MHz and 0.3 MHz bandwidth was created on the EPIQ for observing inertial cavitation. The receive filter characteristics were confirmed by directly transmitting pulses with the V392 while varying the frequency with the function generator and receiving with the C5-1 array. This frequency band was chosen because 3.25 MHz is near the center of the C5-1's bandwidth and it avoids both harmonics and ultraharmonics. The 2D gain was empirically set to 71% in order to visualize the echoes. Passive cavitation images were then formed from the "Definity-like" agent. For the same transmit pressures, 30 frames were recorded on the EPIQ using the same triggering protocol described in **Section 2.2.3** to minimize reverberations. Cavitation detection of the log-compressed scatters was observed in real-time.

2.3 RESULTS

2.3.1 *Frequency Response of Microbubbles*

Averaged FFTs of echoes from all microbubbles at increasing excitation pressures can be seen in **Fig. 2.6** and **Fig. 2.7**. In **Fig. 2.6** we show data acquired using the C308 single element receiver, while in **Fig. 2.7** we show data acquired using the C5-1 imaging array. It can be seen that with an increase in pressure, the frequency spectra also increase in magnitude, due to an increase in both harmonic power and broadband noise. Ultraharmonics also appear prominently in several midrange pressures (0.2 – 0.5 MPa) but are less obvious at the highest pressure (1 MPa), likely due to the increase in amplitude of the in-between frequencies (broadband noise) as a result of inertial cavitation. Similarly, the prominence of the harmonic peaks decreases with increasing pressure due to the same reason. While all bubbles follow similar trends, there are some notable differences; the broadband noise from SonoVue and Optison appears to elevate quickest, while the signal from Sonazoid and the "Definity-like" bubbles appear to elevate slower. Sonazoid maintains strong harmonic signal despite increases in broadband noise at high excitation pressures, whereas

the other formulations seem more susceptible broadband noise overpowering harmonics. Furthermore, despite the obvious differences in bandwidth between the C308 and the C5-1, the trends of the received spectra using the C5-1 array as the receive transducer agree with those of the C308 for both microbubble formulations ("Definity-like" and SonoVue) (**Fig. 2.6a** vs. **Fig. 2.7a** and **Fig. 2.6d** vs. **Fig. 2.7b**).

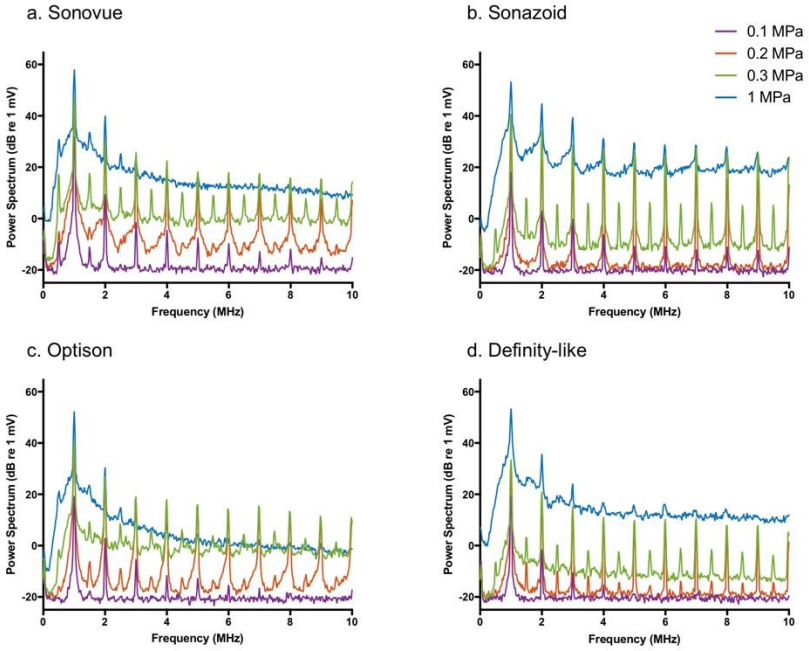

Fig. 2.6: Frequency spectra of various microbubble formulations from the C308.

Average frequency spectra of microbubble echoes at different excitation pressures received using the C308 single element transducer from the four agents used: (a) SonoVue, (b) Sonazoid, (c) Optison, and (d) "Definity-like".

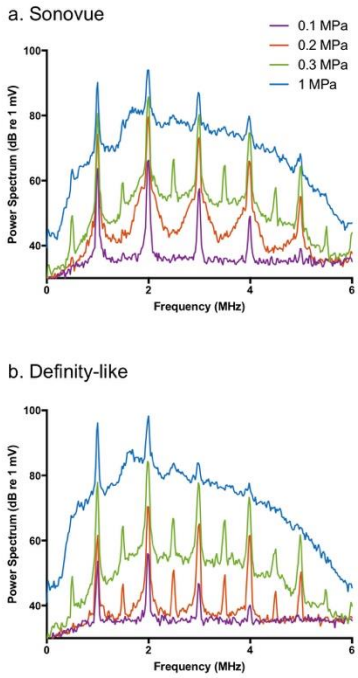

Fig. 2.7: Frequency spectra of various microbubble formulations from the C5-1.

Average frequency spectra of microbubble echoes at different excitation pressures received using the C5-1 array from two agents: (a) SonoVue and (b) "Definity-like".

2.3.2 *Cavitation Thresholds*

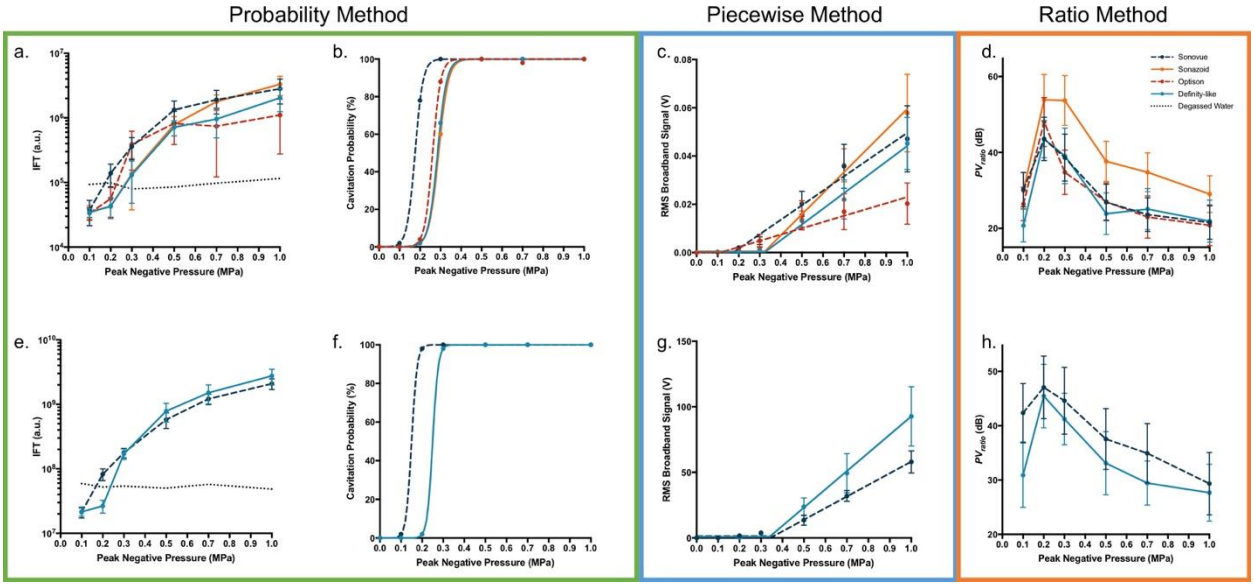

Fig. 2.8: PV_{ratio} and filtered signal from various microbubble formulations from the C308.

(a) and (c) show PV_{ratio} from the C308 and C5-1, respectively. PV_{ratio} is the average difference between the harmonic peaks and broadband noise values calculated in the 3-6 MHz range. The inflection point defines the inertial cavitation threshold, lowest for Optison and highest for Sonazoid. (b) and (d) show the amplitude of the filtered scattered pulses at 3.25 MHz from the C308 and C5-1, respectively. Echoes from all contrast agents increase with increasing pressure; however, echoes from Sonazoid have the highest amplitude in this frequency range at high pressures.

Fig. 2.8 (**a,b**), (**c**), and (**d**) show cavitation threshold analysis using the probability method, piecewise method, and ratio method, respectively, using data from the C308 single element transducer. **Fig. 2.8** (**e,f**), (**g**), and (**h**) show the same analyses performed on RF data from the C5-1 imaging array. Summarized thresholds can be seen in **Table 2.2**.

The 50% crossing point of the sigmoid curves used in the probability method shown in **Fig. 2.8** (**b**) and (**f**) are used to evaluate the inertial cavitation threshold. It can be seen that the cavitation thresholds using this method are between 0.15 and 0.3 for all microbubbles, higher for Sonazoid and Definity-like, and a little lower for Optison and SonoVue. These trends are also observed when using the piecewise method; however, Optison was shown to have a cavitation threshold quite a bit lower than what was calculated using the probability method. When using the C5-1 imaging array, the thresholds were within the same approximate range.

To evaluate PV_{ratio} **Fig. 2.8(d**) and (**h**)), the inflection point indicates the excitation pressure at which broadband noise begins to become the dominant signal component and is used here as a metric of inertial cavitation threshold. Optison reaches this point earliest, at 0.2 MPa. The inflection point of SonoVue and the Definity-like bubble occurs in between 0.2 and 0.3 MPa, which we approximate to be 0.25 MPa from linear interpolation. Sonazoid is the latest, at 0.3 MPa. The inflection points in the C5-1 PV_{ratio} data in (**h**) agree with those shown for Definity-like and SonoVue in (**d**). It is worth noting that all methods show the same relative differences between formulations.

Table 2.2: Cavitation thresholds calculated based on PV_{ratio}

	Probability Method (MPa)	**Piecewise Method (MPa)**	**Ratio Method (MPa)**
C308			
SonoVue	0.17	0.18	0.25
Sonazoid	0.29	0.32	0.30
Optison	0.26	0.11	0.20
Definity-like	0.29	0.33	0.25
C5-1			
SonoVue	0.15	0.26	0.25
Definity-like	0.25	0.27	0.2

2.3.3 *Cavitation Monitoring with Philips EPIQ*

We implemented a variation of the probability method on the EPIQ scanner with the C5-1 imaging array to evaluate cavitation activity in real time. Microbubble echoes were detected within a narrow frequency band (3.1 to 3.4 MHz), consistent with the probability method. This band was chosen in order to isolate solely inertial signal, without either harmonics or ultraharmonics. In **Fig. 2.9** (**a-b**) we show conventional ultrasound images (not to be confused with inertial cavitation images shown in (**c-d**)) of the microbubble solution in contrast mode (AM). A black image in **Fig. 2.9a** is seen before the microbubbles are injected. The image in **Fig. 2.9b** shows uniformly distributed microbubbles in the water tank. In (**c**) – (**e**) we show images formed using the probability method for passive cavitation detection. The images in **Fig. 2.9**(**c-e**) cover the area indicated with a white rectangle in **Fig. 2.9b**. The scattered pulses from 0.2, 0.3, and 1.0 MPa that have been filtered with the 3.25 MHz filters form the images seen in **Fig. 2.9** (**c**), (**d**), and (**e**), respectively. These images are formed with the filtered and envelop-detected signals and indicate the presence of broadband noise in the echoes, and therefore inertial cavitation. These inertial cavitation echoes are detected on one receive line, due to the triggering scheme described previously. The position of the received scatters is not the actual position of inertial cavitation; as the scanner places it according to its received time divided by two (relative to the trigger time), as opposed to the time-of-flight of sound transmission from the single element transducer to the C5-1. The image brightness in **Fig. 2.9** (**c**), (**d**), and (**e**) corresponds to the amplitude of the inertial cavitation echoes and the spatial length of the signal corresponds to the actual duration of the time

domain signal that exceeds the set threshold of inertial cavitation, exemplified by the time scale in (**c**). Although not a "true" position, it confirms that there are microbubbles in the imaging plane (of the true position shown in (**b**)) that are scattering broadband noise frequencies. The appearance of inertial cavitation is shown to begin between 0.2 (**c**) and 0.3 (**d**) MPa and becomes brighter with increasing excitation pressure, which agrees with the cavitation threshold calculated for the Definity-like bubble being approximately 0.25-0.3 MPa from the inertial cavitation analyses. These images also demonstrate that a clinical scanner can give a qualitative indication of inertial cavitation activity by passively listening for bubble activity in the imaging plane. In order to passively listen for inertial cavitation with a clinical scanner, one would only need to synchronize the triggering of the cavitation source with the scanner and implement the changes described in **Section 2.2.5**.

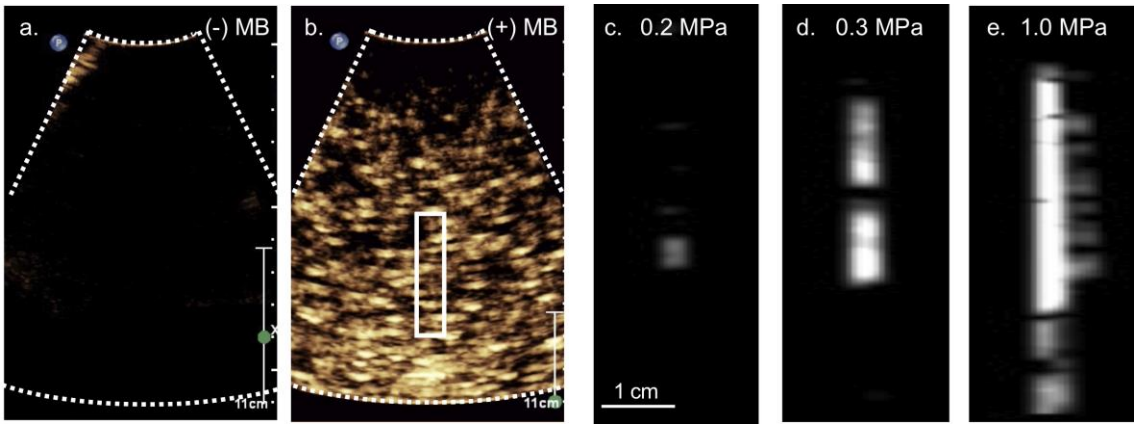

Fig. 2.9: Inertial cavitation images of the Definity-like agent with the C5-1.

(a)-(b) show the standard contrast image before the cavitation ultrasound source is turned on confirming bubble presence. The images created of inertial cavitation are shown in (c) for 0.2 MPa, (d) for 0.3 MPa and (e) for 1.0 MPa. The spatial length of the signals in (c)-(e) corresponds to the actual duration of the time domain signal that exceeds the set threshold of inertial cavitation, indicated by time in the scale bar. The spatial position of the echo occurred in the white box in (b).

2.4 DISCUSSION

Cavitation characteristics of clinically approved microbubble contrast agents were investigated with 2 passive cavitation detection setups: (a) a single element focused transducer in a classic PCD configuration, and (b) a curvilinear array on a clinical scanner operating in passive listening mode. Cavitation characteristics were evaluated using three different methods, the probability method (based on [16]), the piecewise method (based on [17]), and our proposed method, the ratio method.

It was observed that, with some minor discrepancies, all microbubble contrast agents in bulk solution behaved in a similar way. That is, harmonic/ultraharmonic content as well as broadband noise increased at relatively the same rate between all microbubble formulations. This is confirmed through evaluating the inertial cavitation thresholds interpreted from the three different methods, where the cavitation thresholds of all contrast agents, regardless of technique were within a 200 kPa range. If just the probability method and the ratio method are considered, the cavitation threshold range is even smaller; between 150 and 300 kPa. Furthermore, the relative trends between microbubbles remained the same. Optison and SonoVue showed the lowest thresholds, while "Definity-like" and Sonazoid showed the highest thresholds. There were potentially anomalous thresholds calculated when using the piecewise method (notably, the low Optison value), which could be mitigated with a finer pressure spacing. It is worth noting that the inertial cavitation thresholds calculated using the probability method and the piecewise method require a baseline value, which is not required when using the ratio method. That being said, only the probability method has the ability to determine whether an individual microbubble echo resulted in inertial cavitation (provided a baseline is also known). All methods explored have the capability of evaluating single emissions, unlike ICD measurements performed elsewhere, which make them more convenient for implementation on an imaging system.

The small range of thresholds measured is likely a result of the polydisperse nature of the microbubbles; exemplified in **Table 2.1**, where there is large variability in microbubble size, indicated by standard deviations that range from 50-100% of the mean. It has been shown in prior studies that microbubble size plays a role in cavitation behavior [32]. However, with the exception being that there would be more clearance of large bubbles due to the lungs, this polydisperse nature is to be expected in clinical grade formulations *in vivo*. Indeed, some of the discrepancies could be explained by small deviations in size; Optison had the smallest average size (by number) and generated the weakest signal beyond 0.5 MPa. Regardless, the differences were minimal. All this suggests that in bulk polydisperse solutions, inertial cavitation generation may be pressure-dependent but not necessarily microbubble-dependent [18]. The small discrepancies in behavior may still be of importance in certain applications where a high degree of sensitivity is required; for example, that the inertial cavitation threshold of Optison and SonoVue appear to occur at low excitation pressures. These findings could inform pressure and microbubble choices for different

desired outcomes [22]. Indeed, this is consistent with a study that found that SonoVue was the most effective contrast agent for low-MI BBB opening [18] (Optison was not tested in this study). Furthermore, Sonazoid might be the most appropriate choice for applications where high intensities are desired, such as bubble-enhanced heating [33] or vascular disruption [34]. Clinically, Sonazoid is actually recommended for use at higher MIs (MI=0.1-0.2), opposed to other agents that are typically used at MIs between 0.06 to 0.1 for diagnostic imaging [35].

Another important observation was that inertial cavitation, defined here as when broadband noise begins to increase at a higher rate relative to the harmonics, occurs at relatively low pressures. This is not new information; studies from the past 20 years have suggested that inertial cavitation thresholds exist anywhere in the range of 0.1 MPa [5], [14] to 0.5 MPa [23] all the way up to 1 MPa [19] at 1 MHz transmit frequencies. We found that the inertial cavitation threshold of all microbubbles considered when exposed to 1 MHz ultrasound, regardless of technique, occurred in the range of 0.1 to 0.3 MPa, consistent with prior findings [36].

The thresholds calculated for all methods correspond to an MI of 0.1-0.3 at 1 MHz, within the recommended FDA diagnostic limit of 1.9. This suggests that inertial cavitation can happen at diagnostic MIs [37] – although not necessarily at diagnostic pulse lengths. Even that may not always be true, given that Doppler pulses have been shown to induce inertial cavitation [17], and Doppler signal can be enhanced using ultrasound contrast agents [38]. Indeed, the cavitation bioeffects caused by microbubbles insonated with standard Doppler pulses (4-6 cycles at MI = 1.3) have been employed for blood perfusion augmentation [39], [40]. Moreover, while prior studies have shown that cavitation threshold has a pulse length dependency [41], it is possible that even short imaging pulses at high MI may be enough to cause inertial cavitation. This will be investigated in future experiments. That being said, these experiments took place in degassed, deionized water. It has been reported that cavitation thresholds may be higher in tissue, due to changes in bubble dynamics in viscoelastic media [42] and spatial constraints in the microcirculation. Similarly, the effect of physiological flow may further complicate appropriate cavitation detection *in vivo* [43], [44]. Future studies will evaluate whether these trends are consistent in tissue, although it should be noted that many previously reported studies on inertial cavitation have taken place in degassed water [22], [27], [45].

When performing cavitation detection with the EPIQ and the C5-1 imaging array, we found that the trends may be visualized in real-time, when specific receive path optimization was implemented over the frequency bands of interest according to our findings. We utilized a 3.25 MHz filter with a bandwidth of 0.3 MHz in order to observe broadband noise characteristics. This frequency range was chosen as the point at which the frequency response of the array was relatively flat and near its center frequency (see **Fig. 2.7**). Cavitation signals were easily observable, and intensity increased with increasing transmit pressure. Observing inertial cavitation in real time with a scanner simply requires synchronizing the triggering of the cavitation source with the scanner, optimizing the receive path and setting an appropriate gain threshold so that signals are only detected when there is inertial cavitation. Although lacking accurate spatial localization, there are still many benefits that using a clinical device has over current techniques. The multi-element nature of the C5-1 means that it can receive signals from a much larger region and the user may easily adjust the imaging plane and select azimuthal focus. Therefore, it does not necessarily need to be confocally aligned with the source of cavitation signals in order to provide real-time cavitation information, as single element transducers generally must be in order to have adequate SNR. Furthermore, since clinical scanners are already allowed for patient use, and no change to the transmit pulses is necessary for passive cavitation detection, they may be immediately used in clinics. At the present time we suggest using B-mode or contrast imaging to accurately select the imaging plane that needs to be monitored for inertial cavitation, before switching to the passive cavitation mode developed here. In a future implementation, we will utilize a dual imaging path of scanners where a passive cavitation image will be overlaid with a low MI conventional image in a continuous fashion.

Although care was taken to evaluate cavitation characteristics in a precise and rigid manner, testing all possible excitation parameters was not possible. We chose to focus only on one frequency (1 MHz) and one tone burst length (40 cycles) in order to make concrete conclusions about the differences between microbubbles. Furthermore, we wanted to avoid both the spectral leakage due to short pulses as well as microbubble movement and acoustic streaming due to pulses longer than 200 cycles [28], [46]. It was also our intent to study acoustic conditions that would be used for treatment, not imaging, in which a 40-cycle pulse length at 1 MHz represents a typical parameter

set. Although we chose to only evaluate two microbubbles (SonoVue and “Definity-like”) when using the clinical scanner, we believe that two points of comparison is sufficient to evaluate the ability of clinical scanners to receive and display inertial cavitation images in real-time. Similarly, despite finding a rough estimate of cavitation threshold, a finer discretization of transmit pressures could have made these transitions clearer. That said, the discretization scheme used is similar to other works published also evaluating inertial cavitation thresholds [9], [29], [43], and despite the step size, all analysis methods investigated resulted in similar inertial cavitation thresholds. More importantly, given that the polydisperse nature of the formulations yielded high variability in scattered response, it is unlikely that a finer discretization would add value to the study. Future work will involve evaluating cavitation thresholds of monodisperse versus polydisperse formulations. Finally, although we took measures to limit large bubbles from being included in the focal region by drawing bubbles from the bottom of the vial (after it had sat for 60 s), it is likely that there were microbubbles present that were outside of the diameters that would be clinically relevant (after passage through the lungs). However, these microbubbles were outside of the resonance frequency of the transmit pulse and likely would not have caused significant errors.

2.5 CONCLUSION

Through this work, we have shown that common commercial microbubble formulations in bulk solution demonstrated cavitation behavior with similar spectral content. We evaluated cavitation behavior using two reported techniques and one technique developed here and found that the inertial cavitation threshold of common commercial microbubbles occurs between 0.1-0.3 MPa, regardless of methodology. The slight variation between formulations may be due to differences in overall particle size, shell properties, and dispersity. Finally, we have shown that a diagnostic ultrasound device may be used as a passive cavitation detector and can identify cavitation behavior in real-time, provided that there is an ability to synchronize triggering between the scanner and the treatment source. The use of a commercial scanner as a passive cavitation detection device opens many opportunities in guiding therapeutic ultrasound procedures such as microbubble-mediated drug delivery and thermal ablation. Future work in this area will be to incorporate spatial localization of cavitation signals on a clinical scanner.

2.6 ACKNOWLEDGMENTS

This work was supported by a grant from the U.S. Department of Defense (CA160415/PRCRP).

We gratefully acknowledge GE Healthcare for the Sonazoid and Optison used in this study.

2.7 REFERENCES

[1] K. Ferrara, R. Pollard, and M. Borden, "Ultrasound Microbubble Contrast Agents: Fundamentals and Application to Gene and Drug Delivery," *Annu. Rev. Biomed. Eng*, vol. 9, pp. 415–47, 2007.

[2] C. D. Arvanitis, M. Bazan-Peregrino, B. Rifai, L. W. Seymour, and C. C. Coussios, "Cavitation-Enhanced Extravasation for Drug Delivery," *Ultrasound Med. Biol.*, vol. 37, no. 11, pp. 1838–1852, Nov. 2011.

[3] I. Lentacker, I. De Cock, R. Deckers, S. C. De Smedt, and C. T. W. Moonen, "Understanding ultrasound induced sonoporation: Definitions and underlying mechanisms," *Adv. Drug Deliv. Rev.*, vol. 72, pp. 49–64, 2014.

[4] K. B. Bader and C. K. Holland, "Gauging the likelihood of stable cavitation from ultrasound contrast agents.," *Phys. Med. Biol.*, vol. 58, no. 1, pp. 127–44, Jan. 2013.

[5] W.-S. Chen, T. J. Matula, A. A. Brayman, and L. A. Crum, "A comparison of the fragmentation thresholds and inertial cavitation doses of different ultrasound contrast agents," *J. Acoust. Soc. Am.*, vol. 113, no. 1, pp. 643–651, Jan. 2003.

[6] N. McDannold, N. Vykhodtseva, and K. Hynynen, "Targeted disruption of the blood–brain barrier with focused ultrasound: association with cavitation activity," *Phys. Med. Biol.*, vol. 51, no. 4, pp. 793–807, Feb. 2006.

[7] D. E. Goertz *et al.*, "Antitumor Effects of Combining Docetaxel (Taxotere) with the Antivascular Action of Ultrasound Stimulated Microbubbles," *PLoS One*, vol. 7, no. 12, p. e52307, Dec. 2012.

[8] G. Dimcevski *et al.*, "A human clinical trial using ultrasound and microbubbles to enhance gemcitabine treatment of inoperable pancreatic cancer," *J. Control. Release*, vol. 243, pp. 172–181, Dec. 2016.

[9] Y.-S. Tung, J. J. Choi, B. Baseri, and E. E. Konofagou, "Identifying the Inertial Cavitation Threshold and Skull Effects in a Vessel Phantom Using Focused Ultrasound and Microbubbles," *Ultrasound Med. Biol.*, vol. 36, no. 5, pp. 840–852, May 2010.

[10] D. McMahon, C. Poon, and K. Hynynen, "Evaluating the safety profile of focused ultrasound and microbubble-mediated treatments to increase blood-brain barrier permeability," *Expert Opin. Drug Deliv.*, vol. 16, no. 2, pp. 129–142, Feb. 2019.

[11] S. Xu *et al.*, "Correlation Between Brain Tissue Damage and Inertial Cavitation Dose Quantified Using Passive Cavitation Imaging," *Ultrasound Med. Biol.*, vol. 45, no. 10, pp. 2758–2766, Oct. 2019.

[12] J.-M. Hyvelin *et al.*, "Characteristics and Echogenicity of Clinical Ultrasound Contrast Agents: An In Vitro and In Vivo Comparison Study," *J. Ultrasound Med.*, vol. 36, no. 5, pp. 941–953, May 2017.

[13] C. Tremblay-Darveau *et al.*, "The Role of Microbubble Echo Phase Lag in Multipulse Contrast-Enhanced Ultrasound Imaging," *IEEE Trans. Ultrason. Ferroelectr. Freq.*

Control, vol. 65, no. 8, pp. 1389–1401, Aug. 2018.
[14] X. Guo, Q. Li, Z. Zhang, D. Zhang, and J. Tu, "Investigation on the inertial cavitation threshold and shell properties of commercialized ultrasound contrast agent microbubbles," *J. Acoust. Soc. Am.*, vol. 134, no. 2, pp. 1622–1631, Aug. 2013.
[15] J. Tu, T. J. Matula, A. A. Brayman, and L. A. Crum, "Inertial cavitation dose produced in ex vivo rabbit ear arteries with Optison by 1-MHz pulsed ultrasound.," *Ultrasound Med. Biol.*, vol. 32, no. 2, pp. 281–8, Feb. 2006.
[16] M. L. Fabiilli, K. J. Haworth, N. H. Fakhri, O. D. Kripfgans, P. L. Carson, and J. B. Fowlkes, "The role of inertial cavitation in acoustic droplet vaporization.," *IEEE Trans. Ultrason. Ferroelectr. Freq. Control*, vol. 56, no. 5, pp. 1006–17, May 2009.
[17] K. Radhakrishnan *et al.*, "Relationship between cavitation and loss of echogenicity from ultrasound contrast agents.," *Phys. Med. Biol.*, vol. 58, no. 18, pp. 6541–63, Sep. 2013.
[18] S.-K. Wu *et al.*, "Characterization of Different Microbubbles in Assisting Focused Ultrasound-Induced Blood-Brain Barrier Opening," *Sci. Rep.*, vol. 7, no. 1, p. 46689, May 2017.
[19] W.-S. Chen, A. A. Brayman, T. J. Matula, and L. A. Crum, "Inertial cavitation dose and hemolysis produced in vitro with or without Optison®," *Ultrasound Med. Biol.*, vol. 29, no. 5, pp. 725–737, May 2003.
[20] K. J. Haworth, K. B. Bader, K. T. Rich, C. K. Holland, and T. D. Mast, "Quantitative Frequency-Domain Passive Cavitation Imaging," *IEEE Trans. Ultrason. Ferroelectr. Freq. Control*, vol. 64, no. 1, pp. 177–191, Jan. 2017.
[21] E. Lyka, C. M. Coviello, C. Paverd, M. D. Gray, and C.-C. Coussios, "Passive Acoustic Mapping using Data-Adaptive Beamforming Based on Higher-Order Statistics," *IEEE Trans. Med. Imaging*, pp. 1–1, 2018.
[22] F. Vignon *et al.*, "Microbubble cavitation imaging," *IEEE Trans. Ultrason. Ferroelectr. Freq. Control*, vol. 60, no. 4, pp. 661–670, Apr. 2013.
[23] C. H. Farny, R. G. Holt, and R. A. Roy, "Temporal and Spatial Detection of HIFU-Induced Inertial and Hot-Vapor Cavitation with a Diagnostic Ultrasound System," *Ultrasound Med. Biol.*, vol. 35, no. 4, pp. 603–615, Apr. 2009.
[24] P. Qin, L. Xu, T. Han, L. Du, and A. C. H. Yu, "Effect of non-acoustic parameters on heterogeneous sonoporation mediated by single-pulse ultrasound and microbubbles," *Ultrason. Sonochem.*, vol. 31, pp. 107–115, 2016.
[25] C. M. Coviello, S. R. Faragher, and C. Coussios, "Robust Capon beamforming for passive cavitation mapping during high-intensity focused ultrasound therapy.," *J. Acoust. Soc. Am.*, vol. 128, no. 4, pp. 2280–2280, Oct. 2010.
[26] I. De Cock *et al.*, "Ultrasound and microbubble mediated drug delivery: acoustic pressure as determinant for uptake via membrane pores or endocytosis," *J. Control. Release*, vol. 197, pp. 20–28, 2015.
[27] D. A. King, M. J. Malloy, A. C. Roberts, A. Haak, C. C. Yoder, and W. D. O'Brien, "Determination of postexcitation thresholds for single ultrasound contrast agent microbubbles using double passive cavitation detection," *J. Acoust. Soc. Am.*, vol. 127, no. 6, pp. 3449–3455, Jun. 2010.
[28] S. Keller, M. Bruce, and M. A. Averkiou, "Ultrasound Imaging of Microbubble Activity during Sonoporation Pulse Sequences," *Ultrasound Med. Biol.*, vol. 45, no. 3, 2019.
[29] Y. Lin *et al.*, "Effect of acoustic parameters on the cavitation behavior of SonoVue microbubbles induced by pulsed ultrasound," *Ultrason. Sonochem.*, vol. 35, pp. 176–184,

Mar. 2017.
[30] T. G. Leighton, *The acoustic bubble*. Academic Press, 1994.
[31] A. D. Maxwell, C. A. Cain, T. L. Hall, J. B. Fowlkes, and Z. Xu, "Probability of cavitation for single ultrasound pulses applied to tissues and tissue-mimicking materials.," *Ultrasound Med. Biol.*, vol. 39, no. 3, pp. 449–65, Mar. 2013.
[32] J. E. Chomas, P. Dayton, D. May, and K. Ferrara, "Threshold of fragmentation for ultrasonic contrast agents," *J. Biomed. Opt.*, vol. 6, no. 2, p. 141, 2001.
[33] S. D. Sokka, R. King, and K. Hynynen, "MRI-guided gas bubble enhanced ultrasound heating in *in vivo* rabbit thigh," *Phys. Med. Biol.*, vol. 48, no. 2, pp. 223–241, Jan. 2003.
[34] J. Wang *et al.*, "Selective depletion of tumor neovasculature by microbubble destruction with appropriate ultrasound pressure," *Int. J. Cancer*, vol. 137, no. 10, pp. 2478–2491, Nov. 2015.
[35] J. Y. Jang *et al.*, "Current consensus and guidelines of contrast enhanced ultrasound for the characterization of focal liver lesions," *Clin. Mol. Hepatol.*, vol. 19, no. 1, p. 1, 2013.
[36] S. Datta *et al.*, "Correlation of cavitation with ultrasound enhancement of thrombolysis," *Ultrasound Med. Biol.*, vol. 32, no. 8, pp. 1257–1267, Aug. 2006.
[37] R. E. Apfel and C. K. Holland, "Gauging the likelihood of cavitation from short-pulse, low-duty cycle diagnostic ultrasound," *Ultrasound Med. Biol.*, vol. 17, no. 2, pp. 179–185, Jan. 1991.
[38] T. Albrecht *et al.*, "Prolongation and optimization of Doppler enhancement with a microbubble US contrast agent by using continuous infusion: preliminary experience.," *Radiology*, vol. 207, no. 2, pp. 339–47, May 1998.
[39] O. R. Mason *et al.*, "Augmentation of Tissue Perfusion in Patients With Peripheral Artery Disease Using Microbubble Cavitation," *JACC Cardiovasc. Imaging*, vol. 13, no. 3, pp. 641–651, Mar. 2020.
[40] J. T. Belcik *et al.*, "Augmentation of Muscle Blood Flow by Ultrasound Cavitation Is Mediated by ATP and Purinergic Signaling.," *Circulation*, vol. 135, no. 13, pp. 1240–1252, Mar. 2017.
[41] W.-S. Chen, A. A. Brayman, T. J. Matula, L. A. Crum, and M. W. Miller, "The pulse length-dependence of inertial cavitation dose and hemolysis," *Ultrasound Med. Biol.*, vol. 29, no. 5, pp. 739–748, May 2003.
[42] C. C. Church and X. Yang, "A Theoretical Study of Gas Bubble Dynamics in Tissue," in *AIP Conference Proceedings*, 2006, vol. 838, no. 1, pp. 217–224.
[43] M. Cheng, F. Li, T. Han, A. C. H. Yu, and P. Qin, "Effects of ultrasound pulse parameters on cavitation properties of flowing microbubbles under physiologically relevant conditions," *Ultrason. Sonochem.*, vol. 52, pp. 512–521, Apr. 2019.
[44] J. J. Choi and C.-C. Coussios, "Spatiotemporal evolution of cavitation dynamics exhibited by flowing microbubbles during ultrasound exposure," *J. Acoust. Soc. Am.*, vol. 132, no. 5, pp. 3538–3549, Nov. 2012.
[45] E. Sassaroli and K. Hynynen, "Cavitation threshold of microbubbles in gel tunnels by focused ultrasound.," *Ultrasound Med. Biol.*, vol. 33, no. 10, pp. 1651–60, Oct. 2007.
[46] C. Mannaris and M. A. Averkiou, "Investigation of Microbubble Response to Long Pulses Used in Ultrasound-Enhanced Drug Delivery," *Ultrasound Med. Biol.*, vol. 38, no. 4, pp. 681–691, Apr. 2012.

Chapter 3. INVESTIGATION OF THE PHASE OF NONLINEAR ECHOES DURING AMPLITUDE MODULATION[2]

Sara B. Keller, Ting Yu Lai, Lance De Koninck, Michalakis A. Averkiou

Abstract

Contrast-enhanced ultrasound imaging relies on distinguishing between microbubble and tissue echoes. Amplitude modulation, a nonlinear pulsing scheme, has been developed to take advantage of amplitude-dependent nonlinearity of microbubble echoes. However, with amplitude modulation tissue can also generate harmonics that can degrade image contrast. Segmentation of contrast-enhanced ultrasound images based on amplitude-dependent phase difference in the echoes, defined in the present manuscript as $\Delta\Phi_{AM}$, has been proposed as an additional method of enhancing contrast-to-tissue ratio as tissue is not expected to create the same degree of $\Delta\Phi_{AM}$, however this has not been robustly investigated. In this work, we evaluate the source of $\Delta\Phi_{AM}$ through simulations of unshelled versus shelled microbubble oscillation and simulations of nonlinear propagation in tissue. We then validate the simulated $\Delta\Phi_{AM}$ results with experimental $\Delta\Phi_{AM}$ measurements during *in vitro* scattering and imaging in a flow phantom. We show that shelled and unshelled microbubbles resulted in a $\Delta\Phi_{AM}$ with similar overall magnitude with some differences in trends, and that tissue echoes have a small degree of $\Delta\Phi_{AM}$ due to nonlinear propagation. The results from this work can help inform optimal parameter selection for phase segmentation.

3.1 INTRODUCTION

Contrast enhanced ultrasound (CEUS) has emerged as an important tool for vascular imaging. Microbubble ultrasound contrast agents are similar in size to red blood cells which allows them to provide contrast enhancement in capillaries and microvessels [1], [2]. Due to their unique scattering properties, microbubble signal can be distinguished from tissue signal, and therefore

[2] *Manuscript in preparation for submission to IEEE Trans. Ultrason. Freq. Control*

make an excellent diagnostic tool for observing real-time vascular structure and blood perfusion [1], [3], [4].

Microbubble contrast during CEUS is a result of microbubble echoes being nonlinear and containing harmonic components in their spectra while tissue echoes are mostly linear [1], [5]. The degree of nonlinearity is dependent on the amplitude of the ultrasound wave; higher amplitudes result in a greater nonlinear response [6]. In order to isolate the unique frequency components of microbubble echoes, nonlinear pulsing schemes including pulse inversion (PI), amplitude modulation (AM), and amplitude modulated pulse inversion (AMPI) have been developed [1], [5], [6]. Tissue signal suppression is important in CEUS to achieve good image contrast and microbubble specificity [7]. Incomplete tissue signal cancellation may mask real enhancement caused by microbubbles or be incorrectly interpreted as real enhancement [1]. Previous studies have shown that AM has better tissue signal suppression than that of PI [1], [8], [9]. For this work, we focus on AM, a nonlinear pulsing scheme that involves transmitting 2 or more pulses at different amplitudes. A widely used version of AM is one where the amplitude of the second pulse (p_{half}) is half that of the first pulse (p_{full}). The linear response in the echoes is removed by scaling the echoes of p_{half} by a factor of 2 and then subtracting them from the echoes of p_{full} [1].

The image quality of CEUS is also limited by the tissue harmonics generated from the nonlinear propagation of sound waves in tissue. Optimal CEUS imaging is performed at low mechanical index (MI $\leq$0.1) to avoid microbubble destruction and the generation of tissue harmonics, which may interfere with or mask the microbubble signals in CEUS images [10]. However, even at low MIs, tissue still generates some nonlinear response, which degrades the overall contrast-to-tissue ratio (CTR) of CEUS [11], [12]. Recently, it has been proposed that utilizing other unique microbubble echo signal properties could be used as an additional method of tissue signal suppression during AM imaging. Particularly, it has been shown that microbubble echoes not only exhibit amplitude-dependent nonlinearity, but also an amplitude-dependent difference in phase during AM imaging. We refer to this phase difference as $\Delta\Phi_{AM}$, which is the difference in phase between the echoes of p_{full} and p_{half}. Using a pre-determined $\Delta\Phi_{AM}$ as a threshold for image segmentation has been used to improve the CTR of CEUS images, as AM sequences in tissue are not expected to result in the same degree of $\Delta\Phi_{AM}$ [13]. Tremblay-Darveau, et al. posited that

$\Delta\Phi_{AM}$ is a result of the buckling dynamics of shelled microbubbles, which was demonstrated with the Marmottant model [13], [14]. Additionally, they found that $\Delta\Phi_{AM}$ was generally negative, indicating the phase of the echo from p_{full} lags that of p_{half} [13]. According to Tremblay-Darveau, since $\Delta\Phi_{AM}$ is attributed to the bubble shell, it is not expected to occur in tissue or in unshelled bubbles.

We hypothesize, however, that $\Delta\Phi_{AM}$ may also occur to some degree during nonlinear propagation in tissue and nonlinear oscillations of the gas core itself in addition to the impact of shell properties. To the best of our knowledge, $\Delta\Phi_{AM}$ resulting from nonlinear propagation and echoes from unshelled microbubbles (derived from simulations) have not yet been reported. We believe that a robust analysis of the source of $\Delta\Phi_{AM}$ could help derive optimal conditions for phase segmentation. We evaluate this through simulations of unshelled versus shelled microbubble oscillation with the Rayleigh-Plesset [15] and Marmottant equations [14], respectively and simulations of nonlinear propagation in tissue with the Khokhlov-Zabolotskaya-Kuznetsov (KZK) equation [16], [17]. We then validate the simulated $\Delta\Phi_{AM}$ results with experimental $\Delta\Phi_{AM}$ measurements during *in vitro* scattering and AM imaging in a flow phantom. We performed these experiments on three commercially available ultrasound contrast agents: Optison, Sonazoid, and SonoVue, to evaluate the impact of various microbubble formulations on $\Delta\Phi_{AM}$. The results from this work further elucidate the source of $\Delta\Phi_{AM}$ which can both improve phase segmentation to increase CTR during AM imaging and raise the possibility of implementing phase segmentation on imaging applications outside of CEUS.

3.2 THEORY

3.2.1 *Phase calculations*

All simulated and experimentally captured waveforms were analyzed using the following methodology. For the echoes from the p_{full} and p_{half} pair (referred to as an AM echo pair), the waveforms were first filtered using an FIR bandpass filter centered around the center frequency of the transmit pulse, as we chose to evaluate phase at the fundamental frequency [13]. The filtered pulses were then converted to their analytic signal using a Hilbert Transform, which resulted in

waveforms that contained both real and imaginary components. Phase at each time point for each waveform in the AM pair was then calculated as follows,

$$\Phi_{full}(t) = \angle ps_{full}(t) \text{ (3.1)}$$
$$\Phi_{half}(t) = \angle ps_{half}(t), \text{ (3.2)}$$

where $\angle$ is the "angle" operator on the analytic signals. $ps_{full}(t)$ and $ps_{half}(t)$ are the echoes of p_{full} and p_{half} at each time point, respectively. The difference in phase, $\Delta\Phi_{AM}(t)$, between the AM pair was calculated at each time point,

$$\Delta\Phi_{AM}(t) = \Phi_{full}(t) - \Phi_{half}(t) \text{ (3.3)}$$

and then averaged over the pulse duration to get a single value of $\Delta\Phi_{AM}$ for each AM pair. This signal processing method for calculating $\Delta\Phi_{AM}$ was used for all subsequent phase analyses.

3.2.2 *Rayleigh-Plesset model for unshelled bubbles*

Unshelled bubble nonlinear oscillation was modeled with the Rayleigh-Plesset equation [18],

$$\rho_L\left(R\ddot{R} + \tfrac{3}{2}\dot{R}^2\right) = \left(P_0 + \tfrac{2\sigma_W}{R_0}\right)\left(\tfrac{R_0}{R}\right)^{3\kappa}\left(1 - \tfrac{3\kappa\dot{R}}{c}\right) - \tfrac{2\sigma_W}{R} - \tfrac{4\mu_L\dot{R}}{R} - P_0 - P_A(t), \quad (3.4)$$

where *R(t)* is the microbubble radius, ρ_L is the liquid density, P_0 is the static fluid pressure, σ is the surface tension, R_0 is the equilibrium radius, κ is the polytropic gas constant, c is the speed of sound, μ_L is the liquid viscosity and $P_A(t)$ is the applied pressure (ie, the ultrasound pressure).

Scattered echoes from unshelled bubbles insonified with a 1.7 MHz, 4-cycle pulse with pressures ranging from 0.005 to 0.2 MPa were modeled. Microbubble oscillation was simulated using the following parameters: ρ_L = 1000 kg/m^3, P_0 = 100 kPa, σ_w = 0.0725 N/m, κ = 1.1, c = 1486 m/s, μ_L = 0.001 Pa·s for microbubble radii (R_0) spanning from 0.5 to 3 μm. $\Delta\Phi_{AM}$ of all AM pairs was calculated using the methodology described in **Section 3.2.1**.

3.2.3 *Marmottant model for shelled bubbles*

Shelled microbubble oscillation was modeled with the Marmottant Equation, which is merely the Rayleigh-Plesset equation with added surface tension terms [14]:

$$\rho_L\left(R\ddot{R}+\tfrac{3}{2}\dot{R}^2\right)=\left(P_0+\tfrac{2\sigma(R_0)}{R_0}\right)\left(\tfrac{R_0}{R}\right)^{3\kappa}\left(1-\tfrac{3\kappa\dot{R}}{c}\right)-\tfrac{2\chi}{R}\left(\tfrac{R^2}{{R_0}^2}-1\right)-\tfrac{4\mu_L\dot{R}}{R}-\tfrac{4\kappa_S\dot{R}}{R^2}-P_0-P_A(t). \quad (3.5)$$

κ_s is the shell viscosity, χ is the shell elasticity, and $\sigma(R)$ is the spatially varying surface tension at the bubble wall, is defined by [14]

$$\sigma(R)=\begin{cases}0, & R<R_{buck}\\ \chi_0\left(\frac{R^2}{R_{buck}}-1\right), & R_{buck}<R<R_{break}\\ \sigma_w, & R>R_{break}\end{cases}, \quad (3.6)$$

where R_{buck} and R_{break} define the buckle and rupture radius of the microbubble shell, respectively.

The same parameters were used to simulate the shelled bubbles as the free gas bubbles, with the addition of $\kappa_s = 1.5 \times 10^{-8}$ kg/s and $\chi = 1.55$. R_{buck} and R_{break} were defined to be 99% and 102% of the starting radius, respectively. $\Delta\Phi_{AM}$ of all AM pairs was calculated using the methodology described in **Section 3.2.1**.

3.2.4 *Nonlinear parabolic wave equation (KZK equation)*

The KZK nonlinear parabolic wave equation has been used to model the nonlinear propagation of finite amplitude pulses from focused sound beams in thermoviscous fluids [19]–[21]. $\Delta\Phi_{AM}$ due to nonlinear propagation was evaluated by considering the phases of the propagated pulses at different amplitudes and assuming that the tissue echoes would be similar due to linear tissue scattering. More details of the numerical model were presented previously [22].

The assumed source in the simulations was a focused circular source with a radius of 8.6 mm and a focal length of 70 mm. A 4-cycle pulse at 2 MHz was transmitted with source pressures ranging from 0.04 to 1.2 MPa. The nonlinearly propagated pulses at 0.5, 1, and 1.5 focal distances along

the propagation axis were recorded for each AM pair. We used the following acoustic parameters for nonlinear simulations in tissue: speed of sound $c = 1540\ \mathrm{m/s}$, density $\rho = 1000\ \mathrm{kg/m^3}$, absorption coefficient of 0.3 dB/cm at 1 MHz, and nonlinearity coefficient $\beta = 5$.

$\Delta\Phi_{AM}$ of all AM pairs was calculated using the methodology described in **Section 3.2.1**. To highlight the dependence of axial distance on harmonic phase content, the absolute phase (not $\Delta\Phi_{AM}$) of a pulse, with a source pressure of 1.2 MPa, as it propagates along the source axis was calculated from the FFT of the waveform.

3.3 MATERIALS AND METHODS

In order to validate the theoretical results, $\Delta\Phi_{AM}$ was measured both using single element transducers in an *in vitro* scattering experiment and a clinical scanner while scanning microbubbles flowing in a tissue flow phantom. For all experiments, SonoVue (Bracco Suisse SA, Geneva, Switzerland), Sonazoid (GE Healthcare, Chicago, IL, USA), and Optison (GE Healthcare, Chicago, IL, USA) were resuspended according to the manufacturer's instructions. Microbubble concentration from the vials was estimated from our previous study to be between 1-5 $\times$ 10^8 microbubbles/mL for all formulations [23].

3.3.1 In vitro *microbubble scattering*

The experimental setup used for microbubble scattering experiments can be seen in **Fig. 3.1**. A Tektronix AFG 3102C Arbitrary Waveform Generator was used to generate each AM pair. This was accomplished by utilizing both Channel 1 for p_{full} and Channel 2 connected to the 'Add Input' connection on the back of the oscilloscope for p_{half}. The p_{half} was sent after a 500 μs time delay to mimic an average pulse repetition frequency of imaging systems. The p_{full} and delayed p_{half} were sent through an ENI 2200L RF Amplifier (ENI, Rochester, NY). This signal was then sent to a focused transducer (V304, diameter = 2.54 cm, focal distance = 7.6 cm, center frequency = 2.25 MHz, Olympus NDT, Waltham, MA, USA), which was used as the source of microbubble excitation. This transducer was operated at a frequency of 1.7 MHz. A focused transducer (C304, diameter = 2.54 cm, focal distance = 7.6 cm, center frequency = 2.25 MHz, Olympus NDT,

Waltham, MA, USA) was confocally aligned at a 90° angle with the V304 and recorded scattered microbubble echoes.

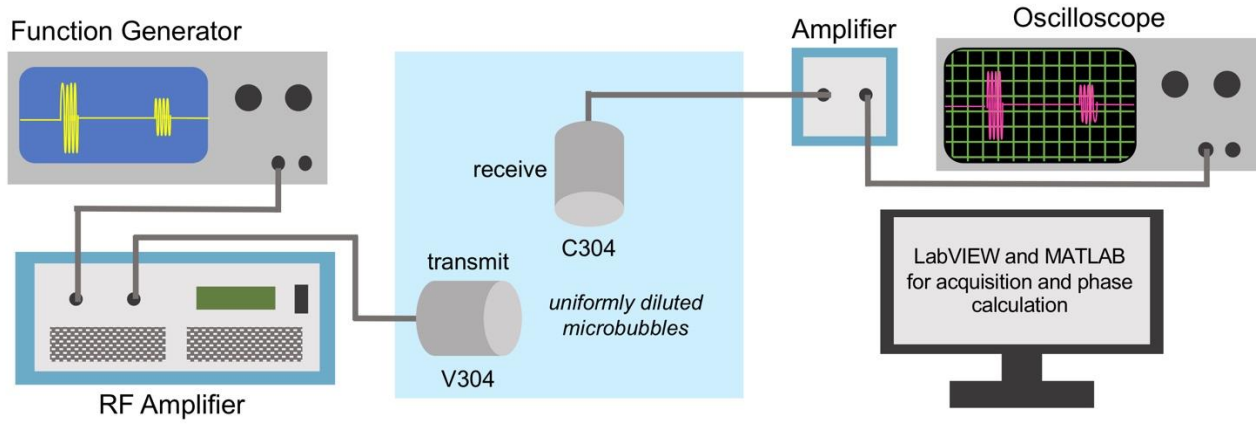

Fig. 3.1: Experimental setup for in vitro scattering experiments.

Microbubbles were added directly into the water tank at a concentration of 10^4 microbubbles/mL, consistent with our prior work [23]. For each experiment, a new vial of microbubbles was used, and microbubble presence was confirmed through observation of scattered signal. The p_{full} and p_{half} pulse sequences were sent through the V304 at acoustic pressures ranging from 40 kPa (the smallest p_{half}) to 160 kPa (the largest p_{full}). The signals were then received by the C308, amplified by 20 dB using a variable gain pulser-receiver (Panametrics, Waltham, MA, USA), and digitized using a DPO7054C Oscilloscope (Tektronix Inc., Beaverton, OR) with a sampling frequency of 500 MHz. A custom LabVIEW program was used to acquire 20 echoes per pressure setting. Calculation of $\Delta\Phi_{AM}$ was performed in MATLAB (The MathWorks, Inc., Natick, MA, USA) as described in **Section 3.2.1**; however, only scattered pulses with an amplitude three times above noise were evaluated, in order to ensure sufficient signal-to-noise ratio. Noise in this case was defined as the average amplitude between a section of the received voltage signal in which scattering was not occurring. For comparison against a control, a 0.5 mm x 0.5 mm metal reflector was placed at the confocal area of both transducers. Reflection of sound off the reflector is not expected to generate $\Delta\Phi_{AM}$ at low excitation pressures.

3.3.2 *RF data acquisition in a flow phantom*

A Doppler flow phantom (Model 5230A-modified, ATS Laboratories, Bridgeport, CT) was connected to a flow system in a closed-loop setup, as seen in **Fig. 3.2**. A 1 L beaker filled with deionized water was connected to the system via ¼ inch inner diameter tygon silicon tubing that ran through a peristaltic pump system consisting of a Masterflex L/S Variable Drive (Model 07528, Cole Parmer, Vernon Hills, IL) and Easy-Load II pump head (Model 77200-62, Cole Parmer). The beaker was placed on a stir-plate with magnetic stirrer (ThermoFisher Scientific, Waltham, MA) to ensure appropriate microbubble mixing. SonoVue, Sonazoid, and Optison were added into the beaker at a dilution factor of 1:100,000. Two imaging transducers, the C5-1 and L12-5, operated by the Philips iU22 (Philips Healthcare, Bothell, WA) were coupled to the tissue phantom with ultrasound gel. The C5-1 and L12-5 transducers were operating in an AM contrast mode, using 4 pulses at a center frequency of 1.7 MHz and 4.1 MHz, respectively. Mechanical indexes (MIs) ranging from 0.06 to 0.21 were used. Radiofrequency (RF) data were acquired using specialized research settings. For each microbubble formulation and pressure, three RF frames were taken. The microbubbles were allowed to flow between each frame acquisition to limit microbubble destruction after one frame; however, the microbubbles were stationary during the acquisition to limit phase shift due to motion.

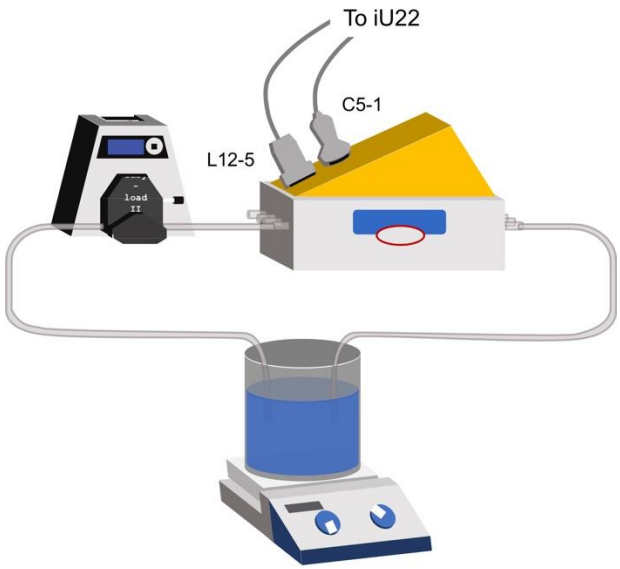

Fig. 3.2: Experimental setup for RF data acquisition of microbubbles in a flow phantom.

The RF data were imported into MATLAB for offline processing. RF data consist of post-beamformed imaging lines acquired prior to envelope detection and log-compression. Two regions of interest (ROIs) were created to evaluate $\Delta\Phi_{AM}$: one ROI within the tube (indicating microbubble signal) and one ROI above the tube (indicating tissue signal). $\Delta\Phi_{AM}$ was first calculated between a start and end time index (describing the depth of the ROI) as described in **Section 3.2.1** and then averaged over a start and end line index (describing the width of the ROI). Finally, $\Delta\Phi_{AM}$ was averaged over three frames for each MI tested.

3.4 RESULTS

3.4.1 $\Delta\Phi_{AM}$ *from unshelled and shelled bubbles*

Example radius- and scattered pressure-versus-time curves for unshelled bubbles generated by the Rayleigh-Plesset equation and for shelled bubbles generated by the Marmottant equation may be seen in **Fig. 3.3**. These results are from a 1, 2, and 3 μm radius bubble excited at 1.7 MHz. Just 0.04 and 0.08 MPa excitations are shown for simplicity. In **Fig. 3.4** we show the $\Delta\Phi_{AM}$ resulting from these bubble radii with all the pressure cases considered. Both shelled and unshelled bubbles exhibit a negative $\Delta\Phi_{AM}$, consistent with prior work. Furthermore, both shelled and unshelled bubbles show a $\Delta\Phi_{AM}$ with magnitude exceeding what has been previously used for phase segmentation (0.1-0.3 rad) [13]. However, where the $\Delta\Phi_{AM}$ of the unshelled bubble seems mostly dependent on pressure, the $\Delta\Phi_{AM}$ from the shelled bubble seems to be more heavily dependent on bubble radius, and indeed shows that lower acoustic pressures and larger bubble radii give a greater $\Delta\Phi_{AM}$. These results may also be visualized in the 2D plots shown in Fig. 5, in which a larger number of bubble radii were evaluated. In these maps, a greater magnitude $\Delta\Phi_{AM}$ is indicated by a yellow color. Notably, the resonance size of a free bubble excited at 1.7 MHz is about 1.5 μm in radius, calculated using the Minnaert formula [24]. This is consistent with the free bubble results showing that midrange radii have the largest $\Delta\Phi_{AM}$ (a) but are otherwise dependent on acoustic pressure. The $\Delta\Phi_{AM}$ resulting from shelled bubbles seems more prominent at large radii and small acoustic pressures for this driving frequency (b), as in **Fig. 3.4**. Interestingly, with increasing shell stiffness, the resonance frequency is known to increase [25], [26], which would ordinarily mean a decreased resonant microbubble size. This phenomenon was not observed in these results, as larger microbubbles gave a more pronounced $\Delta\Phi_{AM}$.

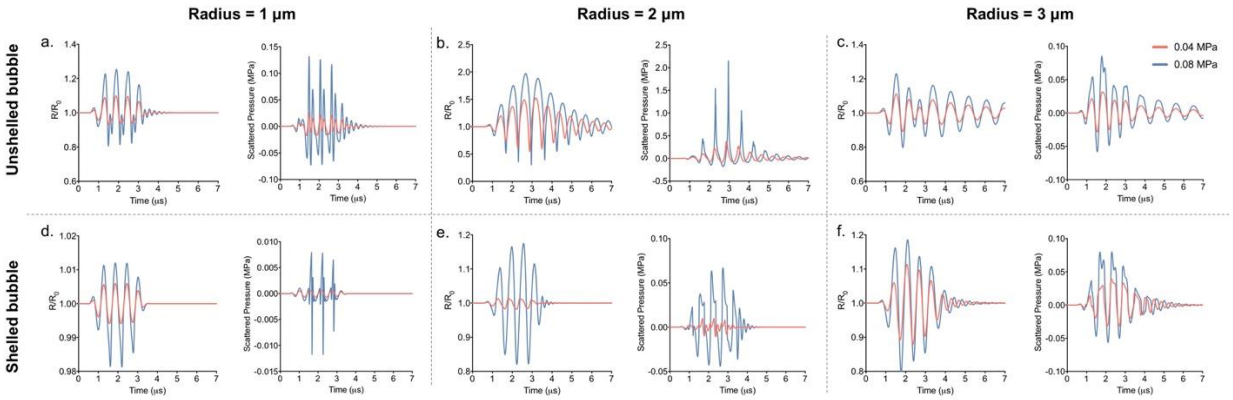

Fig. 3.3: Example radius- and scattered pressure-versus time curves.

Results are from 1, 2, and 3 μm radius unshelled or shelled bubbles. Just 0.04 and 0.08 MPa excitation cases are shown. Visible $\Delta\Phi_{AM}$ can be observed in several cases, such as (b) and (f).

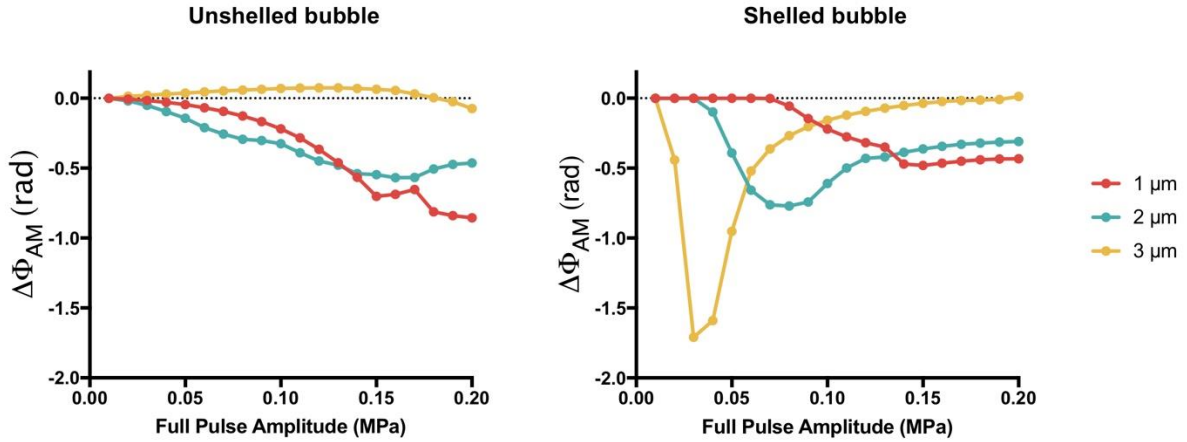

Fig. 3.4: $\Delta\Phi_{AM}$ as a function of the full pulse amplitude.

The unshelled bubble exhibits $\Delta\Phi_{AM}$ that mainly increases with increasing pressure, while the shelled bubble exhibits $\Delta\Phi_{AM}$ that is more prominent at large radii and small pressures

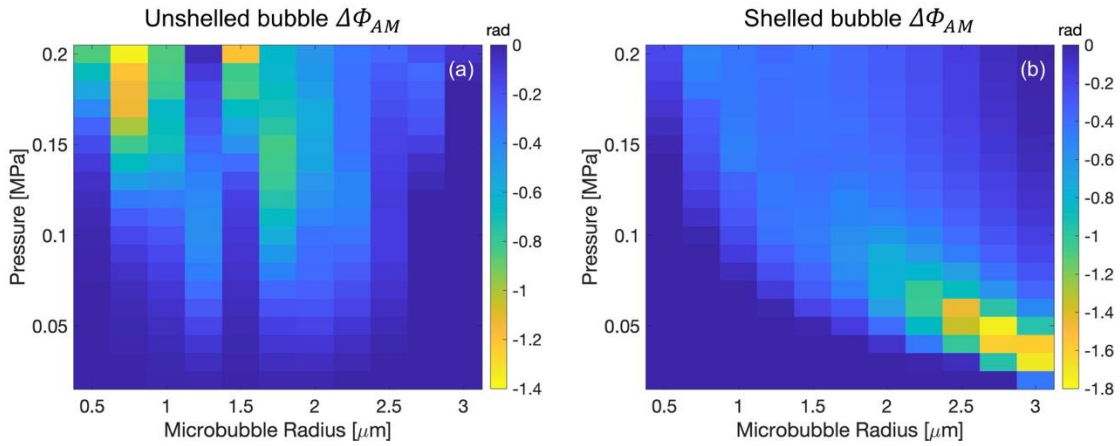

Fig. 3.5: $\Delta\Phi_{AM}$ resulting from unshelled and shelled bubbles.

As in Fig. 4, the $\Delta\Phi_{AM}$ resulting from the unshelled bubble seems mostly dependent on amplitude and to a somewhat lesser degree on bubble radius, while the $\Delta\Phi_{AM}$ from the shelled bubble seems more dependent on bubble size and is in fact more prominent at smaller acoustic pressures.

3.4.2 $\Delta\Phi_{AM}$ *from nonlinear propagation*

Simulated waveforms from nonlinear propagation modeled with the KZK equation at pre-, at- and post-focal axial distances and various pressures are shown in **Fig. 3.6 (a-c)**, respectively. **(d)** shows $\Delta\Phi_{AM}$ versus the source pressure of p_{full}. Interestingly, the $\Delta\Phi_{AM}$ trends change based on location; at the focus, $\Delta\Phi_{AM}$ decreases with increasing source pressure. Before the focus, $\Delta\Phi_{AM}$ increases with increasing source pressure. After the focus, $\Delta\Phi_{AM}$ both first increases and then decreases with increasing source pressure but remains positive for the amplitudes considered. Notably, the magnitude of $\Delta\Phi_{AM}$ is much lower in magnitude from nonlinear propagation (d) than microbubble oscillation (**Fig. 3.4**). **(e)** shows absolute phase (not $\Delta\Phi_{AM}$) from the first, second, and third harmonics at various axial locations from the highest source pressure (1.2 MPa). It can be seen that the different harmonics undergo roughly a 2π phase shift at the focus due to diffraction [10].

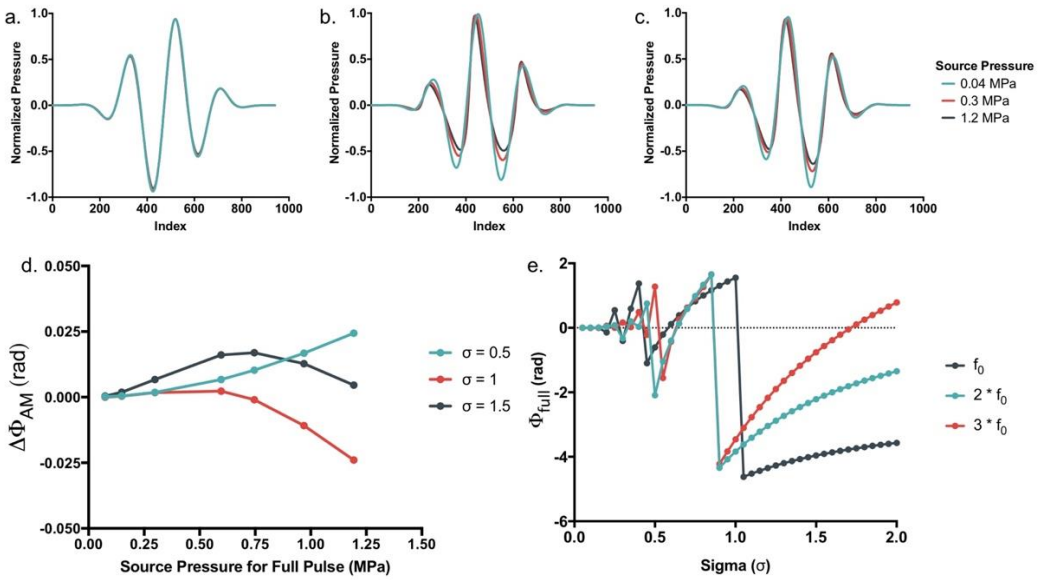

Fig. 3.6: $\Delta\Phi_{AM}$ results from nonlinear propagation.

(a) – (c) show pulses propagating nonlinearly in tissue at σ=0.5 (a), 1.0 (b), and 1.5 (c). Nonlinear behavior becomes much more prominent at and beyond the focus. (d) shows the calculated $\Delta\Phi_{AM}$ at each of these distances as a function of pressure. At the focus σ=1.0, $\Delta\Phi_{AM}$ decreases with increasing source pressure. Before the focus σ=0.5, $\Delta\Phi_{AM}$ increases with increasing source pressure. After the focus σ=1.5, $\Delta\Phi_{AM}$ first increases and then decreases with increasing source pressure but remains positive for the pressures considered. $\Delta\Phi_{AM}$ resulting from nonlinear propagation is much smaller in magnitude than the bubble simulations. (e) shows absolute phase of three harmonics at various axial locations from the highest source pressure (1.2 MPa). All harmonics show roughly a 2π phase shift approximately at the focus.

3.4.3 $\Delta\Phi_{AM}$ *from* in vitro *scattering*

Example scattered echoes from a linear reflector without microbubbles (a) and from SonoVue (b) when excited with a 0.2 MPa / 0.1 MPa AM pair can be seen in **Fig. 3.7**. Where the linear reflector scattered echoes that were well-defined and lacked any obvious $\Delta\Phi_{AM}$, microbubbles scattered much more irregular echoes that were lower in amplitude and had visible $\Delta\Phi_{AM}$.

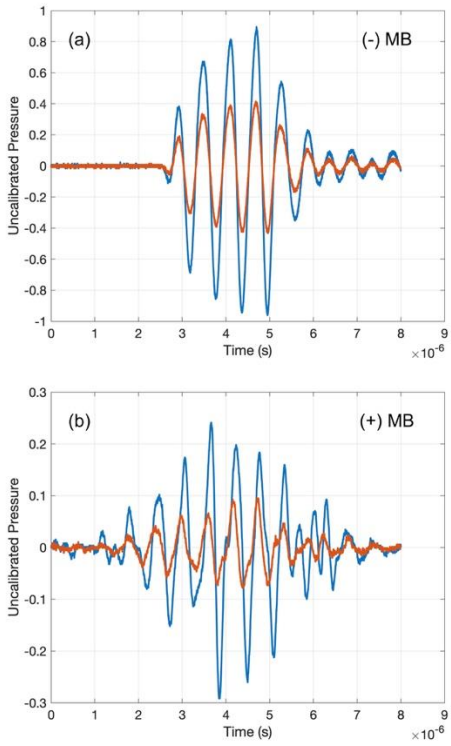

Fig. 3.7: Example scattered echoes from *in vitro* experiments.

Example scattered echoes from (a) a metal reflector, and (b) SonoVue excited at 200 MPa (blue) and 100 MPa (orange). The echoes from the linear reflector were linear and without a visible phase difference $\Delta\Phi_{AM}$, while the echoes from SonoVue were nonlinear and with a visible $\Delta\Phi_{AM}$ (the zero crossings and the peaks and nulls did not align).

The average $\Delta\Phi_{AM}$ across all 20 trials can be seen in **Fig. 3.8**. The $\Delta\Phi_{AM}$ from all microbubble formulations was negative, consistent with the theoretical results. There was no obvious $\Delta\Phi_{AM}$ resulting from scattering off the linear reflector, although a very slight decline in $\Delta\Phi_{AM}$ at high pressures may be observed. In general, Sonazoid and Optison generated $\Delta\Phi_{AM}$ that decreased with increasing pressure, and SonoVue generated $\Delta\Phi_{AM}$ that remained relatively constant. However, due to the inherent variability of scattering, the standard deviations were quite large, obfuscating clear trends between formulations and pressures.

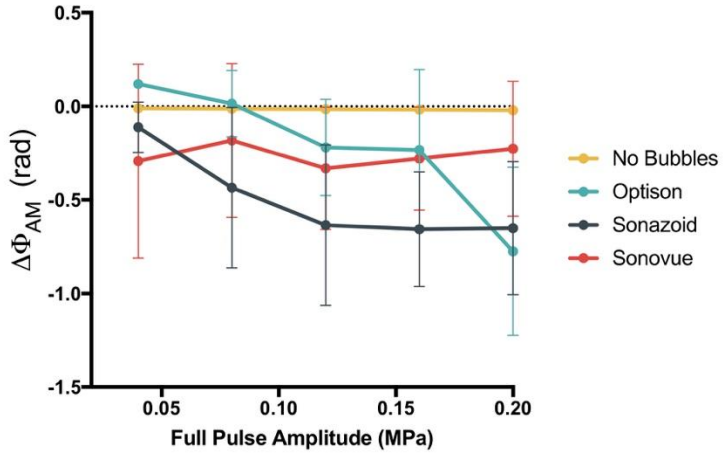

Fig. 3.8: $\Delta\Phi_{AM}$ results from scattering experiments.

All microbubble types produced a negative $\Delta\Phi_{AM}$, while linear echoes from a metal tube did not produce obvious $\Delta\Phi_{AM}$, although a very slight decline may be seen at the highest pressures.

3.4.4 $\Delta\Phi_{AM}$ *from RF data acquisition*

Fig. 3.9 shows the region of interest (ROI) locations analyzed for $\Delta\Phi_{AM}$ in the (a) C5-1 and (b) L12-5, and the resultant $\Delta\Phi_{AM}$ beneath. $\Delta\Phi_{AM}$ for all MIs ranged from -0.1 rad to -0.4 rad for the C5-1 (1.7 MHz transmit frequency) and 0 rad to -0.3 rad for the L12-5 (4.1 MHz transmit frequency). Different microbubble formulations had slightly different $\Delta\Phi_{AM}$ behavior; Sonazoid provided a lower $\Delta\Phi_{AM}$ than SonoVue or Optison at low MI. At high MI, $\Delta\Phi_{AM}$ was similar between all formulations. At the 4.1 MHz frequency, SonoVue, in general, produced the greatest $\Delta\Phi_{AM}$, although Sonazoid provided a similar $\Delta\Phi_{AM}$ when excited with the highest pressure.

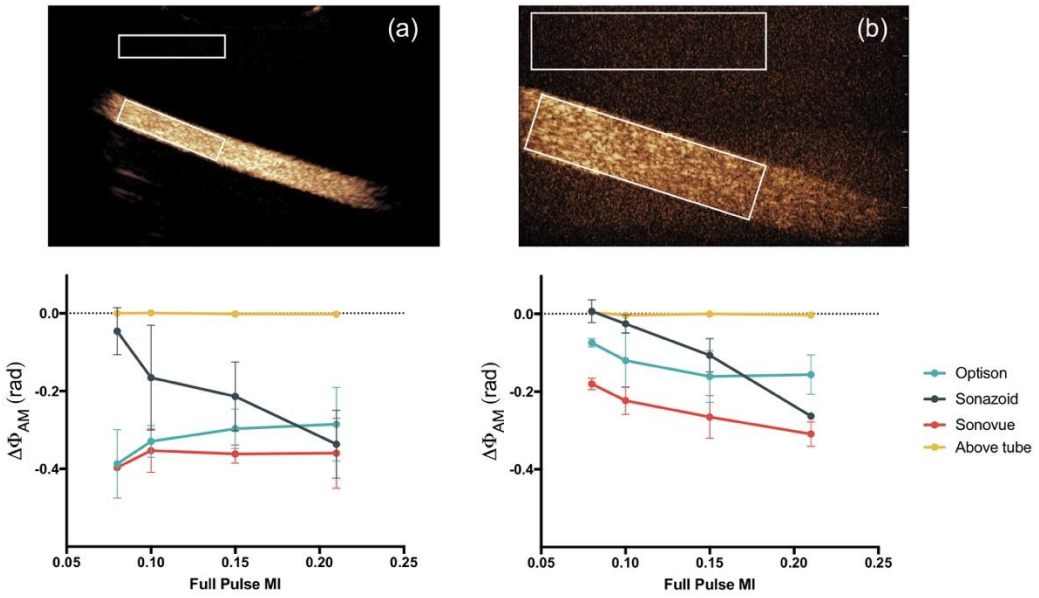

Fig. 3.9: $\Delta\Phi_{AM}$ results from radiofrequency (RF) data.

Data acquisition was performed with a (a) C5-1 curvilinear array and (b) L12-5 array on the Philips iU22 scanner. The top row shows the regions of interest (ROIs) selected for analyzing the phase in the echoes and calculating $\Delta\Phi_{AM}$ for three microbubble formulations. An additional ROI for both the C5-1 and L12-5 above the tube was taken as a tissue control. $\Delta\Phi_{AM}$ results are shown in the bottom row. All microbubble formulations produced a negative $\Delta\Phi_{AM}$, while tissue produced a negligible $\Delta\Phi_{AM}$. Slight differences in $\Delta\Phi_{AM}$ between formulations could be attributed to size and composition.

3.5 DISCUSSION

The goal of this work was to investigate $\Delta\Phi_{AM}$ resulting from both unshelled and shelled microbubble oscillation as well as nonlinear propagation in tissue through both theoretical simulations and *in vitro* experimentation, with the goal of informing optimal parameters for phase segmentation. We observed that both shelled and unshelled microbubbles produced a significant negative $\Delta\Phi_{AM}$, validated with measurements using AM imaging on commercial microbubble formulations in a flow phantom. We also observed that nonlinear propagation resulted in a small degree of $\Delta\Phi_{AM}$, a new finding which could both implicate the reliability of phase segmentation at high mechanical indices as well as open the possibility for phase segmentation during tissue harmonic imaging.

We first evaluated $\Delta\Phi_{AM}$ resulting from unshelled and shelled bubble oscillation during amplitude modulation using the Rayleigh-Plesset and Marmottant Equations, respectively. The most striking result of these simulations was that both shelled and unshelled bubbles produce a distinct negative $\Delta\Phi_{AM}$, dependent on both pressure and bubble size but with differences in overall trends. Unshelled bubbles modeled with the Rayleigh-Plesset Equation provided a $\Delta\Phi_{AM}$ that increased in magnitude with increasing pressure and seemed to be most resonant around 1-2 μm. We also performed the same calculation with the Gilmore equation [15] which accounts for liquid compressibility and violent bubble collapse including shocks and found very similar results. We chose to use the Rayleigh-Plesset equation instead since the Marmottant model is based on it. Shelled bubbles modeled with the Marmottant Equation resulted in waveforms that were more consistent with "compression-only" behavior [27] as seen in **Fig. 3.3**, and different overall $\Delta\Phi_{AM}$ trends. Large, shelled bubbles excited at low pressures resulted in the greatest magnitude of $\Delta\Phi_{AM}$. At smaller radii, $\Delta\Phi_{AM}$ of shelled bubbles was mostly dependent on pressure. We calculated that the resonance size of a free bubble at 1.7 MHz was approximately 1.5 μm and assumed that the resonance size would be larger for shelled bubbles. The $\Delta\Phi_{AM}$ results were consistent with these assumptions as well as with previous results observed by Tremblay-Darveau, et al. [13]. Previously, Tremblay-Darveau attributed the appearance of $\Delta\Phi_{AM}$ solely to shell parameters. The results from our work simulating free gas bubbles suggests that $\Delta\Phi_{AM}$ may have more dependence on nonlinear oscillation of the bubble, whereas the specific trends and resonance characteristics of the $\Delta\Phi_{AM}$ results are impacted by the shell parameters. Due to the strong dependence of $\Delta\Phi_{AM}$ on microbubble radius, phase segmentation could likely be enhanced by using monodisperse microbubbles [28].

The *in vitro* measurements evaluating $\Delta\Phi_{AM}$ with a single element transducer setup first and the ultrasound scanner next confirmed and extended the simulation results. We observed predominantly negative phase differences dependent on microbubble formulation and pressure. Sonazoid produced the greatest magnitude of $\Delta\Phi_{AM}$ at high pressures, while SonoVue and Optison produced greater $\Delta\Phi_{AM}$ at low pressures. This is consistent with the fact that Sonazoid is recommended for use at higher MI [29] than SonoVue and Optison which have lower overall cavitation thresholds [23]. The $\Delta\Phi_{AM}$ trends observed in our measurements were similar between the single element transducer setup and the imaging of a flow phantom with a scanner. Finally, we

saw, in general, a greater $\Delta\Phi_{AM}$ when imaging at lower frequencies. This makes sense, given that microbubbles display resonance behavior dependent on size and frequency [30]. For lower frequency applications such as abdominal imaging this should not be a limitation for using phase segmentation during AM imaging. For clinical applications requiring higher frequencies such as breast or peripheral imaging [31], the generated $\Delta\Phi_{AM}$ from microbubbles is lower and hence the signal segmentation more challenging but still feasible.

Finally, we evaluated $\Delta\Phi_{AM}$ resulting from nonlinear propagation in tissue using the KZK Equation. We found that nonlinear sound propagation from high amplitude transmit pulses results in $|\Delta\Phi_{AM}|$ between 0 and 0.025 rad. The sign and magnitude of $\Delta\Phi_{AM}$ from nonlinear propagation depended on the axial location: pre-focally, the $\Delta\Phi_{AM}$ was mostly positive; at the focus, the $\Delta\Phi_{AM}$ was mostly negative; beyond the focus, the $\Delta\Phi_{AM}$ was again mostly positive. The switching in signs of $\Delta\Phi_{AM}$ around the focus may be a result of a sudden phase shift in Φ_{AM} around the focus as it is shown in Fig. 6 (e). It has been previously reported that tissue produces minimal $\Delta\Phi_{AM}$ [13]. While indeed at a much lower magnitude, our results indicate that nonlinear propagation does in fact result in clear $\Delta\Phi_{AM}$, which has not been evaluated before. That said, microbubble imaging generally takes place at low amplitudes (MI $\leq$ 0.1) [1], in which the $\Delta\Phi_{AM}$ from nonlinear propagation is very small. However, phase variations as a result of microbubble destruction at high amplitudes (4.7 MPa) have been previously reported [32] and utilized as an imaging technique [33], which, according to the results of our simulations, could certainly cause $\Delta\Phi_{AM}$ in tissue. Furthermore, certain microbubble agents, such as Sonazoid, are clinically recommended for use at slightly higher MIs [29] than SonoVue and Optison, at which point $\Delta\Phi_{AM}$ from nonlinear propagation will have a higher value that must be considered for segmentation. Although not evaluated in the present work, the discovery of $\Delta\Phi_{AM}$ arising from nonlinear propagation could open the possibility of performing tissue harmonic imaging using an amplitude modulation scheme with phase segmentation at high MI to distinguish between linear and nonlinear tissue signals.

We acknowledge several limitations to this study. First, we limited our simulation acoustic parameters in order to use standard microbubble imaging parameters modeled off the contrast AM setting on the Philips iU22. Since we were primarily interested in comparison between shelled bubbles, unshelled bubbles, and tissue, we deemed that maintaining a constant imaging parameter

set minimized complexity. Second, we opted to evaluate $\Delta\Phi_{AM}$ at the fundamental frequency, both to be consistent with prior work, and because microbubble signal is strongest at the fundamental. Future efforts could evaluate the use of harmonics or alternate methods of phase analysis, such as cross correlation analysis, to incorporate other frequencies. Finally, although we mention that $\Delta\Phi_{AM}$ could potentially be used in tissue harmonic imaging, we have not yet evaluated this method, but it presents an exciting opportunity for future work

3.6 CONCLUSION

Phase difference between full and half amplitude echoes during amplitude modulation (defined in the present study as $\Delta\Phi_{AM}$) was investigated through simulations of nonlinear oscillation of free and shelled bubbles, nonlinear propagation in tissue, and *in vitro* scattering and AM imaging of commercial microbubbles. We observed that both shelled and unshelled microbubbles resulted in a $\Delta\Phi_{AM}$ with similar overall magnitude with some differences in trends; $\Delta\Phi_{AM}$ from unshelled bubbles was most prominent at large acoustic pressures, while $\Delta\Phi_{AM}$ from shelled bubbles was most prominent at low acoustic pressures and large bubble radii. Regardless, the appearance of $\Delta\Phi_{AM}$ from free bubble simulations, which have not been evaluated for this purpose before, suggest nonlinear oscillation may be a dominant mechanism determining $\Delta\Phi_{AM}$, not shell parameters as previously reported. Simulations of nonlinear propagation in tissue resulted in $\Delta\Phi_{AM}$ of about |0.025| rad, much lower than that of simulated free gas bubbles (up to |1.4| rad), shelled microbubbles (up to |1.8| rad) and experimentally measured commercial microbubbles (up to |1| rad). Although low, the presence of phase difference in tissue has a strong implication on parameter selection for optimal segmentation based on echo phase

3.7 ACKNOWLEDGMENTS

We gratefully acknowledge GE Healthcare for the Sonazoid and Optison used in this study.

3.8 REFERENCES

[1] M. A. Averkiou, M. F. Bruce, J. E. Powers, P. S. Sheeran, and P. N. Burns, *Imaging Methods for Ultrasound Contrast Agents*, vol. 46, no. 3. 2020, pp. 498–517. doi: 10.1016/j.ultrasmedbio.2019.11.004.

[2] S. Sirsi and M. Borden, “Microbubble Compositions, Properties and Biomedical Applications,” *Bubble Sci Eng Technol.*, vol. 1, pp. 3–17, 2010, doi: 10.1179/175889709X446507.Microbubble.
[3] E. Stride, “Physical principles of microbubbles for ultrasound imaging and therapy,” *Cerebrovascular Diseases*, vol. 27, no. SUPPL. 2, pp. 1–13, 2009, doi: 10.1159/000203122.
[4] J. R. Lindner, “Microbubbles in medical imaging: Current applications and future directions,” *Nature Reviews Drug Discovery*, vol. 3, no. 6, pp. 527–532, 2004, doi: 10.1038/nrd1417.
[5] K. Ferrara, R. Pollard, and M. Borden, “Ultrasound Microbubble Contrast Agents: Fundamentals and Application to Gene and Drug Delivery,” *Annu. Rev. Biomed. Eng*, vol. 9, pp. 415–47, 2007, doi: 10.1146/annurev.bioeng.8.061505.095852.
[6] R. J. Eckersley, C. T. Chin, and P. N. Burns, “Optimising phase and amplitude modulation schemes for imaging microbubble contrast agents at low acoustic power.,” *Ultrasound in medicine & biology*, vol. 31, no. 2, pp. 213–9, Feb. 2005, doi: 10.1016/j.ultrasmedbio.2004.10.004.
[7] T.-Y. Lai and M. A. Averkiou, “Linear Signal Cancellation of Nonlinear Pulsing Schemes in a Verasonics Research Scanner,” *IEEE Transactions on Ultrasonics, Ferroelectrics, and Frequency Control*, vol. 68, no. 5, pp. 1721–1728, May 2021, doi: 10.1109/TUFFC.2021.3050481.
[8] T.-Y. Lai and M. A. Averkiou, “Linear Signal Cancellation of Nonlinear Pulsing Schemes in a Verasonics Research Scanner,” *IEEE Transactions on Ultrasonics, Ferroelectrics, and Frequency Control*, vol. 68, no. 5, pp. 1721–1728, May 2021, doi: 10.1109/TUFFC.2021.3050481.
[9] O. Couture, M. Fink, and M. Tanter, “Ultrasound contrast plane wave imaging.,” *IEEE transactions on ultrasonics, ferroelectrics, and frequency control*, vol. 59, no. 12, pp. 2676–83, Dec. 2012, doi: 10.1109/TUFFC.2012.2508.
[10] M. F. Hamilton and D. T. Blackstock, *Nonlinear acoustics*. Academic press San Diego, 1998.
[11] P.-C. Li, C.-C. Shen, and S.-W. Huang, “Waveform design for ultrasonic pulse-inversion fundamental imaging.,” *Ultrasonic imaging*, vol. 28, no. 3, pp. 129–43, Jul. 2006, doi: 10.1177/016173460602800301.
[12] P. J. Phillips, “Contrast pulse sequences (CPS): imaging nonlinear microbubbles,” in *2001 IEEE Ultrasonics Symposium. Proceedings. An International Symposium (Cat. No.01CH37263)*, vol. 2, pp. 1739–1745. doi: 10.1109/ULTSYM.2001.992057.
[13] C. Tremblay-Darveau *et al.*, “The Role of Microbubble Echo Phase Lag in Multipulse Contrast-Enhanced Ultrasound Imaging,” *IEEE Transactions on Ultrasonics, Ferroelectrics, and Frequency Control*, vol. 65, no. 8, pp. 1389–1401, Aug. 2018, doi: 10.1109/TUFFC.2018.2841848.
[14] P. Marmottant *et al.*, “A model for large amplitude oscillations of coated bubbles accounting for buckling and rupture,” *The Journal of the Acoustical Society of America*, vol. 118, no. 6, pp. 3499–3505, Dec. 2005, doi: 10.1121/1.2109427.
[15] T. G. Leighton, *The acoustic bubble*. Academic Press, 1994.
[16] V. Kuznetsov, “Equations of nonlinear acoustics,” *Soviet Physics Acoustics*, vol. 16, pp. 467–470, 1971.

[17] E. Zabolotskaya, “Quasi-plane waves, in the nonlinear acoustics of confined beams,” *Soviet Physics Acoustics*, vol. 15, pp. 35–40, 1969.
[18] W. Lauterborn, “Numerical investigation of nonlinear oscillations of gas bubbles in liquids,” *Journal of the Acoustical Society of America*, vol. 59, no. 2, pp. 283–293, Aug. 1976, doi: 10.1121/1.380884.
[19] M. A. Averkiou, Y. Lee, and M. F. Hamilton, “Self-demodulation of amplitude- and frequency-modulated pulses in a thermoviscous fluid,” *The Journal of the Acoustical Society of America*, vol. 94, no. 5, pp. 2876–2883, Nov. 1993, doi: 10.1121/1.407344.
[20] M. A. Averkiou and M. F. Hamilton, “Measurements of harmonic generation in a focused finite-amplitude sound beam.,” *The Journal of the Acoustical Society of America*, vol. 98, no. 6, pp. 3439–42, Dec. 1995, doi: 10.1121/1.413795.
[21] T.-Y. Lai, M. Bruce, and M. A. Averkiou, “Modeling of the Acoustic Field Produced by Diagnostic Ultrasound Arrays in Plane and Diverging Wave Modes.,” *IEEE transactions on ultrasonics, ferroelectrics, and frequency control*, vol. 66, no. 7, pp. 1158–1169, 2019, doi: 10.1109/TUFFC.2019.2908831.
[22] M. A. Averkiou and M. F. Hamilton, “Nonlinear distortion of short pulses radiated by plane and focused circular pistons,” *The Journal of the Acoustical Society of America*, vol. 102, no. 5, p. 2539, Jun. 1998, doi: 10.1121/1.420308.
[23] S. B. Keller, P. S. Sheeran, and M. A. Averkiou, “Cavitation Therapy Monitoring of Commercial Microbubbles With a Clinical Scanner,” *IEEE Transactions on Ultrasonics, Ferroelectrics, and Frequency Control*, vol. 68, no. 4, pp. 1144–1154, Apr. 2021, doi: 10.1109/TUFFC.2020.3034532.
[24] M. Minnaert, “On musical air-bubbles and the sounds of running water,” *Philos. Mag.*, vol. 16, pp. 235–248, Aug. 1933, doi: 10.1080/14786443309462277.
[25] M. Versluis, E. Stride, G. Lajoinie, B. Dollet, and T. Segers, “Ultrasound Contrast Agent Modeling: A Review,” *Ultrasound in Medicine & Biology*, vol. 46, no. 9, pp. 2117–2144, Sep. 2020, doi: 10.1016/J.ULTRASMEDBIO.2020.04.014.
[26] A. A. Doinikov, J. F. Haac, and P. A. Dayton, “Resonance frequencies of lipid-shelled microbubbles in the regime of nonlinear oscillations,” *Ultrasonics*, vol. 49, no. 2, p. 263, Feb. 2009, doi: 10.1016/J.ULTRAS.2008.09.006.
[27] N. de Jong *et al.*, “‘Compression-Only’ Behavior of Phospholipid-Coated Contrast Bubbles,” *Ultrasound in Medicine and Biology*, vol. 33, no. 4, pp. 653–656, Apr. 2007, doi: 10.1016/j.ultrasmedbio.2006.09.016.
[28] T. Segers, P. Kruizinga, M. P. Kok, G. Lajoinie, N. de Jong, and M. Versluis, “Monodisperse Versus Polydisperse Ultrasound Contrast Agents: Non-Linear Response, Sensitivity, and Deep Tissue Imaging Potential,” *Ultrasound in Medicine & Biology*, vol. 44, no. 7, pp. 1482–1492, Jul. 2018, doi: 10.1016/J.ULTRASMEDBIO.2018.03.019.
[29] J. Y. Jang *et al.*, “Current consensus and guidelines of contrast enhanced ultrasound for the characterization of focal liver lesions,” *Clinical and Molecular Hepatology*, vol. 19, no. 1, p. 1, 2013, doi: 10.3350/cmh.2013.19.1.1.
[30] A. A. Doinikov, J. F. Haac, and P. A. Dayton, “Resonance frequencies of lipid-shelled microbubbles in the regime of nonlinear oscillations.,” *Ultrasonics*, vol. 49, no. 2, pp. 263–8, Feb. 2009, doi: 10.1016/j.ultras.2008.09.006.
[31] M. Bruce *et al.*, “High-Frequency Nonlinear Doppler Contrast-Enhanced Ultrasound Imaging of Blood Flow,” *IEEE Transactions on Ultrasonics, Ferroelectrics, and*

Frequency Control, vol. 67, no. 9, pp. 1776–1784, Sep. 2020, doi: 10.1109/TUFFC.2020.2986486.
[32] J. E. Chômas, P. Dayton, J. Alien, K. Morgan, and K. W. Ferrara, "Mechanisms of contrast agent destruction," *IEEE Transactions on Ultrasonics, Ferroelectrics, and Frequency Control*, vol. 48, no. 1, pp. 232–248, Jan. 2001, doi: 10.1109/58.896136.
[33] M. Siepmann *et al.*, "Phase shift variance imaging-a new technique for destructive microbubble imaging," *IEEE Transactions on Ultrasonics, Ferroelectrics, and Frequency Control*, vol. 60, no. 5, pp. 909–923, 2013, doi: 10.1109/TUFFC.2013.2648.

Chapter 4. ULTRASOUND IMAGING OF MICROBUBBLE ACTIVITY DURING SONOPORATION PULSE SEQUENCES[3]

Sara B. Keller, Matt Bruce, Michalakis A. Averkiou

Abstract

Ultrasound-mediated drug delivery using the mechanical action of oscillating and/or collapsing microbubbles has been studied in many different experimental platforms, both *in vitro* and *in vivo*; however, the mechanisms remain to be elucidated. Many groups use sterile, enclosed chambers, such as Opticells or Clinicells, to optimize acoustic parameters *in vitro* needed for effective drug delivery *in vivo*, as well as for mechanistic investigation of sonoporation, or the use to sound to permeate cell membranes. In these containers, cell monolayers are seeded on one side and the rest of the volume is filled with a solution containing microbubbles and a model drug. Ultrasound is then applied to study the effect of different parameters on model drug uptake in cell monolayers. Despite the simplicity of this system, the field has been unable to appropriately address what parameters and microbubble concentrations are most effective at enhancing drug uptake and minimizing cellular toxicity. In this work, a common *in vitro* sonoporation experimental setup was characterized through quantitative analysis of microbubble-dependent acoustic attenuation in combination with high frame rate and high resolution imaging of bubble activity during sonoporation pulse sequences. The goal was to visualize the effect that ultrasound parameters have on microbubble activity. It was observed that under literature-derived sonoporation conditions (0.1 to 1 MPa, 20 to 1000 cycles, and 10k to 10M microbubbles per mL), there is strong and nonlinear acoustic attenuation, as well as bubble destruction, gas diffusion, and bubble motion resulting in spatiotemporal pressure and concentration gradients. Ultimately, it was shown that the acoustic conditions in common *in vitro* sonoporation setups are much more complex and confounding than often assumed.

[3] *Reprinted with permission from Keller, SB, et al. "Ultrasound Imaging of Microbubble Activity During Sonoporation Pulse Sequences." Ultrasound Med. Biol.,* ***45****, 833-845 (2019).*

4.1 INTRODUCTION

Beyond diagnostic imaging, contrast-enhanced ultrasound has shown immense promise in the field of drug delivery [1], [2]. With the growing clinical relevancy of delivering macromolecular therapeutics, including proteins [3] and nucleic acids [4], ultrasound and microbubbles can provide a means for overcoming traditional barriers defining intracellular drug uptake [5]. In the presence of an acoustic wave, microbubbles undergo volumetric oscillations and eventual destruction, which can provide both an acoustic signal for contrast enhancement through resonant scattering as well as localized microscale forces that can cause increased cell membrane permeation through a process known as sonoporation [6].

However, despite over 10 years of promising studies both *in vitro* [7], [8] and *in vivo* [9], [10], the acoustic parameters that lead to effective sonoporation remain ambiguous. Peak negative pressure, pulse length, frequency, pulse repetition frequency, and microbubble concentration are all important parameters that have been studied, yet there is not conclusive agreement for these parameters between different studies. It has been generally accepted that increasing acoustic pressure may increase sonoporation efficiency, but at the expense of cell viability [11], [12]. Additionally, several groups suggest that microbubble-cell distance can also affect the success of particle uptake [13], while others suggest that rather it is microbubble displacement that governs membrane poration [12], [14]. The choice of whether to send a single pulse [12] or a series of repeated pulses [7] can add an additional layer of complexity. The resultant ambiguity in parameter space can obfuscate understanding of biophysical mechanism. We hypothesize that an additional confounding factor *in vitro* is due to the lack of standardization in experimental setup and macroscale field effects. While several papers mention microbubble oscillation and displacement as a means of inducing sonoporation, they are limited by optical microscopy, which, despite having high spatiotemporal resolution in one plane, does not consider the 3D geometry of microbubble movement or overall acoustic environment [12], [14]. To the best of our knowledge, there have been no existing studies on how microbubble presence affects sound propagation in a 3D volume during the sonoporation process.

Moreover, there are three distinct timescales important in sonoporation: 1) the time of bubble oscillation, equal to the duration of the sound pulse (microseconds), 2) the timescale of bubble destruction (accompanied by gas diffusion) and radiation force (milliseconds), and 3) the timescale of cell membrane permeation (seconds to minutes). For the first timeframe, super high frame rate microscopy with a Brandaris camera has been used [12], [15], and for the third, *in vitro* studies of propidium iodide uptake into cells and membrane resealing mechanics have been performed [11], [16]. We concentrate on the second timescale and hypothesize that examining the temporal window after application of an ultrasound pulse may further elucidate this process.

The objective of this work was to evaluate the effect of various acoustic parameters and microbubble concentrations on the resulting microbubble activity during sonoporation in cell enclosures. To this end, we have performed quantitative representations of microbubble concentrations in a 3D volume, acoustic attenuation measurements through increasing microbubble concentrations, and high-resolution and ultrafast ultrasound imaging of bubble behavior during and after ultrasound exposures. We evaluated conditions similar to those found in the literature: moderate pressures (125 kPa-1 MPa), cycles (20-1000), and concentrations (10k – 10M MBs/mL) using both single pulses and repeated pulses with a single element focused 1 MHz transducer. Studying microbubble behavior in a tightly controlled experimental design may help explain the conflicting results in published literature and may lead to reproducible sonoporation.

4.2 Materials and Methods

4.2.1 *Microbubble Preparation*

Microbubbles composed of DPPC (1,2-dipalmitoyl-sn-glycero-3-phosphocholine) and DSPE-PEG (1,2-distearoyl-sn-glycero-3-phosphoethanolamine-N-[methoxy(polyethylene glycol)-2000]) (Avanti Polar Lipids Inc, Alabaster, AL) in a 95:5 molar ratio were prepared as described previously [7] and used for imaging studies to mimic prior Opticell sonoporation work [7], [11], [12]. SonoVue (Bracco Suisse SA, Geneva, Switzerland) was additionally used in attenuation studies for comparison with a clinically relevant microbubble. Average bubble diameter by volume was measured using a Multisizer 3 (Beckman Coulter, Brea, CA) and determined to be approximately 3 μm for the custom formulation and 4.5 μm for SonoVue. To understand how

microbubble concentration in a 3D volume impacts bubble-to-cell ratio, theoretical calculations were made to estimate the effective concentration that appears next to cells. A Clinicell (MABIO, Tourcoing, France) was chosen as the representative cell enclosure, and has dimensions of 0.5 cm x 6.2 cm x 3.8 cm (**Fig. 4.1**). The average distance between microbubbles (d_{avg}) was calculated as shown in **Equation 4.1**, where V is the volume of the container (m^3) and N_{MB} is the total number of microbubbles in the container.

$$d_{avg} = \sqrt[3]{\frac{V}{N_{MB}}} \qquad (4.1)$$

Distance between microbubbles was tracked at varying concentrations (10k to 100M microbubbles/mL). Shown in **Fig. 4.1** are the assumptions made in determining this metric, where 3 μm x 3 μm cubes represent microbubbles, an approximation given the 3 μm diameter custom microbubble. This was compared against the standard length of endothelial cells (15 μm). Void fraction (ϕ), or the fraction of the solution that exists in the gas phase (microbubbles) versus the liquid phase (solvent) was also calculated at increasing concentrations as shown in **Equation 4.2** as a secondary measure of microbubble dispersity, where V_{MB} is the volume of a single microbubble (m^3), N_{MB} is the total number of microbubbles in the container, and V is the total volume of the container (m^3).

$$\phi = \frac{V_{MB} \times N_{MB}}{V} \qquad (4.2)$$

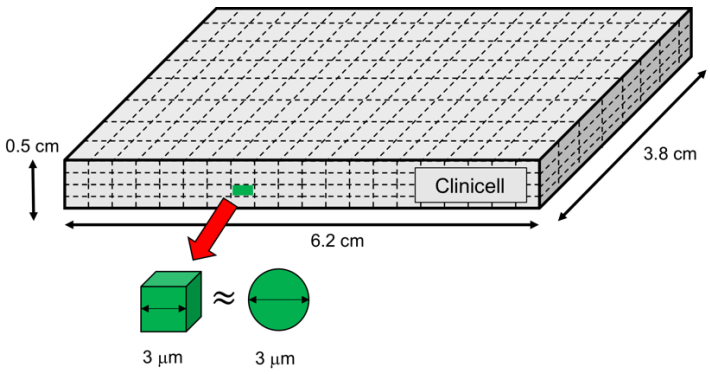

Fig. 4.1: Model of concentration and dispersity of microbubbles in a 3D volume.

Each grid (not to scale) represents a microbubble, which are approximated to be 3 μm cubes, as measured with a Multisizer 3.

4.2.2 *Acoustic Attenuation*

All experiments were conducted using a custom-made single element focused transducer (diameter = 20 mm, focal distance = 80 mm, frequency = 1 MHz). 20 cycle sound pulses were sent using a Tektronix AFG 3102 Arbitrary Waveform Generator (Tektronix, Inc., Beaverton, OR), amplified by an ENI 2200L RF Amplifier (ENI, Rochester, NY), and transmitted by the focused transducer. Transmit pressure, defined here as peak negative pressure, was scaled up 10% per pressure reduction through the Clinicell when measured relative to the free-field. Transmit parameters can be seen in **Table 4.1**. The sound pressure of a pulse transmitted by the 1 MHz transducer reaching a 0.4 mm membrane hydrophone (Precision Acoustics Ltd., Dorchester, UK) after passage through a Clinicell filled with increasing concentrations of microbubbles was measured. Microbubble concentration was measured using the Multisizer 3. The Clinicell was placed 4 cm away from the focused transducer, as beam characterization measurements showed that this distance had the largest pressure amplitude. The hydrophone was placed 2 cm away from the enclosure to measure the acoustic pressure after transmission through the Clinicell upon exiting. The cell enclosure was placed in the vertical orientation for this experiment, as shown in **Fig. 4.2a**, to avoid the effects of sound reflection at the water-air interface. Bubble rising effects due to buoyancy were minimized by quick measurement and refilling each time and were not seen in imaging. The signals were acquired using a DPO7054C Oscilloscope (Tektronix, Inc., Beaverton, OR) and analyzed in MATLAB (The MathWorks, Inc., Natick, MA, USA). Received peak negative pressure was measured for each microbubble concentration.

Table 4.1: Overview of acoustic parameters used for sonoporation imaging.

	Pressure (kPa)	**Cycles**	**PRF**	**Concentration (microbubbles/mL)**
Attenuation	125, 250, 500	20	Single Pulse	10k - 10M
High-Resolution Imaging	200, 500, 1000	20, 200	1 Hz, 51 Hz	500k, 5M
High FR Imaging	1000	20, 200, 1000	Single Pulse	500k, 5M

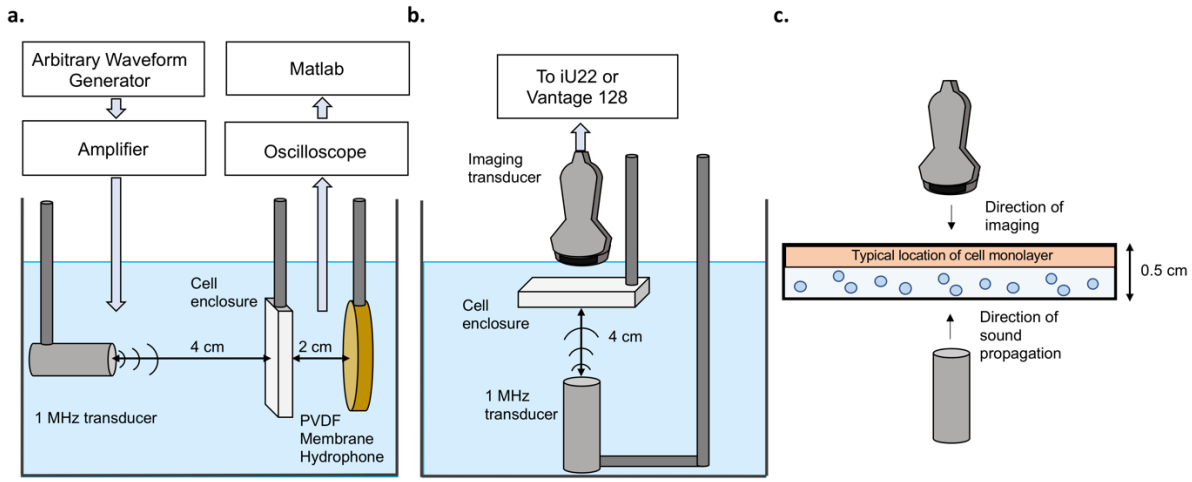

Fig. 4.2: Setup orientations of attenuation and imaging experiments.

(a) is the vertical orientation used for acoustic attenuation. (b) is the horizontal orientation used for microbubble imaging. (c) represents where cells would be located in reference to therapy and imaging transducers.

4.2.3 *High-Resolution Imaging of the Sonoporation Process*

A Philips iU22 (Philips Medical Systems, Bothell, WA) was used to visualize the bubble activity, destruction, and movement induced by the 1 MHz transducer. An L15-7io probe operating at 12 MHz, provided high-resolution at a moderately high frame rate of 51 Hz B-mode fundamental imaging. The imaging mechanical index (MI) was set to 0.05 to avoid bubble destruction. The imaging system inherently applies a time gain compensation, which was set to the default value for tissue. The same transmit setup was used as in the attenuation studies, except that the Clinicell was placed in the horizontal orientation, seen in **Fig. 4.2b**. This position was chosen to accommodate imaging. Exposures were performed immediately after introduction in the tank environment to limit bubble rising. Images were acquired while the 1 MHz transducer was firing at 1 Hz or 51 Hz PRF. Since the experiments were in water and there were no other ultrasound scatterers in the medium, it was adequate to use fundamental B-mode imaging as opposed to contrast-specific imaging modes for visualizing microbubbles. Images loops were analyzed in QLAB (Philips Medical Systems, Bothell, WA). For the 1 Hz PRF condition, images were acquired in real-time (51 Hz in this case) after multiple exposures from the focused transducer. For the 51 Hz PRF condition, images were acquired over a five second exposure. The conditions

tested can be seen in **Table 4.1**, and were chosen to represent parameters used in published *in vitro* sonoporation studies.

4.2.4 *High Frame Rate Imaging of the Sonoporation Process*

High frame rate imaging was performed with a Vantage 128 (Verasonics, Kirkland, WA) system in order to image and resolve the bubble activity during and after ultrasound excitation with a single element 1 MHz transducer. A linear array operating at 15 MHz (Vermon, France) was used for imaging. The transmitted imaging pulse was 2 cycles long and the MI was 0.05 to avoid bubble destruction. 8000 frames at an 8 kHz frame rate were captured while imaging in the orientation shown in **Fig. 4.2b**. A single pulse at 1 MPa and with duration 20, 200, or 1000 cycles was fired by the single element 1 MHz transducer. One second image loops were collected with the imaging system to study bubble destruction and gas diffusion at this greatly improved temporal resolution (compared to conventional scanners).

4.3 RESULTS

4.3.1 *Microbubble Concentration Measurements*

Average distance between microbubbles and void fraction at increasing microbubble concentrations can be seen in **Fig. 4.3**. Distance between microbubbles decreases with increasing concentration (a), while void fraction increases (b). Even at the highest concentrations used (10 million microbubbles/mL), the distance between microbubbles is still only about 50 μm. Void fraction remains quite low (10^{-7} – 10^{-4}), indicating that despite the high microbubble concentrations, still the actual microbubble volume is minimal. Also shown in (c) are the pictorial representations of how these microbubble concentrations may manifest near cell monolayers. Concentrations used in prior works range from 100,000 microbubbles/mL to 10 million microbubbles/mL [12], [17]. However, only when the microbubble concentration reaches 100 million microbubbles/mL, a concentration much greater than what was used in the above publications, does the “bubble-to-cell” ratio near cells reach 1:1.

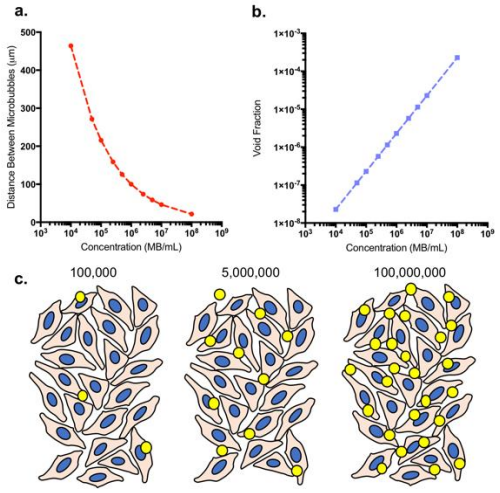

Fig. 4.3: Representation of bubble-to-cell ratio.

(a) distance between microbubbles, measured using Equation 1 and (b) void fraction, measured using Equation 2. (c) shows the visualization of these microbubble concentrations in comparison with 15 µm diameter endothelial cells.

4.3.2 *Acoustic Attenuation*

Despite low void fractions, with increasing concentration of microbubbles, the attenuation increases and the resultant signal decreases (**Fig. 4.4**). **Fig. 4.4a** shows the propagated peak negative pressure for the custom microbubble formulation and **Fig. 4.4b** for SonoVue. For both formulations, higher pressure pulses experienced more attenuation. When using the custom microbubbles at a concentration of 1,000,000 microbubbles/mL, the pressure received after transmitting with 500 kPa had already decreased by over 50%, while it had only decreased about 20% when transmitting with 125 kPa. SonoVue experienced slightly more attenuation than the custom formulation; however, the overall trends seen with the custom formulation and SonoVue remain mostly consistent.

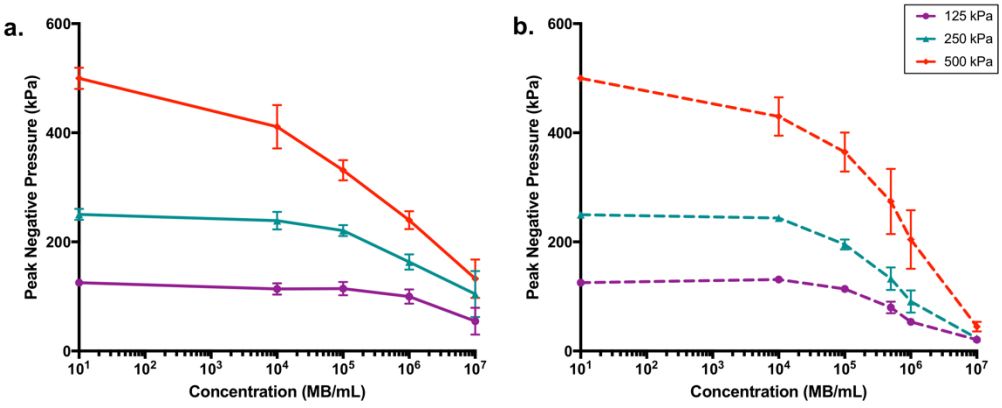

Fig. 4.4: Microbubble attenuation versus concentration.

The transmit pressures used are 125, 250, and 500 kPa (peak negative pressure). Shown in (a) are the received peak negative pressure amplitudes of pulses through a volume of custom microbubbles after a single transmit pulse and shown in (b) are the peak negative pressure amplitudes through a volume of SonoVue microbubbles after a single transmit pulse.

4.3.3 *High-Resolution Imaging of the Sonoporation Process*

Shown in **Fig. 4.5** and **Fig. 4.6** are images acquired with a Philips iU22 of bubbles in the Clinicell during sonoporation-type excitations from a 1 MHz transducer. **Fig. 4.5** shows the effect of repeated 20 cycle pulses, while **Fig. 4.6** shows the effect of repeated 200 cycle pulses. The effect of changing other parameters (pressure, concentration, and PRF) is also shown in both figures.

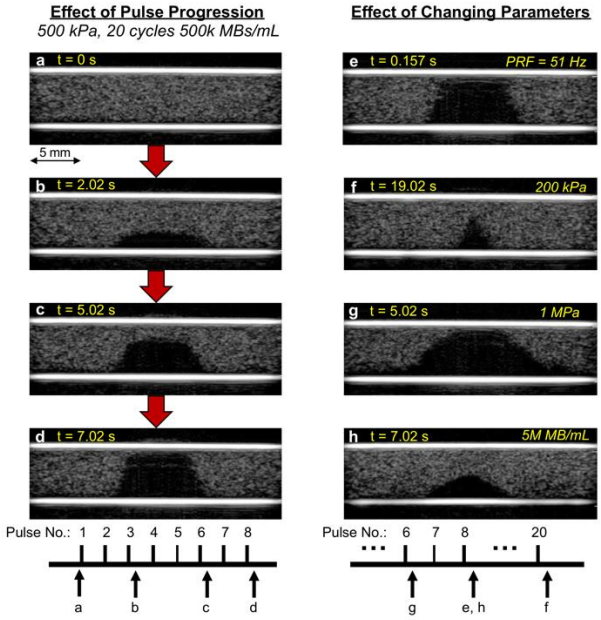

Fig. 4.5: Representative images of 20 cycle pulse excitations with varied parameters.

(a-d) show the effect of sending 500 kPa pulses through 500k MBs/mL at a repetition frequency of 1 Hz. The first pulse was sent at time t = 0s, the second pulse at t =1s, and so forth. Images were acquired the frame immediately after the pulse was sent except for (a) which was acquired immediately before the pulse. It takes 8 pulses for complete bubble elimination through the Clinicell. (e-h) show the effect of changing different parameters, specifically, (e) increasing PRF, (f) decreasing pressure, (g) increasing pressure, and (h) increasing concentration. Increasing PRF only changes the rate of bubble elimination (seen in [e] versus [d]), decreasing or increasing pressure causes a decrease or increase in bubble elimination accordingly, and increasing concentration reduces bubble elimination.

Fig. 4.5(a-d) shows the images recorded after multiple firings from a 20 cycle, 500 kPa pulse at a 1 Hz PRF (i.e., 1 s between firings) through 500,000 microbubbles/mL. This PRF was chosen to analyze bubble activity after repeated single exposures at a slow rate (1 Hz) while acquiring images at a much higher rate (51 Hz). The first pulse was sent at time t = 0s (**Fig. 4.5a**), the second pulse at t =1s, and so forth. As more pulses are sent, progressing from **Fig. 4.5a** to **d**, the amount of bubble elimination, defined here as the combination of bubble destruction and bubble motion, is increased. However, the amount of motion seen was minimal, implying that most bubble elimination that occurs using 20 cycle pulses is due to bubble destruction alone. Complete bubble elimination through the entire volume of the propagation path did not occur using this setting until 8 pulses had been sent (**Fig. 4.5d**).

Fig. 4.5e examines the effect of increasing the sonication PRF (not to be confused with the imaging frame rate) to 51 Hz, as pulse repetition has been considered in various published works [7], [14]. After 8 pulses were sent at 51 Hz (in 157 ms), the resultant image looks nearly the same as after 8 pulses sent at 1 Hz (in 7 s) (**Fig. 4.5d**), implying that when using this pulsing scheme, the only change is the rate of bubble elimination. **Fig. 4.5f** and **g** show the impact of changing sonication acoustic pressure. When a 200 kPa pulse was used (**Fig. 4.5f**), there was much less bubble elimination than when 500 kPa was used, even after 20 repeated pulses. Conversely, when a 1 MPa pulse was sent (**Fig. 4.5g**), there was much more bubble elimination. The width of bubble elimination also increased with increasing pressure. This is because at higher pressures a larger portion of the beam is above the bubble destruction threshold. **Fig. 4.5h** shows the effect of increasing microbubble concentration. At this higher concentration, the bubble elimination that reaches the top of the Clinicell due to the 1 MHz firings is reduced.

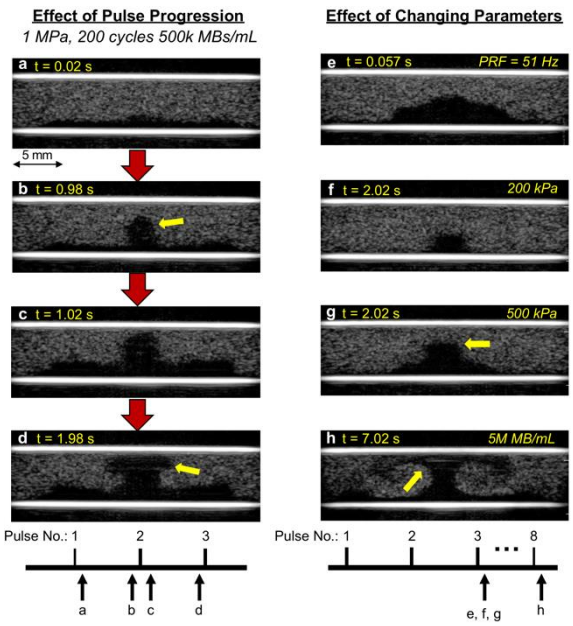

Fig. 4.6: Representative images of 200 cycle pulse excitations with varied parameters.

(a-d) show the effect of sending 1 MPa pulses through 500k MBs/mL at a repetition frequency of 1 Hz. The first pulse was sent at time t = 0s. (a) and (c) were the frames acquired immediately after the 1st and 2nd pulses, respectively, and show their immediate effect, while (b) and (d) show the evolution of movement resulting from these pulses. Yellow arrows indicate areas where movement had occurred. (e-h) show the effect of changing different parameters, specifically, (e) increasing PRF, (f,g) decreasing pressure, and (h) increasing concentration. Increasing PRF reduces bubble elimination due to movement (seen in [e] versus [d]), decreasing pressure decreases bubble elimination, and increasing concentration reduces bubble elimination and causes swirling to occur.

Fig. 4.6(a-d) shows the images recorded after multiple firings from a 200 cycle, 1 MPa pulse at a 1 Hz PRF through 500,000 microbubbles/mL. **Fig. 4.6a** and **c** show the images acquired immediately after the end of the 1st and 2nd transmit pulses, respectively. **Fig. 4.6b** and **d** show the evolution of movement that occurred subsequent to these transmit pulses. While the initial pulse caused a small degree of bubble destruction, the time between pulse excitations allowed for visualization of resultant bubble motion, shown with yellow arrows. Indeed, the bubble elimination that eventually reaches the upper membrane of the Clinicell is a result of this movement, and not just destruction, as demonstrated in **Fig. 4.6d**.

Fig. 4.6e shows the effect of using a 51 Hz sonication PRF. Unlike when using 20 cycles, increasing the pulse repetition rate had a significant impact on the bubble elimination profile. Specifically, the short time between repeated pulses reduced the amount of movement that could

occur prior to the next pulse. Therefore, the unique movement patterns seen using a 1 Hz PRF and long cycles were not seen when using a higher PRF. **Fig. 4.6f** and **g** show the effect of using two lower pressures. Bubble elimination that occurs from these two transmit sequences is smaller than the 1 MPa transmit pulse, but motion still occurs, as indicated with yellow arrows. Finally, increasing the concentration increased the complex motion shown in **Fig. 4.6d**. Pulses sent through a high concentration of microbubbles resulted in bubble swirling surrounding the direction of axial propagation (**Fig. 4.6h**).

In summary, increasing the number of cycles in the pulse increased the amount of bubble motion that occurred after the end of the transmit pulse. Increasing acoustic pressure increased the area of bubble elimination, both in the lateral and axial direction. Higher concentrations reduced the bubble elimination that reached the top of the Clinicell. Finally, using a higher pulse repetition frequency only changed the bubble elimination profile when movement was occurring.

4.3.4 *High Frame Rate Imaging of the Sonoporation Process*

High frame rate imaging using a Verasonics 128 was used to show the effect of a single 1 MPa pulse at high temporal resolution not possible with conventional ultrasound. Similar to the experiments using the Philips iU22, the results from high frame rate imaging can be broken into the individual variable effects of cycles and concentration. The two columns in **Fig. 4.7**, **(a-d)** and **(e-h)** show progressions from two different single pulses through different bubble concentrations. The time scale starts when the pulse is fired. Therefore, for the 200 cycle condition, the sonoporation pulse duration is 2 imaging frames, and for the 1000 cycle condition, the pulse duration is 8 frames.

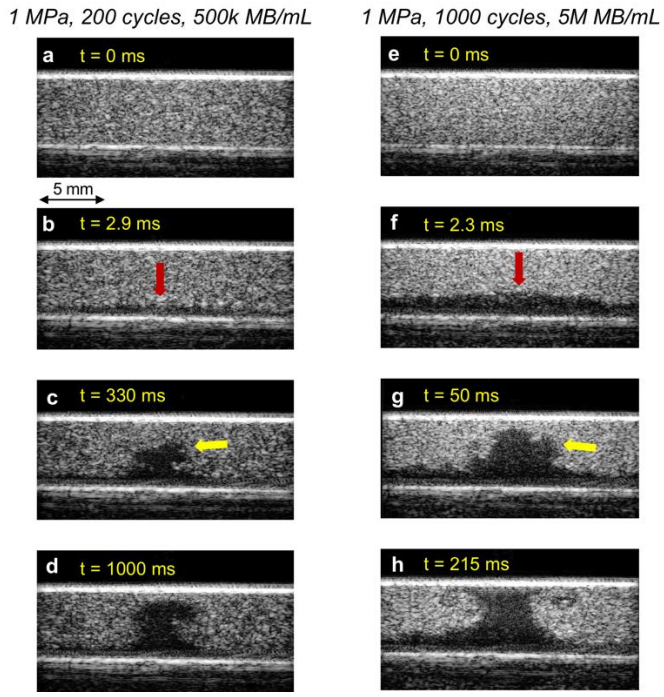

Fig. 4.7: High frame rate images of single pulse excitation.

Images during high frame rate acquisitions with a Verasonics 128 of microbubble activity caused with a single pulse excitation. The time t = 0 denotes the firing of the pulse. (a-e) show the effect of a 1 MPa, 200 cycle pulse through 500k MBs/mL, and (e-h) show the effect of a 1 MPa, 1000 cycle pulse through 5M MBs/mL. For each condition, the red arrows represent the extent of initial bubble destruction immediately following the end of the ultrasound pulse, while the yellow arrows represent the subsequent microbubble behavior independent of bubble oscillation. These images show the delineation between immediate bubble destruction and subsequent bubble movement.

Fig. 4.7 (a-d) shows the progression of a 1 MPa, 200 cycle pulse through a Clinicell filled with 500,000 microbubbles/mL. Shown in **Fig. 4.7b** is the frame taken 2.9 ms after the pulse begins. The bubble elimination shown with a red arrow is theorized to be due to bubble destruction from the high-pressure excitation as it is present immediately after the pulse ends. The void areas shown in **Fig. 4.7c** and **d** that occur after the initial bubble destruction are theorized to be due to bubble movement from acoustic streaming and gas diffusion.

Fig. 4.7 (e-h) shows the progression of a 1 MPa pulse with an increased number of cycles through a higher microbubble concentration. **Fig. 4.7f**, a frame taken shortly after the end of the pulse, shows that there is considerably more initial bubble destruction than in the 200 cycle pulse condition. Similarly, as shown in subsequent frames, there is more dramatic movement that occurs,

highlighted with the yellow arrow in **Fig. 4.7g**. Finally, as in **Fig. 4.6h** where a high microbubble concentration was also used, a similar swirling pattern develops in **Fig. 4.7h**.

Fig. 4.8 shows the effect of a 20 cycle pulse through 500,000 microbubbles/mL. In **Fig. 4.8a**, the image taken 2.5 ms after the pulse was fired, there was no amount of initial bubble elimination at these ultrasound settings; however, after 100 ms, a sizable void area has developed (**Fig. 4.8b**) without observing any type of bubble motion in the images that preceded. This is reasoned to be due to gas diffusion after bubble shell disruption, known to occur within durations on the order of 100 ms after the collapse of a gas volume of this size [18]. No bubble movement was seen using 20 cycles, confirming the observations taken with the iU22 that little radiation force occurs when using short cycle lengths.

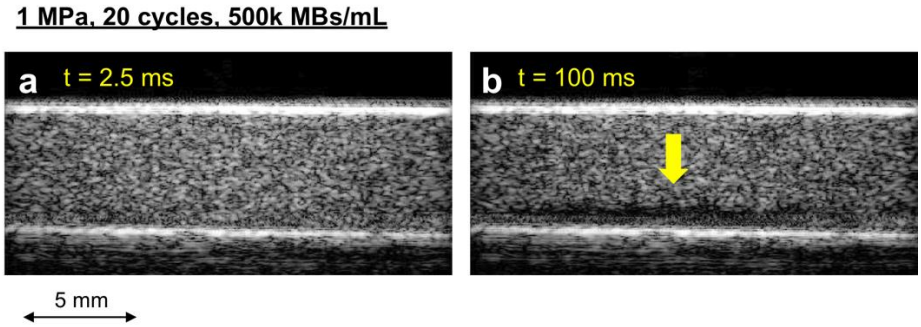

Fig. 4.8: High frame rate imaging of microbubble diffusion.

Images from an 8kHz acquisition taken after a 1 MPa, 20 cycle pulse through 500k MBs/mL. The time t = 0 denotes the firing of the pulse. There is no bubble destruction seen in (a), while a sizable void has developed in (b), implying that bubble elimination occurred via gas diffusion since no motion was observed.

High frame rate imaging with the Verasonics extended the findings from imaging with a diagnostic scanner; specifically, that secondary microbubble acoustic radiation force is dependent on the duration of the sound pulse as well as the microbubble concentration. Despite the high pressure excitation, total bubble elimination was minimal. In fact, only the 1000 cycle pulse shown in **Fig. 4.7 (e-h)** demonstrated complete bubble elimination through the length of the Clinicell for the acquisition duration studied. Even in this case, it was only after the resultant diffusion and bubble motion that the microbubbles were eliminated from the top membrane. These results imply that the bubble activity near the top membrane (where cells would normally be) is due to a complex combination of multiple phenomena and not just simply microbubble oscillations.

4.4 DISCUSSION

The propagation of sound through microbubble volumes in a typical *in vitro* sonoporation experimental setup was investigated with high-resolution conventional imaging and high frame rate plane wave imaging. Through this work, several important findings were observed. First, even high (for clinical standards) microbubble concentrations in a 3D volume still result in low bubble-to-cell ratios. At the highest microbubble concentration tested (10 million microbubbles/mL), the distance between bubbles is only about 50 μm. Compared with endothelial cell diameters of approximately 15 μm, these concentrations do not reach 1:1 bubble-to-cell ratios. That said, this is only an approximate calculation. If extrapolated to include bubble expansion beyond the initial radius, this ratio would be more favorable [19]. Regardless, the common usage of bubble-to-cell ratio as a ratio of the total number of microbubbles to total number of cells does not account for experimental geometry, rendering it a misleading statistic. Indeed, when the term was originally used, it was for cell suspensions and not monolayers [20], [21]. Additionally, void fraction was calculated and presented for the concentrations used in this study. Given the dispersity of microbubbles, the void fraction is very low (typically less than 10^{-4}) even at high concentrations. These two metrics imply that high bubble concentrations still yield sparse microbubble placement at typical literature parameters between 1 and 10 million microbubbles per mL [7], [12].

Despite low void fractions, high microbubble concentrations create large acoustic attenuation. The most striking result of the attenuation experiments is the extreme loss of pressure that occurs with increasing microbubble concentration. Even at low concentrations, between 100k and 1M microbubbles/mL, there can be up to a 50% loss in acoustic pressure. This result implies that for single pulsed sonoporation experiments through a volume of microbubbles, the *in situ* pressures meant to be delivered to microbubbles next to cells are not the pressures that would exist in the medium when bubbles are not present. Further, these observations remained similar between the custom formulation and SonoVue. It was observed that SonoVue created slightly more attenuation, likely because of its larger average size. This is consistent with prior work showing that larger bubbles have a more pronounced effect on sound attenuation [22].

From the attenuation experiments, two additional observations can be made: first, that the effect of concentration-dependent attenuation is more pronounced at higher pressures, and second, that higher microbubble concentrations yield stronger harmonic signal generation. As seen in **Fig. 4.4**, for both SonoVue and the custom microbubble, the received signal decreases at a higher rate when using 500 kPa than when using 125 kPa. This seems counterintuitive, as it would make sense that a higher pressure propagates further while destroying more bubbles. However, higher pressure pulses result in a more dramatic microbubble radius increase [19], [23] and therefore more attenuation, while smaller bubble oscillations at lower pressures are less attenuative to the overall beam.

Increasing the microbubble concentration also increased the amount of harmonic signal generation. This is shown in **Fig. 4.9d**, where at 10M microbubbles/mL, the strength and number of harmonic peaks generated from a 125 kPa transmit pulse is increased due to resonant scattering. Additionally, nonlinear propagation of sound in the medium (water) results in harmonic generation and thus alteration of the original frequency content, shown by the second harmonic peak in **Fig. 4.9b**, before microbubbles had been added. Therefore, not only does the presence of microbubbles affect the delivered pressure, but it also alters the frequency content of the ultrasound pulse that reaches the microbubbles adjacent to the cells of the monolayer.

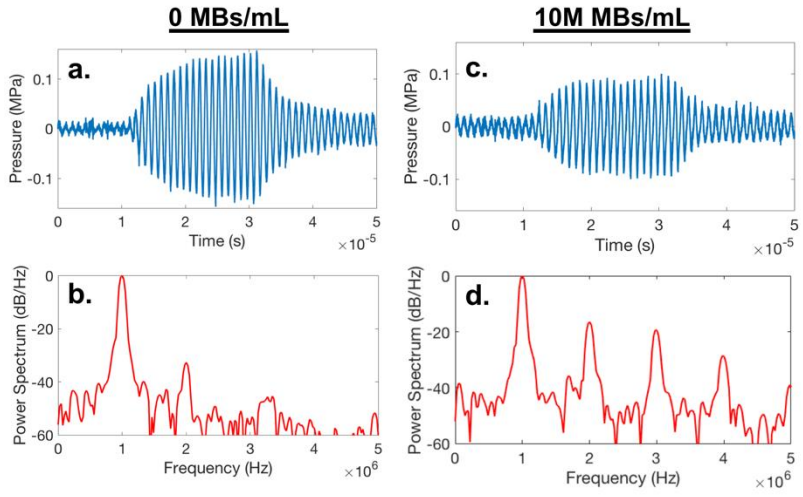

Fig. 4.9: Representative waveforms and power spectra of received pulses.

Waveforms and spectra are after a 125 kPa, 20 cycle pulse through either water or bubbles (10M MBs/mL). (a) and (c) show the time waveforms, and (b) and (d) show the spectra of those pulses, after cropping and windowing.

As stated before, sonoporation efficacy is dependent on microbubble concentration. It has been shown that there is more biological effect (be it sonoporation or cytotoxicity) at high microbubble concentrations [12], [21]. Paradoxically, achieving maximal bubble-to-cell ratios also substantially decreases available pressure to induce bubble oscillation near cell monolayers. Several groups have mitigated this issue by inverting the setup, such that ultrasound goes through cells first before insonifying microbubbles [24], [25]. While this does limit microbubble-dependent acoustic attenuation, it may still induce microbubble collapse and movement away from cells at destructive pressures, which could impact working microbubble concentration for maximum sonoporation effect. Nevertheless, the vast majority of published work to date used the monolayer/transducer orientation investigated with the present work [7], [11], [12].

Bubble destruction, gas diffusion, and movement were shown to be dependent on acoustic parameters and bubble concentration. The results from imaging the sonoporation process confirm and extend the findings from acoustic attenuation. The presence of microbubbles in a volume container affects both the pressure received as well as the acoustic environment itself. Pressure increase caused an increase in destruction area, which is intuitive given that a larger portion of a high pressure beam can still be above the microbubble destruction threshold. What is more surprising is that pressures as high as 1 MPa (MI of 1 at 1 MHz) at moderate microbubble concentrations still do not eliminate all microbubbles in the axial propagation path due to bubble-induced acoustic shadowing. This validates the observation shown in the attenuation experiments that high pressures still result in high attenuation. Pulse length (number of cycles) was also shown to impact the amount of bubble radiation force as well as bubble elimination that occurs following an ultrasound pulse. This can be seen in both the high-resolution imaging with the iU22, where the 1 MPa pulse at 200 cycles results in an intense movement phenomenon (**Fig. 4.6[a-d]),** and in the high frame rate imaging where 1000 cycles causes a swirling motion to occur (**Fig. 4.7[e-h]**). This is consistent with prior findings that cycle lengths above 200 are more likely to push microbubbles [26]. Additionally, as shown in **Fig. 4.7**, a larger number of cycles resulted in a larger region of bubble elimination. This is explained by the fact that microbubble shell integrity is compromised in just a few cycles but gas diffusion and complete elimination of the microbubble lasts on the order of milliseconds. Therefore, the difference between smaller and larger cycles may be attributed to microbubble fragmentation during long cycle oscillations and thus accelerated gas

diffusion. Finally, increasing the microbubble concentration not only increases the difficulty for sound to propagate through the volume, but also plays a role in bubble swirling and motion effects.

One additional observation seen from high frame rate imaging was the delineation between bubble destruction, gas diffusion, and bubble movement. As shown in **Fig. 4.7**, the initial bubble destruction occurs immediately, and is dependent on concentration, cycles, and pressure. However, this initial oscillation and destruction does not happen next to cells. It is clear from this result that bubble oscillation as the dominant form of cell permeation is not valid in this type of experimental setup. Rather, it is the subsequent bubble activity (diffusion and motion) due to a combination of a pressure gradient and inertial force that occurs within 100 ms of the dissolution of the microbubble shell [15], [18] that reaches cells in some cases.

Finally, the effect of repeated pulses was examined. As shown in the high frame rate images, a single pulse results in microbubble destruction, gas diffusion, and propagation. When this is repeated, as in the scenario using repeated pulses (or even long cycles), this effect is enhanced, and the complex gas diffusion and motion results in a continually changing microbubble concentration through the axial propagation direction. Therefore, not only does the pressure received through a volume of microbubbles change, but so too does the microbubble concentration next to cells. The microbubble concentrations that were assumed to be the "effective" concentrations will be inaccurate when examined after a series of repeated ultrasound pulses. Interestingly, it was observed that the rate at which pulse repetition occurs also has an effect on overall microbubble movement when using transmit parameters that induce bubble movement (such as long pulses). If the pulse repetition frequency is high enough such that the medium does not have time to return to steady state, then sending repeated pulses limits the amount of bubble movement that occurs for each pulse.

Although consideration was taken to accurately emulate common *in vitro* experimental designs, given the wide parameter space, testing all possible ultrasound combinations remains an impossible task. An additional limitation to this study was that the orientation of the Clinicell parallel to the water-air interface for optimal imaging induced standing waves that were not fully representative of a single source excitation. Orienting the setup at an angle would have mediated

this issue. That said, despite the limitations of parameter space and experimental setup, the outcomes and observations should remain universal: high microbubble concentrations are preferred for maximum probabilistic sonoporation efficacy, but the presence of microbubbles creates sound attenuation and a wide variety of post-excitation events, which work to confound the overall acoustic environment. Perhaps the only truly accurate way to understand sonoporation mechanism is through single cell-single bubble interactions [27], as opposed to using macroscopic experiments to understand microscopic events. Additionally, while these experiments were not conducted on cell monolayers, the goal of this work was not to evaluate *in vitro* sonoporation, but rather to understand and hopefully elucidate why sonoporation on cell monolayers has been inconclusive despite wide research in the area.

Even though this work was done purely as a characterization of an *in vitro* system, there are important points that can be applied to *in vivo* ultrasound-mediated therapy as well. The phenomenon of excess microbubble attenuation and acoustic shadowing at high microbubble concentrations is still relevant in highly perfused areas, and could cause unwanted pressure reduction at areas of interest for therapy [28]. Further, while microbubble streaming, the dominant microbubble phenomenon seen in our work, is probably more associated with *in vitro* experiments, complex microbubble post-excitation activity may still happen in large vessels *in vivo*. Finally, as shown in this work, achieving maximal "bubble-to-cell" ratios is a complicated task; however, these concentrations would similarly never be reachable *in vivo*. It is possible that the true mechanism behind ultrasound-mediated drug delivery *in vivo* is less about probabilistic encounters of bubbles near cells but more about other, more difficult to emulate phenomena, such as vascular damage, hyperthermia, or immune modulation [29]–[31].

The true complexity of trying to evaluate sonoporation by considering single variables (such as concentration or pressure or cycles) is that in a 3D volume, all variables impact each other. Increasing pressure increases the amount of cavitation (stable/inertial), which increases attenuation. Higher numbers of cycles result in more destruction and movement. High concentrations result in attenuation, and maintaining a constant concentration can be difficult when using repeated pulses. Further, since sonoporation is dependent on the distance between microbubbles and cells, trying

to elucidate mechanism in such a disperse and varied environment (both acoustically and physically) is an oversimplification of a complex process.

4.5 Conclusion

Through this work, we have characterized a setup commonly used to evaluate *in vitro* sonoporation. We have shown that the confounding microbubble activity during sonoporation in cell enclosures is quite complex and is a result of spatially and temporally varying acoustic fields and bubble concentrations. Specifically, bubble elimination in cell enclosures is impacted by pressure, pulse duration, bubble concentration, and pulse repetition, all of which are common parameters that have been explored in previous works. This complex environment and transient spatiotemporal bubble and pressure variations make it impossible to study sonoporation in cell enclosures in a standardized and reproducible way. It is fair to say that the actual pressure and concentration values in some of the previously reported works were quite possibly not what were originally intended. Perhaps the most important conclusion from this work is that unless studies look explicitly at single bubble-single cell sonoporation, it is impossible to separate the wide variety of parameters into single variables. Pressure and concentration affect microbubble behavior, while microbubble behavior affects *in situ* pressure and concentration. Trying to form conclusions about macroscale sonoporation outcome will therefore be both varied and confounding.

4.6 References

[1] S. Mitragotri, "Healing sound: the use of ultrasound in drug delivery and other therapeutic applications," *Nat. Rev. Drug Discov.*, vol. 4, no. 3, pp. 255–260, Mar. 2005.

[2] K. Kooiman, H. J. Vos, M. Versluis, and N. De Jong, "Acoustic behavior of microbubbles and implications for drug delivery," *Adv. Drug Deliv. Rev.*, vol. 72, pp. 28–48, 2014.

[3] R. Bekeredjian, S. Chen, P. A. Grayburn, and R. V Shohet, "Augmentation of cardiac protein delivery using ultrasound targeted microbubble destruction.," *Ultrasound Med. Biol.*, vol. 31, no. 5, pp. 687–91, May 2005.

[4] R. Suzuki, Y. Oda, N. Utoguchi, and K. Maruyama, "Progress in the development of ultrasound-mediated gene delivery systems utilizing nano- and microbubbles," *J. Control. Release*, vol. 149, no. 1, pp. 36–41, Jan. 2011.

[5] P. Qin, T. Han, A. C. H. Yu, and L. Xu, "Mechanistic understanding the bioeffects of ultrasound-driven microbubbles to enhance macromolecule delivery," *J. Control. Release*, vol. 272, pp. 169–181, Feb. 2018.

[6] K. Ferrara, R. Pollard, and M. Borden, "Ultrasound Microbubble Contrast Agents: Fundamentals and Application to Gene and Drug Delivery," *Annu. Rev. Biomed. Eng*, vol. 9, pp. 415–47, 2007.

[7] I. De Cock *et al.*, “Ultrasound and microbubble mediated drug delivery: acoustic pressure as determinant for uptake via membrane pores or endocytosis,” *J. Control. Release*, vol. 197, pp. 20–28, 2015.
[8] R. Karshafian, P. D. Bevan, R. Williams, S. Samac, and P. N. Burns, “Sonoporation by Ultrasound-Activated Microbubble Contrast Agents: Effect of Acoustic Exposure Parameters on Cell Membrane Permeability and Cell Viability,” *Ultrasound Med. Biol.*, vol. 35, no. 5, pp. 847–860, May 2009.
[9] G. Shapiro *et al.*, “Multiparameter evaluation of in vivo gene delivery using ultrasound-guided, microbubble-enhanced sonoporation,” *J. Control. Release*, vol. 223, pp. 157–164, Feb. 2016.
[10] K. Iwanaga *et al.*, “Local delivery system of cytotoxic agents to tumors by focused sonoporation,” *Cancer Gene Ther.*, vol. 14, no. 4, pp. 354–363, Apr. 2007.
[11] B. Helfield, X. Chen, S. C. Watkins, and F. S. Villanueva, “Biophysical insight into mechanisms of sonoporation,” *Proc. Natl. Acad. Sci.*, p. 201606915, 2016.
[12] T. van Rooij *et al.*, “Viability of endothelial cells after ultrasound-mediated sonoporation: Influence of targeting, oscillation, and displacement of microbubbles,” *J. Control. Release*, vol. 238, pp. 197–211, 2016.
[13] M. Wang, Y. Zhang, C. Cai, J. Tu, X. Guo, and D. Zhang, “Sonoporation-induced cell membrane permeabilization and cytoskeleton disassembly at varied acoustic and microbubble-cell parameters,” *Sci. Rep.*, vol. 8, no. 1, p. 3885, Dec. 2018.
[14] Z. Fan, D. Chen, and C. X. Deng, “Characterization of the dynamic activities of a population of microbubbles driven by pulsed ultrasound exposure in sonoporation.,” *Ultrasound Med. Biol.*, vol. 40, no. 6, pp. 1260–72, Jun. 2014.
[15] N. de Jong, M. Emmer, A. van Wamel, and M. Versluis, “Ultrasonic characterization of ultrasound contrast agents.,” *Med. Biol. Eng. Comput.*, vol. 47, no. 8, pp. 861–73, Aug. 2009.
[16] Y. Hu, J. M. F. Wan, and A. C. H. Yu, “Membrane Perforation and Recovery Dynamics in Microbubble-Mediated Sonoporation,” *Ultrasound Med. Biol.*, vol. 39, no. 12, pp. 2393–2405, Feb. 2018.
[17] Y. Hu, J. M. F. Wan, and A. C. H. Yu, “Membrane Perforation and Recovery Dynamics in Microbubble-Mediated Sonoporation,” *Ultrasound Med. Biol.*, vol. 39, no. 12, pp. 2393–2405, 2013.
[18] P. S. Epstein and M. S. Plesset, “On the Stability of Gas Bubbles in Liquid-Gas Solutions,” *J. Chem. Phys.*, vol. 18, no. 11, pp. 1505–1429, 1950.
[19] S. Qin, C. F. Caskey, and K. W. Ferrara, “Ultrasound contrast microbubbles in imaging and therapy: physical principles and engineering.,” *Phys. Med. Biol.*, vol. 54, no. 6, pp. R27-57, Mar. 2009.
[20] M. Ward, J. Wu, and J.-F. Chiu, “Experimental study of the effects of optison® concentration on sonoporation in vitro,” *Ultrasound Med. Biol.*, vol. 26, no. 7, pp. 1169–1175, Sep. 2000.
[21] H. R. Guzmán, A. J. McNamara, D. X. Nguyen, and M. R. Prausnitz, “Bioeffects caused by changes in acoustic cavitation bubble density and cell concentration: a unified explanation based on cell-to-bubble ratio and blast radius,” *Ultrasound Med. Biol.*, vol. 29, no. 8, pp. 1211–1222, Aug. 2003.
[22] N. de Jong, L. Hoff, T. Skotland, and N. Bom, “Absorption and scatter of encapsulated gas filled microspheres: Theoretical considerations and some measurements,” *Ultrasonics*,

vol. 30, no. 2, pp. 95–103, Mar. 1992.
[23] I. Lentacker, I. De Cock, R. Deckers, S. C. De Smedt, and C. T. W. Moonen, "Understanding ultrasound induced sonoporation: Definitions and underlying mechanisms," *Adv. Drug Deliv. Rev.*, vol. 72, pp. 49–64, 2014.
[24] P. Qin, L. Xu, T. Han, L. Du, and A. C. H. Yu, "Effect of non-acoustic parameters on heterogeneous sonoporation mediated by single-pulse ultrasound and microbubbles," *Ultrason. Sonochem.*, vol. 31, pp. 107–115, 2016.
[25] J. Park, Z. Fan, and C. X. Deng, "Effects of shear stress cultivation on cell membrane disruption and intracellular calcium concentration in sonoporation of endothelial cells.," *J. Biomech.*, vol. 44, no. 1, pp. 164–9, Jan. 2011.
[26] C. Mannaris and M. A. Averkiou, "Investigation of Microbubble Response to Long Pulses Used in Ultrasound-Enhanced Drug Delivery," *Ultrasound Med. Biol.*, vol. 38, no. 4, pp. 681–691, Apr. 2012.
[27] Z. Fan, H. Liu, M. Mayer, and C. X. Deng, "Spatiotemporally controlled single cell sonoporation.," *Proc. Natl. Acad. Sci. U. S. A.*, vol. 109, no. 41, pp. 16486–91, Oct. 2012.
[28] J. Song, A. L. Klibanov, J. A. Hossack, and R. J. Price, "Acoustic Attenuation by Contrast Agent Microbubbles in Superficial Tissue Markedly Diminishes Petechiae Bioeffects in Deep Tissue," *Invest. Radiol.*, vol. 43, no. 5, pp. 322–329, May 2008.
[29] D. E. Goertz *et al.*, "Antitumor Effects of Combining Docetaxel (Taxotere) with the Antivascular Action of Ultrasound Stimulated Microbubbles," *PLoS One*, vol. 7, no. 12, p. e52307, Dec. 2012.
[30] R. G. Holt and R. A. Roy, "Measurements of bubble-enhanced heating from focused, mhz-frequency ultrasound in a tissue-mimicking material," *Ultrasound Med. Biol.*, vol. 27, no. 10, pp. 1399–1412, Oct. 2001.
[31] H.-L. Liu, H.-Y. Hsieh, L.-A. Lu, C.-W. Kang, M.-F. Wu, and C.-Y. Lin, "Low-pressure pulsed focused ultrasound with microbubbles promotes an anticancer immunological response.," *J. Transl. Med.*, vol. 10, p. 221, Nov. 2012.

Chapter 5. IMAGE-GUIDED TREATMENT OF PRIMARY LIVER CANCER IN MICE LEADS TO VASCULAR DISRUPTION AND INCREASED DRUG PENETRATION[4]

Sara B. Keller, Dingjie Suo, Yak-Nam Wang, Heidi Kenerson,
Raymond S. Yeung, Michalakis A. Averkiou

Abstract

Despite advances in interventional procedures and chemotherapeutic drug development, hepatocellular carcinoma (HCC) is still the fourth leading cause of cancer-related deaths worldwide with a <30% 5-year survival rate. This poor prognosis can be attributed to the fact that HCC most commonly occurs in patients with pre-existing liver conditions, rendering many treatment options too aggressive. Patient survival rates could be improved by a more targeted approach. Ultrasound-induced cavitation can provide a means for overcoming traditional barriers defining drug uptake. The goal of this work was to evaluate preclinical efficacy of image-guided, cavitation-enabled drug delivery with a clinical ultrasound scanner. To this end, ultrasound conditions (unique from those used in imaging) were designed and implemented on a Philips EPIQ and S5-1 phased array probe to produced focused ultrasound for cavitation treatment. SonoVue® microbubbles which are clinically approved as an ultrasound contrast agent were used for both imaging and cavitation treatment. A genetically engineered mouse model was bred and used as a physiologically relevant preclinical analog to human HCC. It was observed that image-guided and targeted microbubble cavitation resulted in selective disruption of the tumor blood flow and enhanced doxorubicin uptake and penetration. Histology results indicate that no gross morphological damage occurred as a result of this process. The combination of these effects may be exploited to treat HCC and other challenging malignancies and could be implemented with currently available ultrasound scanners and reagents.

[4] *Reprinted with permission from Keller, SB et al. "Image-Guided Treatment of Primary Liver Cancer in Mice Leads to Vascular Disruption and Increased Drug Penetration" Front. Pharmacol. 2020.*

5.1 INTRODUCTION

Hepatocellular carcinoma (HCC) is the sixth most common cancer globally and the fourth leading cause of cancer-related deaths [1], [2]. The high case mortality rate can be attributed to the delay in diagnosis, lack of effective systemic therapy, and pre-existing liver disease that limits hepatic reserve. The major risk factors for HCC are the same as those causing liver cirrhosis including alcoholism, hepatitis B/C, and steatohepatitis. Consequently, treatment options and prognosis depend not only on tumor characteristics, but also the extent of liver dysfunction, rendering many strategies too aggressive. Emerging therapies have focused on more precise tumor targeting while sparing non-tumor liver [3], [4].

One such approach is the use of vascular disruption agents (VDAs) to restrict blood flow to the tumor [5]. However, small-molecule VDAs such as combrestatin A-4 phosphate (CA4P) and 5, 6-dimethylxanthenone-4-acetic acid (DMXAA) are often associated with poor side effects and can result in drug resistance in some cases [4], [6]. Ultrasound-mediated microbubble cavitation has been shown to recapitulate the vascular disruptive effect with more precise targeting, thereby limiting side effects [7]. The immature neovessels within angiogenic tumors are abnormal, with nonuniform vessel diameters, irregular branching, and heterogeneous blood flow patterns [8]. It is hypothesized that these aberrant architectures make the vasculature of tumors more vulnerable to the mechanical effects of cavitation than surrounding non-tumor tissue. Therefore, it has been shown that cavitation-induced vascular disruption can be selectively applied to the tumor microvascular network, while avoiding damage to surrounding tissue [7]. Cavitation activity within the irregular tumor microvasculature causes selective vascular shutdown, hypothesized to be a result of a decrease in microvascular density due to widespread endothelial cell toxicity and vascular depletion [7]. Indeed, several studies have shown significant blood flow restriction to tumor neovessels with cavitating microbubbles at modest ultrasound pressures (1-5 MPa) with minimal non-tumorous tissue damage. Goertz et. al showed significant reduction of blood flow in the central area of tumors after therapy with 1.65 MPa at a frequency of 1 MHz [9]. In a study performed by Wang et. al, microvascular density was significantly reduced 24 hours after therapy with pressures beyond 1.5 MPa, with no damage to surrounding tissue until the sonication pressure reached 5 MPa [7]. Finally, Liu et al observed complete cessation of tumor blood flow after therapy

with 4.8 MPa that could last as long as 24 hours, which resulted in widespread necrosis to the tumor region [10].

Despite these successes, tumor hypoxia as a sole strategy for cancer treatment can often have the unintended consequence of an increased proliferative phenotype in remaining tumor cells and endothelial cells [5], [6], [11]. Moreover, prior work suggests that the effect of vascular shutdown may be offset by an opposing 'vascular rebound', since the cancer cells that remain after therapy tend to be more aggressive, often resulting in worse clinical outcomes [5], [9]. Therefore, a synergistic approach to targeting both the aberrant neovessels in the tumor core through cavitation-mediated vascular disruption and the proliferative outer rim of the tumor through enhanced cytotoxic drug penetration may be necessary to overcome these limitations [9], [12].

Previous studies that have examined ultrasound-mediated vascular disruption with or without drug delivery *in vivo* have generally used simplistic single element transducers for the ultrasound treatment which limits clinical translation [9], [13], [14]. Single element focused transducer systems provide a great deal of flexibility for parameter optimization, but they are cumbersome to use due to requiring auxiliary components (function generators, amplifiers, etc.) and they are not capable of imaging. In addition, the use of custom devices in clinical trials requires regulatory approval, which is a complex process. Because of this, there has been a clear trend from single element transducers towards clinical imaging transducers for ultrasound therapy. However, the lack of ability to modify scanner pulsing parameters has limited innovation in this area. Indeed, in a Phase I clinical trial using ultrasound and microbubbles to enhance gemcitabine delivery to pancreatic cancer [15], the investigators chose to use normal imaging modes with short sound pulses for therapy, despite the fact that their previous studies indicated that "sonoporation had a significant therapeutic effect when using long pulse durations". It can be inferred that the authors of the reported study were unable to create the acoustic parameters necessary for maximally effective therapy. More recently, O'Neil et al. reported using a Philips X5-1 for interleaved imaging and therapy for tissue perfusion augmentation [16]. While the application of that work was not targeted drug delivery and therefore wide beam areas were preferred, it still represents an important example of the adaptation of clinical ultrasound technology for interventional procedures.

The main objective of the present work is to evaluate preclinical efficacy of image-guided, cavitation-induced vascular disruption and drug uptake enhancement using a clinical ultrasound scanner in a physiologically relevant mouse model of primary liver cancer, defined in the present manuscript as UltraSound Cavitation Treatment (USCTx). Our hypothesis is that using a clinical diagnostic probe to perform USCTx along with clinical microbubbles will result in vascular disruption and greater doxorubicin delivery in treated tumors. To the best of our knowledge, we believe that this is the first study to incorporate clinically available tools and reagents in a pre-clinical *in vivo* model of genetically engineered mice to highlight the combined effects of vascular disruption and drug delivery. If successful, this would be a simple, inexpensive, and easily implementable clinical technique for treating human liver tumors.

5.2 MATERIALS AND METHODS

5.2.1 *Breeding of Pten-null mouse model*

All animal work was conducted in accordance with national guidelines and was approved by the Institutional Animal Care and Use Committee (IACUC) at the University of Washington, Seattle. 8 week old male albumin (Alb)-Cre mice (003574, B6.Cg-Tg(Alb-cre)21Mgn/J) and 8-week old female $Pten^{fl/fl}$ mice (006440, B6.129S4-Ptentm1Hwu/J) were purchased from Jackson Laboratory (Bar Harbor, ME). Alb-Cre mice were bred with $Pten^{fl/fl}$ mice to ultimately generate $Pten^{fl/fl}$;Alb^{cre} experimental mice. Genotyping protocols and primers were obtained from Jackson Laboratory, and PCR was performed to confirm the correct genotype. At 40 weeks of age, $Pten^{fl/fl}$;Alb^{cre} (*Pten*-null) mice develop tumors that are physiologically similar to human HCCs and ICCs (intrahepatic cholangiocarcinoma) [17], [18]. Moreover, the mice develop hepatic steatosis, resulting in livers that are abnormally large preceding tumorigenesis. Tumor progression was monitored through weekly ultrasound scans with an L15-7io imaging probe on a Philips iU22 (Philips Medical Systems, Bothell, WA) starting at 36 weeks of age. Mice (20 male and 18 female) were treated once tumors were 1 cm in diameter.

5.2.2 *Drug and contrast agents*

Doxorubicin was used as the chemotherapeutic drug as it is detectable using fluorescent imaging. Although clinically, the liposomal formulation of doxorubicin, Doxil, is favored over the free drug, we chose to use free doxorubicin for simplicity, and note that it could be easily replaced by a wide variety of other small molecule drugs. Furthermore, the benefits of using Doxil over doxorubicin (ie, limiting cardiotoxicity) would not be relevant in the current study due to the acute timeline of the experiments. Doxorubicin HCl was purchased and dissolved in sterile saline at a concentration of 10 mg/ml and mice received a dosing level of 30 mg/kg [19]. SonoVue®, marketed in the US as Lumason® (Bracco Suisse SA, Geneva, Switzerland), was the contrast agent used for these studies and was resuspended according to the manufacturer's instructions. Microbubble concentration was measured using a Multisizer 3 (Beckman Coulter, Brea, CA, USA) and found to consistently be between $1\text{-}5\times10^8$ microbubbles/mL. Microbubble dosing was evaluated through preliminary experiments in which it was observed that 50 μL injections gave adequate contrast without acoustic shadowing [20] and therefore that dosing regimen was used for all further experiments.

5.2.3 *Acoustic parameters*

Focused ultrasound beams suitable for USCTx were designed and implemented on a Philips EPIQ scanner and S5-1 phased array operating in a hybrid pulsed-wave Doppler mode. A deep focal length of 10 cm was chosen to allow for a broader collimated beam in the nearfield (1-2 cm) where the liver tumor in the mice would be. The scanner was modified to produce 200 cycles at a pulse repetition frequency (PRF) of 50 Hz at acoustic pressures ranging between 2-3 MPa [21] at a center frequency of 1.6 MHz.. The output pressure could be easily modified by changing the transmit voltage to the probe in the same fashion as done during clinical scanning. The specific ultrasound parameters were selected to be consistent with prior work studying cavitation induced treatments with ultrasound and microbubbles [7], [9], [10]. The spatial extent of the sound field in both the azimuth and elevation planes at the chosen transmit voltage (100 V) were measured in a water tank with a 0.4 mm membrane hydrophone (Precision Acoustics Ltd., Dorchester, UK), acquired using a DPO7054C Oscilloscope (Tektronix, Inc., Beaverton, OR, USA) and analyzed in MATLAB

(The MathWorks, Inc., Natick, MA, USA). The delivered acoustic pressure in the mice may be calculated by derating the water measurements according to account for attenuation.

5.2.4 *Treatment procedure*

Mice were anesthetized under 1-3% isoflurane and placed supine on a sound-absorbing pad to minimize sound reverberations (**Fig. 5.1**). After depilating the abdomen of the mouse, pre-treatment b-mode images were taken to orient the imaging plane in the center of the tumor. An overview of the experimental timeline may be seen in **Fig. 5.2**. Two ultrasound scanners, one for USCTx (EPIQ) and one for imaging (iU22) were used. A pre-treatment contrast-enhanced ultrasound (CEUS) scan was performed with a Philips iU22 and L12-5 linear array probe on all mice. 50 μL SonoVue® was injected retro-orbitally and 60 s CEUS loops were recorded. The L12-5 was then removed and the S5-1 probe of the EPIQ with programmed long pulses (described in the previous section) was positioned over the same area. This timing also allowed for clearance of microbubbles from pre-treatment CEUS imaging. Treatment consisted of doxorubicin (DOX) with or without USCTx. Mice were randomly split into focused ultrasound (DOX + USCTx) or control (DOX alone) cohorts. There were 10 male and 9 female mice in each group. Mice receiving USCTx received 4 injections of DOX + MBs over one anesthesia event. Each injection was followed by focused ultrasound treatment 30 s after injection which alternated between "on" for 5 s and "off" for 5 s [22], for a total "on" time of 30 s. The start time of 30 s was chosen based on evaluating bolus transit in preliminary contrast injections [23], and the multiple injection regimen was chosen to maximize the time in which ultrasound affected microbubbles at peak bolus concentrations [22]. Time intensity curve (TIC) analysis [24] was used to determine the optimal time for treatment (**Fig. 5.3**). Control animals received doxorubicin alone without USCTx. The total doxorubicin amount in control animals was divided into 4 injections with a 90 s waiting period between injections to mimic the timing of ultrasound in the USCTx cohort. 30 min after the last injection, mice were euthanized via transcardial perfusion and samples of tumor and healthy liver were embedded in optimum cutting temperature (OCT) compound for sectioning. Tumor versus non-tumor tissue could be delineated based on gross anatomical morphology after dissection (**Fig. 5.3b**). Half of the tumor tissue was frozen for sectioning. The other half of the tumor tissue, along with non-tumorous liver parenchyma, heart, kidney, spleen, and muscle were removed and frozen at -80°C for doxorubicin extraction.

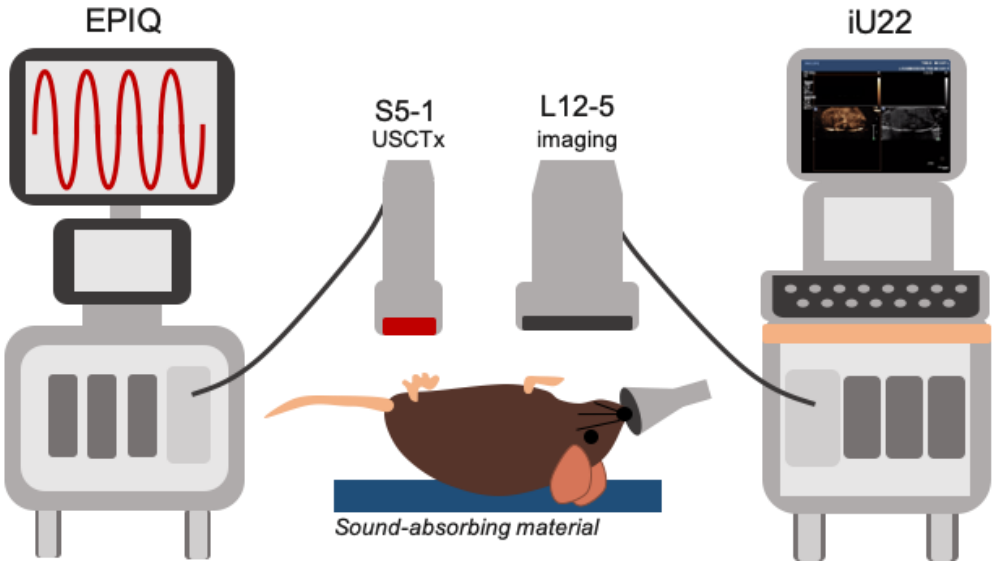

Fig. 5.1: Overview of experimental setup for *in vivo* USCTx treatment and imaging.

The EPIQ and S5-1 probe were programmed to produce ultrasound conditions for cavitation treatments. The iU22 with the L12-5 probe were used for contrast enhanced ultrasound (CEUS) imaging before and after cavitation treatments as well as routine monitoring of tumor growth. Mice were placed on a sound-absorbing material to minimize sound reverberations.

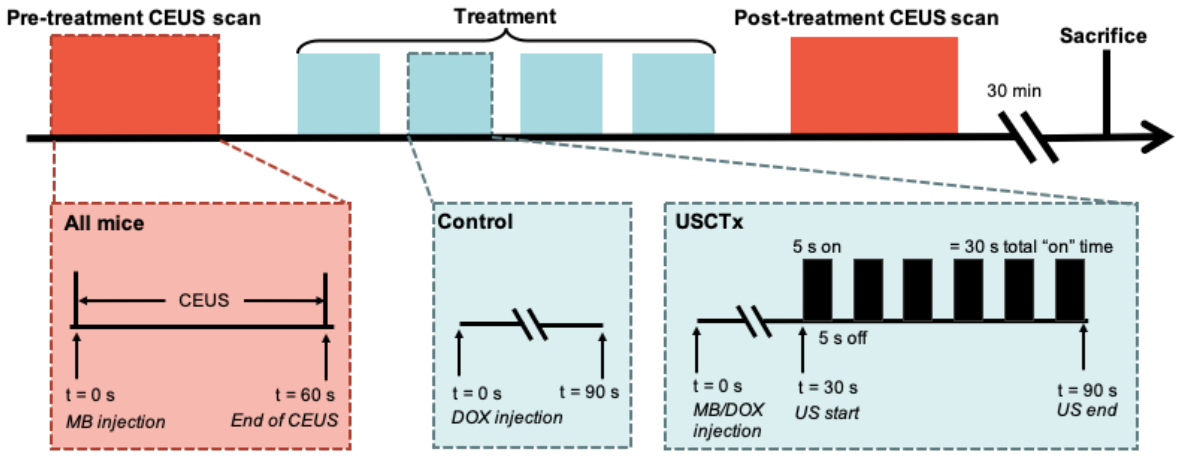

Fig. 5.2: Overview of experimental protocol for USCTx.

60 s CEUS loops were taken before and after therapy on all mice, regardless of experimental group. Treatment is defined by 4 injections of DOX alone (control) or DOX + USCTx. There were 90 s between each injection. The mice were sacrificed 30 min after the post-treatment CEUS exam.

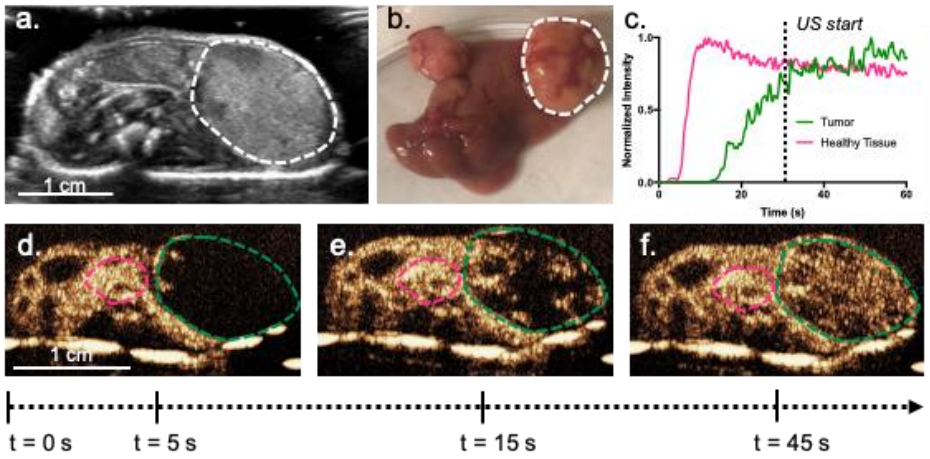

Fig. 5.3: Timing for treatment based on TIC analysis.

(a) Representative cross-sectional B-mode image of a mouse with a tumor (bounded by dashed line) taken with the L12-5. Tumors can be easily delineated by gross anatomical morphology, as in (b). Example TICs from the tumor and the normal parenchyma are shown in (c) with (d)-(f) showing the original CEUS images and ROIs, where the green line is the tumor and the pink line is healthy tissue. Intensity was normalized to peak intensity within each respective ROI, in order to highlight differences in time parameters. In this example, the tumor does not reach its peak intensity until after the 60 s. The wash-in of microbubbles is slower in the tumor than the surrounding tissue. USCTx was chosen to start at 30 s, when the tumor had sufficient microbubble accumulation.

5.2.5 *CEUS evaluation of vascular disruption*

CEUS pre- and post- treatment video loops (extracted as native DICOM data [24]) were analyzed qualitatively for image intensity in tumor and non-tumor liver areas, as well as quantitatively using TIC analysis in QLAB (Philips Healthcare, Bothell, WA, USA). Contrast agent rise time (RT), which is inversely proportional to blood flow [25], and peak intensity (PI), which is a measure of vascular volume [13], were measured as indicators of perfusion changes [22]. Regions of interest (ROIs) were drawn as freeform polygons in tumor and non-tumor areas on the contrast image. The intensity within an ROI is the average intensity of the pixels over the entire area. RT was calculated as the time it took from microbubbles arriving in each ROI (tumor and non-tumor) to the peak of contrast intensity. Change in RT (ΔRT) is expressed as the post-treatment RT minus the pre-treatment RT and therefore higher values of ΔRT would indicate a slower perfusion rate in the ROI as a result of treatment. PI within the tumoral area was calculated as the maximum contrast intensity within the ROI and was normalized to an ROI of surrounding non-tumor tissue intensity in order to account for differences in microbubble injections. Change in PI is expressed as a ratio

of the post-treatment PI divided by the pre-treatment PI and therefore a value less than 1 would indicate a reduced PI in the ROI as a result of treatment. Since the intensity within the non-tumor region was used for normalization, changes in non-tumor PI were not evaluated. Perfusion parameters from 25 (11 control and 14 treated) tumors were analyzed. Loops from mice that had inadequate bubble delivery and/or had obvious differences in probe placement pre- and post-treatment were not analyzed for perfusion changes due to potential for inaccuracies.

5.2.6 *Quantification of doxorubicin uptake*

Quantification of doxorubicin uptake was performed as described previously [26]. Briefly, nuclear lysis (RIPA) buffer (50 mM Tris•HCl, 150 mM NaCl, 1% Triton X-100, 0.5% Sodium Deoxycholate, 0.1% SDS, 1mM EDTA, 10 mM NaF, 1 mM PMSF, in ddH_20) was added to frozen tissue samples (20% w/v) in 2 mL centrifuge tubes and homogenized on ice with hard tissue homogenizer tips (Omni International, Kennesaw, GA, USA). 200 μL of tissue homogenate was removed and added to a 2 mL microcentrifuge tube, along with 100 μL 10% v/v Triton X-100, 200 μL ddH_2O, and 1500 μL 0.75 N acidified isopropanol. Samples were vortexed and then left at -20°C for overnight extraction. The next day, samples were warmed to room temperature, vortexed, and centrifuged at 15,000*xg* for 20 minutes. The supernatant was added to a 96 well plate and analyzed for fluorescence intensity (480 nm Ex; 605 nm Em) using a plate reader (Infinite 200 PRO, Tecan, Austria). Fluorescence was compared against a standard curve of known absolute doxorubicin amounts added to untreated tissue homogenate. Doxorubicin amount is presented in micrograms (per equivalent tissue homogenate mass). Samples were omitted if the tumor or organ volume was insufficient to get an accurate reading.

5.2.7 *Fluorescence microscopy and histologic examination*

Serial sections of 5 μm thickness were taken from OCT-embedded tumor and liver samples from all mice using a Leica CM 1950 Cryostat (Leica Biosystems). At up to three different locations near the central region of the tumor, one section was analyzed qualitatively for doxorubicin presence using a custom filter set (480/40 nm Ex; 605/50 nm Em; dichroic, 505 lp). The second section was stained with anti-CD31 (Abcam, Cambridge, United Kingdom) for evaluation of microvascular integrity. The final section was stained with hematoxylin and eosin (H&E) for anatomical morphology, which enabled segregation of tumor and non-tumor tissue, and was used

to evaluate gross morphological damage. CD31 and H&E staining were performed by the UW Histology and Imaging Core.

5.2.8 *Statistical analysis*

Doxorubicin uptake between control and USCTx treated groups was compared using a Mann-Whitney test. Change in RT and post-PI divided by pre-PI were compared between control and USCTx treated groups using an unpaired Student's *t*-test. Statistical analyses were performed in GraphPad Prism version 7.0 for Mac (GraphPad Software, San Diego, CA, USA). For all analyses, the significance level was set to 0.05.

5.3 RESULTS

5.3.1 *Measured acoustic sound field from clinical device*

Hydrophone measurements of the ultrasound pressure field in the azimuthal and elevational planes in water of the S5-1 clinical probe (used for USCTx) can be seen in **Fig. 5.4a** and **b**, respectively. The black line represents the -6 dB contours of the maximum spatial extent (area of up to half the maximum amplitude). The azimuthal beam width (**Fig. 5.4a**) is about 1 cm in diameter and reaches pressures up to 2.5 MPa (in this specific amplitude setting). The elevational beam width (**Fig. 5.4b**) is slightly narrower (0.5 cm). Given that mice were treated once their tumors reached approximately 1 cm in diameter, it can be extrapolated that the beam covered essentially the entire tumor area. Despite the fact that a diagnostic ultrasound device was used to generate these beams, it can be seen that the amplitude is slightly higher than the FDA limit of 1.9 MI given the transmit frequency of 1.6 MHz. Since these measurements are in water, to find the actual *in situ* pressure in the mice we must adjust for attenuation at a 0.3 dB/(cm-MHz) [27]. Since the tumors were generally located within 2 cm of the transducer face, attenuation was minimal (approximately 0.96 dB, corresponding to a loss of 10% of the transmitted pressure). Since the tumors were generally located within 2 cm of the transducer face, attenuation was minimal (approximately 0.96 dB, corresponding to a loss of 10% of the transmitted pressure). We note that the probe is in a hybrid PW Doppler mode and the number of cycles and acoustic pressure are not what would be used in standard Doppler imaging.

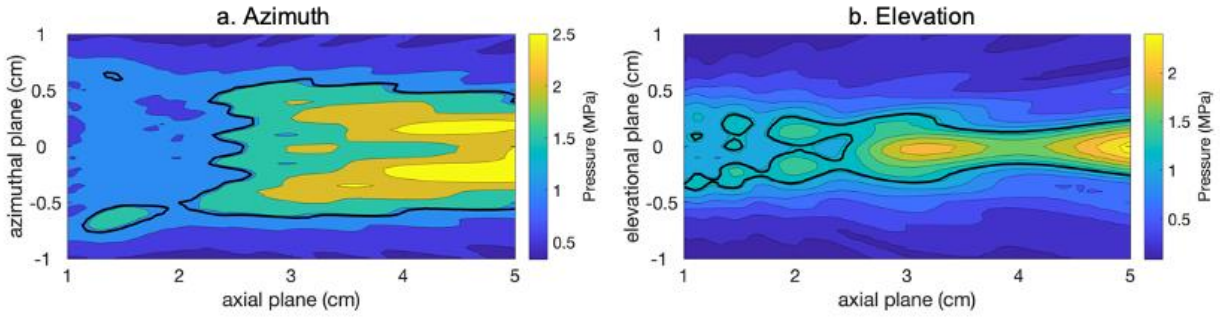

Fig. 5.4: 2D sound fields of the therapeutic beam from the S5-1 in azimuth (a) and elevation (b) planes.

5.3.2 *Vascular disruption measured by qualitative and quantitative CEUS*

Fig. 5.5 shows CEUS images from pre- and post-treatment loops. The top row **(a,d,g,j)** shows the anatomical b-mode image, and the middle **(b,e,h,k)** and bottom **(c,f,i,l)** rows show the contrast images acquired 15 s after a bolus injection before treatment and after treatment, respectively. There was no reduction in contrast in the tumors shown in the control mice post-therapy **(c,f)**. However, for mice treated with USCTx, areas of perfusion deficits may be seen in **(i.l)**. Any differences in the overall image brightness is attributed to differences in the actual microbubble concentration delivered with the bolus injection.

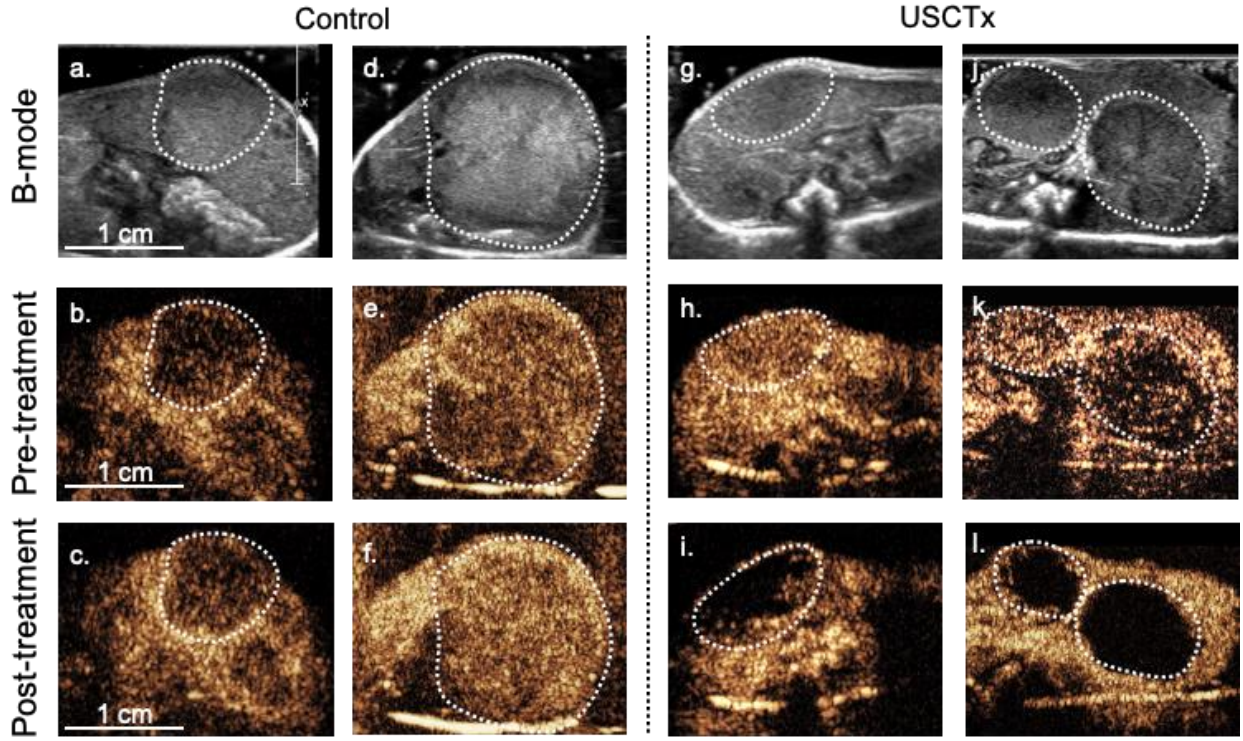

Fig. 5.5: Qualitative CEUS results from USCTx.

Each column represents four different mice with tumors indicated by the dashed white line; (a-c) and (d-f) did not undergo USCTx while (g-i) and (j-l) did undergo USCTx. The top row (a,d,g,j) shows the initial b-mode images, the middle row (b,e,h,k) shows CEUS images taken 15 s after microbubble injection before treatment, and the bottom row (c,f,i,l) shows CEUS images taken 15 s after microbubble injection after treatment. Note reduced presence of microbubbles post-treatment in the USCTx mice (i,l) and similarities in microbubble presence in the control mice (c,f).

Fig. 5.6 shows quantitative analysis of CEUS loops. Representative tumor TICs from control and USCTx mice are shown in (**a**) and (**b**), respectively. Signal intensity in these representative TICs were normalized to the maximum intensity in each individual ROI (such that the maximum intensity in each TIC equals 1) in order to better visually demonstrate the time it took from the beginning of the bolus to the peak (defined as RT), and it can be seen that the RT in the control mouse remained around 5 s, whereas the RT increased to over 40 s in the USCTx mouse. Summary data can be seen in (**c**) and (**d**), where USCTx caused a significant increase in ΔRT within the tumor ($p < 0.001$). This means that USCTx, on average, increased RT by 34.6 s. There were no significant differences in ΔRT seen in non-tumor (surrounding liver) tissue from USCTx treated mice as well as tumor and non-tumor tissue from control mice. USCTx also resulted in significant reduction in tumor PI ($p < 0.01$). Example ROIs may be seen in (e) and (f), where the tumor is bounded in blue and the non-tumor area in green.

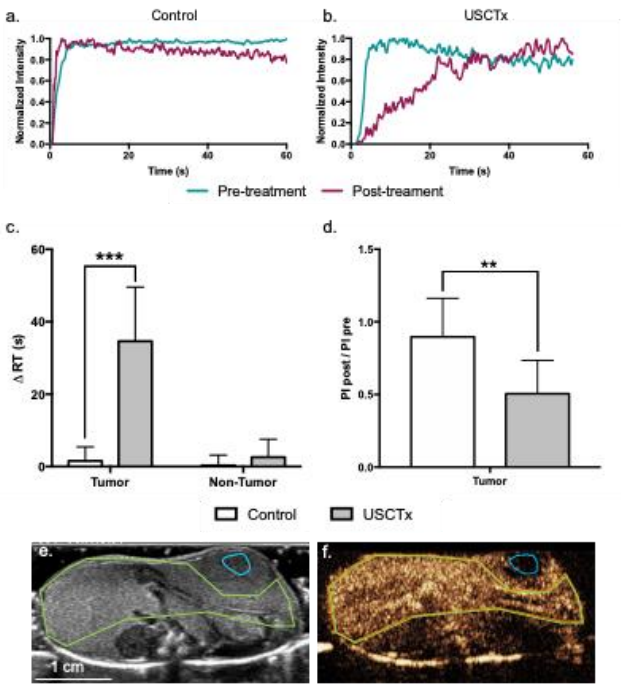

Fig. 5.6: Quantitative CEUS results from USCTx.

Representative TICs from control (a) and USCTx (b) mice within the tumor. Signal intensity was normalized to the maximum intensity in each individual ROI in order to better visually demonstrate change in time parameters as in **Fig. 5.3**. Quantification of ΔRT in control and USCTx mice in the tumor and non-tumor liver is shown in (c). Post-treatment PI divided by pre-treatment PI within the tumor is shown in (d). ROIs showing the tumor (blue) and non-tumor tissue (green) is shown in b-mode (e) and contrast (f). **p<0.01, ***p < 0.001.

5.3.3 *Qualitative and quantitative doxorubicin uptake*

Fig. 5.7 shows quantification of doxorubicin uptake by fluorescence analysis. Doxorubicin amount is presented in micrograms (per equivalent tissue homogenate mass). There was a significant ($p < 0.001$), almost twofold, increase in doxorubicin amount in the tumor following USCTx. We also observed significant increases in doxorubicin in other organs ($p < 0.01$ for spleen, $p < 0.05$ for liver, heart, muscle and kidney) from USCTx versus control mice.

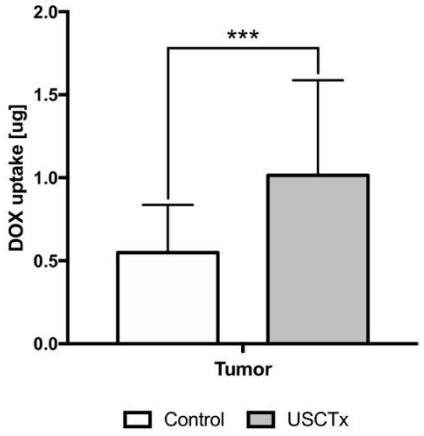

Fig. 5.7: DOX uptake in USCTx versus control mice.

Doxorubicin amount is presented in micrograms (per equivalent tissue homogenate mass). ***p<0.001.

A comparison of representative sections taken for DOX nuclear uptake is shown in **Fig. 5.8**. It can be observed that there is a higher accumulation of doxorubicin beyond tumor walls in USCTx versus control animals, as indicated by the greater amount of red fluorescent cell nuclei shown in **Fig. 5.8f** and **h** than in **Fig. 5.8b** and **d**.

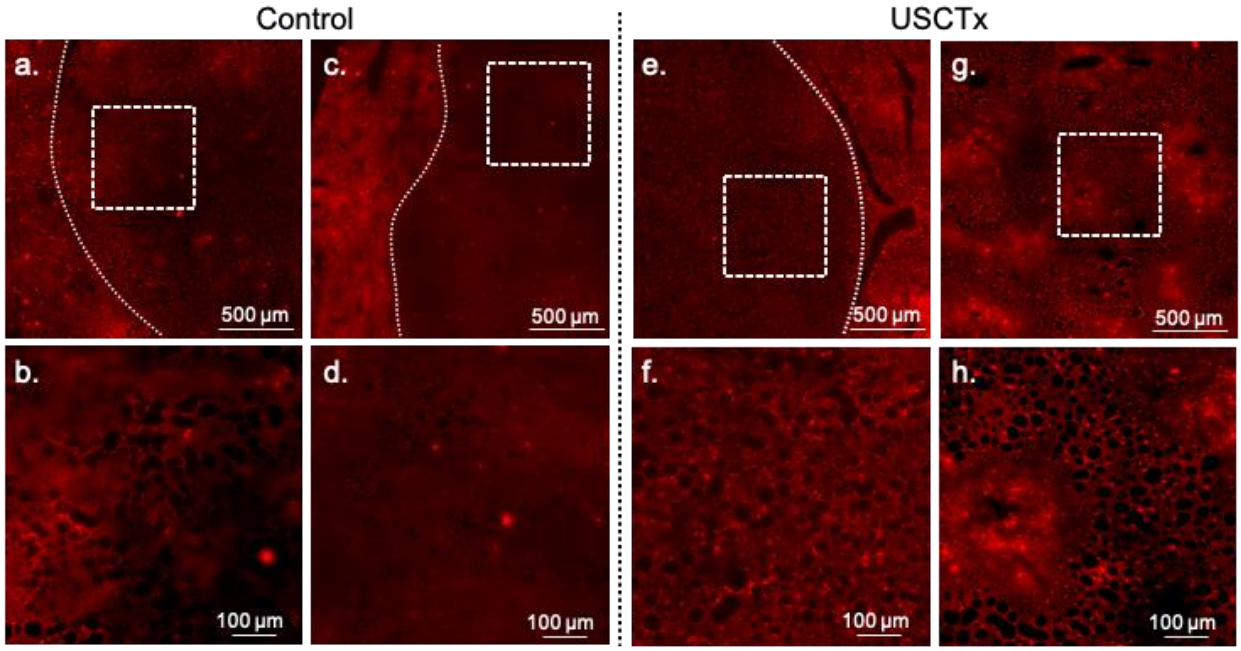

Fig. 5.8: Representative DOX fluorescent images.

Images from control animals in (a,b) and (c,d) and USCTx animals in (e,f) and (g,h). Each column represents a different animal. The top row (a,c,e,g) shows tumor morphology (tumor bounded with dashed line, or the entire image is the central part of the tumor) and the bottom row (b,d f,h) shows the same area at increased magnification. The USCTx animals have more DOX-positive nuclei than the control animals, as seen in (f) and (h) as compared to (b) and (d).

5.3.4 *Histologic examination*

CD31 images taken from non-tumor liver tissue and tumor tissue are shown in **Fig. 5.9a** and **b** and **Fig. 5.9c** and **d**, respectively. The vascular density of the tumors is much higher than the surrounding tissue. The capillaries in the tumors were also in general smaller in diameter than the non-tumor liver. No differences in microvascular density were observed between USCTx and control animals.

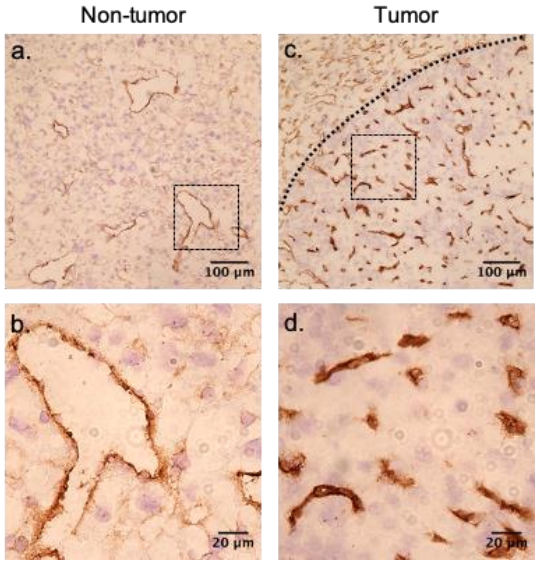

Fig. 5.9: CD31-stained slices from tumor and non-tumor liver.

(a,b) shows non-tumor tissue and (c,d) shows tumor tissue. The vessels in both tumors are much smaller in diameter and the overall vascular density is higher than in the non-tumor section.

Representative examples of H&E stained sections are shown in **Fig. 5.10**. Both non-tumor tissue and tumor tissue had some degree of steatosis. It can be observed that it was simple to segment tumorous tissue from non-tumorous tissue using anatomical morphology in **Fig. 5.10b**. No hemorrhaging or extravasated red blood cells were observed in any H&E stained slides in either USCTx or control animals (**Fig. 5.10c, d**).

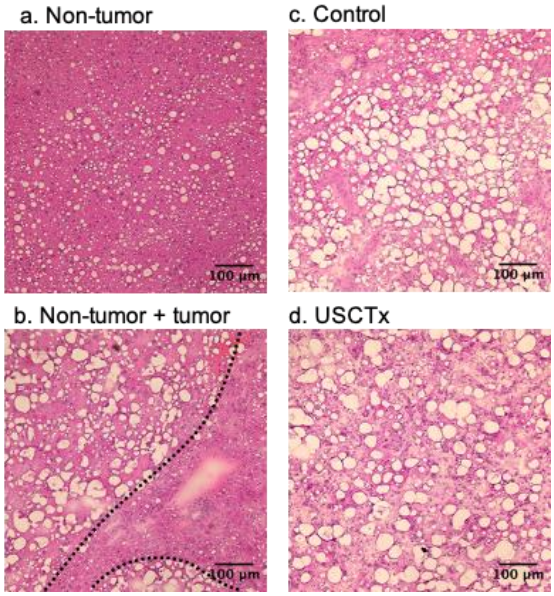

Fig. 5.10: Examples of H&E stained images from tumor and non-tumor liver.

(a) shows the boundary between non-tumor and tumor tissue (b) shows control tumorous tissue (c) and USCTx tumorous tissue (d). No tissue damage was observed in any slides.

5.4 DISCUSSION

The main goal of the present work was to investigate ultrasound cavitation-induced treatment (USCTx) of primary liver cancer while paying attention to the ability of the present methods to be easily translated to clinical practice. To this end, we used a genetically engineered mouse model that developed native liver cancer that could appropriately recapitulate human pathology and we performed all imaging and treatment with clinical ultrasound systems. Enhanced drug penetration and immediate tumor vascular shutdown were observed in animals treated with focused ultrasound and microbubbles compared to those receiving free drug. Using a diagnostic ultrasound device, clinical-grade microbubbles, and a clinically approved drug means that this technique could be adopted into clinical practice.

5.4.1 *Use of a diagnostic ultrasound device for ultrasound cavitation treatment*

To the best of our knowledge, this is the first study to optimize a clinical scanner and probe to produce the ultrasound conditions for cavitation treatment that are different from those of normal

imaging. We chose the S5-1 array for two reasons: it allows the use of a low frequency (1.6 MHz was the lowest available for this probe) suitable for cavitation therapies and it produces collimated beams to cover a large area, like novel phased array HIFU devices currently being investigated [28]–[30]. We chose to implement parameters that were consistent with other studies investigating cavitation-induced vascular disruption, and therefore the MI of 2 that was used was only slightly higher than the FDA limit of 1.9. It is worth noting, however, that our cycle lengths are slightly longer than would typically be used within these FDA constraints. Optimizing ultrasound treatment parameters in this regime requires changing aspects of the Doppler signal path, such as its depth (focus), sample volume size and range (number of cycles and PRF), and mechanical index (focal pressure). The highest sample volume achievable with the S5-1 without additional modification yields 32 cycles, but thermal index limitations on the probe means that the mechanical index at this setting is limited to 0.5. By accessing research settings on the system, we were able to increase the number of cycles and pressure, while simultaneously decreasing PRF and reduce the thermal load on the probe. While a higher number of cycles could be used, there is a tradeoff between output voltage, number of cycles, and PRF, due to concerns of transducer surface heating. That said, there is still a high degree of tunability that can be achieved within these constraints. Finally, although the S5-1 is technically also able to perform imaging, we chose to instead use a higher frequency linear probe for better image resolution in mice. However, when considering using this technique in clinical abdominal applications, S5-1 would be suitable to perform both the treatment and imaging and we would not need to use 2 scanners as we did here in this mouse study.

5.4.2 *Pten-null mice are an appropriate model for studying image-guided cavitation treatment*

In addition to using a diagnostic ultrasound device for treatment, we also chose to use a mouse model that could appropriately mimic human liver cancer. Despite previous reports showing efficacy in ultrasound-mediated vascular disruption with or without drug delivery [9], [10], [13], [31], there have been no studies using a physiologically relevant preclinical liver cancer model. However, one drawback to using this model is the substantial time to tumorigenesis (40 weeks in addition to breeding time). While subcutaneous or intramuscular tumor inoculations provide

quicker experimental timelines, it was important to study these phenomena in a system that more accurately represents the *in vivo* setting of liver cancer.

From H&E stained slides, large fat vacuoles can be seen due to the steatotic nature of the *Pten*-null phenotype. Steatosis is associated with an overall reduction in perfusion in the hepatic microcirculation, due to the enlargement of parenchymal cells from fat accumulation causing distortion of liver sinusoids [32]. This, in turn, can yield less efficient drug delivery [33]. In addition to steatosis, two forms of primary liver cancer, HCCs and ICCs, were observed in the livers of *Pten*-null mice. HCC accounts for 70% of diagnosed liver cancer cases and ICC accounts for 15% [34]. ICC often accompanies HCC during clinical diagnosis and generally has the same risk factors, including cirrhosis, hepatitis B/C, and non-alcoholic steatohepatitis [34]. Therefore, despite increasing the complexity of the model, the presence of both forms of primary liver cancer (HCC and ICC) along with steatohepatitis is not uncommon in disease progression in humans.

5.4.3 *Microbubble-mediated vascular shutdown*

We observed that microbubble cavitation at moderate ultrasound pressures between 2-3 MPa exhibits a high degree of anti-vascular action selectively within the tumors of mice. This was first seen qualitatively, in which it was observed that there was a clear reduction of contrast in the tumor post-USCTx that was not observed in healthy tissue. When this was analyzed quantitatively using TIC analysis, we found a significant increase in contrast RT and a significant decrease in PI in the tumor cores of USCTx mice. No differences in RT and PI were observed in non-tumor tissue of either control or USCTx treated mice, consistent with prior studies showing selectivity of cavitation treatment within the tumor [7], [9]. This selectivity is generally hypothesized to be a result of the fragile and atypical vascular structure in tumor neovessels, including irregular vessel diameters and branching patterns [8], [35]. Prior studies have shown these highly aberrant vessels are more susceptible to cavitation-induced damage, including endothelial cell damage and thrombosis [7], [36]. Differences in vascular morphology were confirmed through CD31 staining of endothelial cells; as shown in **Fig. 5.9**, the vascular density of tumor tissue was indeed higher than in non-tumorous tissue. Moreover, the vessel size was much smaller in the tumors, averaging about 10-20 μm, as opposed to the non-tumor vessels, which had diameters in the order of hundreds of microns. Given that microbubbles are within the 1-10 μm range, it makes sense that

cavitation within these smaller diameter vessels might have a bigger impact on blood flow. However, no observable differences in CD31 expression were seen in USCTx versus control animals in both tumorous and non-tumorous tissue, nor was any damage observed in any H&E stained slides, indicating that no acute endothelial damage occurred. However, this may be due to the fact that microvascular density changes are generally observed after a latency period of 24 hours after therapy [7]. Alternatively, the exact mechanism may be due to other physiological changes (such as modulating tumor interstitial pressure), and the lack of gross morphological damage may be an indicator of the overall safety of this therapy.

5.4.4 *Enhanced drug penetration in ultrasound cavitation treated tumors*

We found that there was a significant, almost twofold, increase in doxorubicin accumulation in the tumors of USCTx mice versus control mice. When other organs were considered, however, we also observed significant increases. This might be due to the fact that we used a broad sound beam and, though we tried to minimize sound reflections through the use of an attenuating pad, our setup may still have allowed for other organs to have been affected. This could be easily avoided in clinical scenarios by image guidance and beamforming approaches for targeting of the therapeutic ultrasound field to be strictly within the tumoral area. Indeed, the size of the S5-1 makes it more optimized for targeting in human liver HCCs rather than in mice. The quantitative observations were further confirmed using qualitative fluorescence imaging of doxorubicin presence in serial sections of frozen tissue. It was observed that there was on average more penetration of doxorubicin deeper into the tumors of USCTx versus control animals. Attaining high tumor volumes usually comes at the expense of high dosages, which can lead to cardiotoxicity among other dangerous side effects [37]. Therefore, achieving higher doxorubicin accumulation in the tumor with the same injected dose is of high value, and this technique could certainly be implemented with other current drugs like sorafenib [38] or even nucleic acids [39], [40].

There is some discrepancy between the observed reduction in perfusion (and therefore reduction in blood flow) and contradictory enhanced drug delivery. One possible explanation for this is that the enhanced permeability and retention (EPR) effect seen in many highly angiogenic tumors can result in a high interstitial fluid pressure that can compromise drug delivery [35]. One proposed mechanism of how ultrasound and microbubbles increase drug penetration in tumors is that

cavitation activity actually temporarily alleviates the tumor interstitial fluid pressure, allowing for enhanced drug diffusion [41]. Most likely is that the two aspects of USCTx, drug penetration and anti-vascular action, work synergistically to target the outer rim and core of the tumor, respectively [9]. However, a longer-term study would be required to confirm this hypothesis.

5.4.5 *Limitations*

The purpose of this study was to investigate the feasibility of performing ultrasound-mediated cavitation treatment *in vivo* using a clinical ultrasound scanner. That being said, there are still many interesting mechanistic questions that were beyond the scope of that goal. Future work will be focused on exploring the exact physiological mechanism and time duration of vascular disruption in addition to long-term survival. However, the acute nature of these experiments allowed us to see immediate tissue morphology and drug accumulation both histologically and quantitatively as a result of USCTx. Additionally, we focused only on one set of ultrasound parameters. We specifically selected parameters based on previous work from our lab; 200 cycles and 50 Hz PRF to maximize cavitation activity and minimize microbubble motion [20], [21] and 2-3 MPa for maximum bubble response [42]. These parameters remain consistent with published literature [7], [9]; however, more parameter optimization may be necessary to study the underlying physical and physiological mechanisms of USCTx and would be simple to perform with the S5-1. Finally, this animal model represents a rather specific form of liver cancer that develops from a single genetic mutation. Unsurprisingly, the typical pathogenesis of HCC is far more complex, often a result of repeated stress on the liver due to chronic diseases such as Hepatitis B/C and alcoholic cirrhosis causing eventual DNA damage. Yet, HCC prevalence rates are rising in Western countries, which is theorized to be a result of an increase in obesity and obesity-related illnesses, such as diabetes, which cause hepatic steatosis and eventually liver cancer [43]. In this case, the *Pten*-null mouse model may be considered a reasonable model for observing macroscopic perfusion and drug delivery in cases in which cancer develops in the liver in the presence of steatosis.

5.5 CONCLUSION

A diagnostic ultrasound scanner was converted into a device capable of performing ultrasound cavitation treatment by reprogramming the transmit sequence of the S5-1 probe in a hybrid PW Doppler mode. The *Pten*-null mouse model used in these studies exhibited steatosis in addition to

HCC and ICC tumors, consistent with some types of human liver cancer pathogenesis. We observed that there were significant and immediate perfusion changes following ultrasound cavitation treatment with a commercial scanner and microbubbles. This effect was specific to the tumor, implying an inherent vulnerability in the tumor microvasculature that was not seen in surrounding tissue. Furthermore, it was shown that there was a statistically significant increase of doxorubicin in tumors in treated versus control animals. We did not observe any gross morphological damage, nor any differences in the microvasculature of USCTx treated tumors. The combination of selective tumor vascular disruption and peripheral enhanced drug penetration may play a synergistic role in successful cancer treatment.

5.6 ACKNOWLEDGEMENTS

We would like to also thank the UW Histology and Imaging Core for providing antibody staining and histology services, the Woodrow lab at UW for use of their fluorescence plate reader, and the Pozzo lab at UW for use of their centrifuge.

5.7 REFERENCES

[1] H. B. El-Serag and K. L. Rudolph, "Hepatocellular carcinoma: epidemiology and molecular carcinogenesis.," *Gastroenterology*, vol. 132, no. 7, pp. 2557–76, Jun. 2007.

[2] G. B. of D. L. C. Global Burden of Disease Liver Cancer Collaboration *et al.*, "The Burden of Primary Liver Cancer and Underlying Etiologies From 1990 to 2015 at the Global, Regional, and National Level: Results From the Global Burden of Disease Study 2015.," *JAMA Oncol.*, vol. 3, no. 12, pp. 1683–1691, 2017.

[3] M. N. Mavros, K. P. Economopoulos, V. G. Alexiou, and T. M. Pawlik, "Treatment and prognosis for patients with intrahepatic cholangiocarcinoma: Systematic review and meta-analysis," *JAMA Surg.*, vol. 149, no. 6, pp. 565–574, 2014.

[4] W. Liang, Y. Ni, and F. Chen, "Tumor resistance to vascular disrupting agents: Mechanisms, imaging, and solutions," *Oncotarget*, vol. 7, no. 13, pp. 15444–15459, Mar. 2016.

[5] K. Liu *et al.*, "Targeting the vasculature in hepatocellular carcinoma treatment: Starving versus normalizing blood supply.," *Clin. Transl. Gastroenterol.*, vol. 8, no. 6, p. e98, Jun. 2017.

[6] J. H. Gill, K. L. Rockley, C. De Santis, and A. K. Mohamed, "Vascular Disrupting Agents in cancer treatment: Cardiovascular toxicity and implications for co-administration with other cancer chemotherapeutics," *Pharmacol. Ther.*, vol. 202, pp. 18–31, Oct. 2019.

[7] J. Wang *et al.*, "Selective depletion of tumor neovasculature by microbubble destruction with appropriate ultrasound pressure," *Int. J. Cancer*, vol. 137, no. 10, pp. 2478–2491, Nov. 2015.

[8] D. Fukumura and R. K. Jain, “Tumor microvasculature and microenvironment: Targets for anti-angiogenesis and normalization,” *Microvasc. Res.*, vol. 74, no. 2–3, pp. 72–84, Sep. 2007.
[9] D. E. Goertz *et al.*, “Antitumor Effects of Combining Docetaxel (Taxotere) with the Antivascular Action of Ultrasound Stimulated Microbubbles,” *PLoS One*, vol. 7, no. 12, p. e52307, Dec. 2012.
[10] Z. Liu *et al.*, “Disruption of tumor neovasculature by microbubble enhanced ultrasound: A potential new physical therapy of anti-angiogenesis,” *Ultrasound Med. Biol.*, vol. 38, no. 2, pp. 253–261, Feb. 2012.
[11] R. K. Jain, “Normalization of Tumor Vasculature: An Emerging Concept in Antiangiogenic Therapy,” *Science (80-.).*, vol. 307, no. 5706, pp. 58–62, Jan. 2005.
[12] D. W. Siemann, E. Mercer, S. Lepler, and A. M. Rojiani, “Vascular targeting agents enhance chemotherapeutic agent activities in solid tumor therapy,” *Int. J. Cancer*, vol. 99, no. 1, pp. 1–6, May 2002.
[13] J. C. D’Souza *et al.*, “Microbubble-enhanced ultrasound for the antivascular treatment and monitoring of hepatocellular carcinoma,” *Nanotheranostics*, vol. 3, no. 4, pp. 331–341, 2019.
[14] Y.-J. Ho, T.-C. Wang, C.-H. Fan, and C.-K. Yeh, “Spatially Uniform Tumor Treatment and Drug Penetration by Regulating Ultrasound with Microbubbles,” *ACS Appl. Mater. Interfaces*, vol. 10, no. 21, p. acsami.8b05508, May 2018.
[15] G. Dimcevski *et al.*, “A human clinical trial using ultrasound and microbubbles to enhance gemcitabine treatment of inoperable pancreatic cancer,” *J. Control. Release*, vol. 243, pp. 172–181, Dec. 2016.
[16] O. R. Mason *et al.*, “Augmentation of Tissue Perfusion in Patients With Peripheral Artery Disease Using Microbubble Cavitation,” *JACC Cardiovasc. Imaging*, vol. 13, no. 3, pp. 641–651, Mar. 2020.
[17] Y. Horie *et al.*, “Hepatocyte-specific Pten deficiency results in steatohepatitis and hepatocellular carcinomas.,” *J. Clin. Invest.*, vol. 113, no. 12, pp. 1774–83, Jun. 2004.
[18] H. L. Kenerson, M. M. Yeh, and R. S. Yeung, “Tuberous Sclerosis Complex-1 Deficiency Attenuates Diet-Induced Hepatic Lipid Accumulation,” *PLoS One*, vol. 6, no. 3, p. e18075, Mar. 2011.
[19] T. Li *et al.*, “Pulsed high-intensity focused ultrasound enhances delivery of doxorubicin in a preclinical model of pancreatic cancer,” *Cancer Res.*, vol. 75, no. 18, pp. 3738–3746, Sep. 2015.
[20] S. Keller, M. Bruce, and M. A. Averkiou, “Ultrasound Imaging of Microbubble Activity during Sonoporation Pulse Sequences,” *Ultrasound Med. Biol.*, vol. 45, no. 3, 2019.
[21] C. Mannaris and M. A. Averkiou, “Investigation of Microbubble Response to Long Pulses Used in Ultrasound-Enhanced Drug Delivery,” *Ultrasound Med. Biol.*, vol. 38, no. 4, pp. 681–691, Apr. 2012.
[22] C. P. Keravnou, I. De Cock, I. Lentacker, M. L. Izamis, and M. A. Averkiou, “Microvascular Injury and Perfusion Changes Induced by Ultrasound and Microbubbles in a Machine-Perfused Pig Liver,” *Ultrasound Med. Biol.*, vol. 42, no. 11, pp. 2676–2686, 2016.
[23] M. A. Averkiou, M. F. Bruce, J. E. Powers, P. S. Sheeran, and P. N. Burns, *Imaging Methods for Ultrasound Contrast Agents*, vol. 46, no. 3. 2020, pp. 498–517.
[24] C. F. Dietrich, M. A. Averkiou, J.-M. M. Correas, N. Lassau, E. Leen, and F. Piscaglia,

"An EFSUMB introduction into dynamic contrast-enhanced ultrasound (DCE-US) for quantification of tumour perfusion," *Ultraschall der Medizin*, vol. 33, no. 4, pp. 344–351, Aug. 2012.
[25] C. Strouthos, M. Lampaskis, V. Sboros, A. Mcneilly, and M. Averkiou, "Indicator dilution models for the quantification of microvascular blood flow with bolus administration of ultrasound contrast agents," *IEEE Trans. Ultrason. Ferroelectr. Freq. Control*, vol. 57, no. 6, pp. 1296–1310, Jun. 2010.
[26] K. M. Laginha, S. Verwoert, G. J. R. Charrois, and T. M. Allen, "Determination of doxorubicin levels in whole tumor and tumor nuclei in murine breast cancer tumors," *Clin. Cancer Res.*, vol. 11, no. 19 I, pp. 6944–6949, Nov. 2005.
[27] C. P. Keravnou, M. L. Izamis, and M. A. Averkiou, "Method for estimating the acoustic pressure in tissues using low-amplitude measurements in water," *Ultrasound Med. Biol.*, vol. 41, no. 11, pp. 3001–3012, Nov. 2015.
[28] J. W. Hand, A. Shaw, N. Sadhoo, S. Rajagopal, R. J. Dickinson, and L. R. Gavrilov, "A random phased array device for delivery of high intensity focused ultrasound," *Phys. Med. Biol.*, vol. 54, no. 19, pp. 5675–5693, Oct. 2009.
[29] M. Wang and Y. Zhou, "Simulation of non-linear acoustic field and thermal pattern of phased-array high-intensity focused ultrasound (HIFU)," *Int. J. Hyperth.*, vol. 32, no. 5, pp. 569–582, Jul. 2016.
[30] P. Aslani *et al.*, "Thermal therapy with a fully electronically steerable HIFU phased array using ultrasound guidance and local harmonic motion monitoring," *IEEE Trans. Biomed. Eng.*, pp. 1–1, 2019.
[31] A. K. W. Wood, S. Ansaloni, L. S. Ziemer, W. M.-F. Lee, M. D. Feldman, and C. M. Sehgal, "The antivascular action of physiotherapy ultrasound on murine tumors.," *Ultrasound Med. Biol.*, vol. 31, no. 10, pp. 1403–10, Oct. 2005.
[32] G. C. Farrell, N. C. Teoh, and R. S. Mccuskey, "Hepatic Microcirculation in Fatty Liver Disease," *Anat. Rec. Adv. Integr. Anat. Evol. Biol.*, vol. 291, no. 6, pp. 684–692, Jun. 2008.
[33] Y. ITO, E. R. ABRIL, N. W. BETHEA, M. K. MCCUSKEY, and R. S. MCCUSKEY, "Dietary Steatotic Liver Attenuates Acetaminophen Hepatotoxicity in Mice," *Microcirculation*, vol. 13, no. 1, pp. 19–27, Jan. 2006.
[34] N. N. Massarweh and H. B. El-Serag, "Epidemiology of Hepatocellular Carcinoma and Intrahepatic Cholangiocarcinoma," *Cancer Control*, vol. 24, no. 3. SAGE Publications Ltd, 06-Sep-2017.
[35] D. Semela and J. F. Dufour, "Angiogenesis and hepatocellular carcinoma," *Journal of Hepatology*, vol. 41, no. 5. pp. 864–880, Nov-2004.
[36] J. H. Hwang, A. A. Brayman, M. A. Reidy, T. J. Matula, M. B. Kimmey, and L. A. Crum, "Vascular effects induced by combined 1-MHz ultrasound and microbubble contrast agent treatments in vivo," *Ultrasound Med. Biol.*, vol. 31, no. 4, pp. 553–564, Apr. 2005.
[37] P. K. Singal and N. Iliskovic, "Doxorubicin-Induced Cardiomyopathy," *N. Engl. J. Med.*, vol. 339, no. 13, pp. 900–905, Sep. 1998.
[38] Y. Tan *et al.*, "Ultrasound-triggered nanodroplets for targeted Co-delivery of sorafenib/doxorubicin for hepatocellular carcinoma therapy," *J. Biomed. Nanotechnol.*, vol. 15, no. 9, pp. 1881–1896, 2019.
[39] T. Di Ianni *et al.*, "Ultrasound/microbubble-mediated targeted delivery of anticancer microRNA-loaded nanoparticles to deep tissues in pigs," *J. Control. Release*, vol. 309, pp.

1–10, Sep. 2019.
[40] L. Scarabel *et al.*, “Strategies to optimize siRNA delivery to hepatocellular carcinoma cells,” *Expert Opin. Drug Deliv.*, vol. 14, no. 6, pp. 797–810, Jun. 2017.
[41] Q. Zhang *et al.*, “Effect of ultrasound combined with microbubble therapy on interstitial fluid pressure and VX2 tumor structure in rabbit,” *Front. Pharmacol.*, vol. 10, no. JUN, 2019.
[42] C. Keravnou, C. Mannaris, and M. Averkiou, “Accurate measurement of microbubble response to ultrasound with a diagnostic ultrasound scanner,” *IEEE Trans. Ultrason. Ferroelectr. Freq. Control*, vol. 62, no. 1, pp. 176–184, Jan. 2015.
[43] B. Q. Starley, C. J. Calcagno, and S. A. Harrison, “Nonalcoholic fatty liver disease and hepatocellular carcinoma: A weighty connection,” *Hepatology*, vol. 51, no. 5, pp. 1820–1832, May 2010.

Chapter 6. SAFETY OF IMAGE-GUIDED TREATMENT OF THE LIVER WITH ULTRASOUND AND MICROBUBBLES IN AN *IN VIVO* PORCINE MODEL[5]

Sara B. Keller, Yak-Nam Wang, Stephanie Totten, Raymond S. Yeung, Michalakis A. Averkiou

Abstract

Ultrasound and microbubbles are useful for both diagnostic imaging and targeted drug delivery, making them ideal conduits for theranostic interventions. Recent reports have indicated preclinical success of microbubble cavitation for enhancement of chemotherapy in abdominal tumors; however, there have been limited studies and variable efficacy in clinical implementation of this technique. This is likely because in contrast to the high pressures and long cycle lengths seen in successful preclinical work, current clinical implementation of microbubble cavitation for drug delivery generally involves low acoustic pressures and short cycle lengths to fit within clinical guidelines. In order to translate the preclinical parameter space to clinical adoption, a relevant safety study in a healthy large animal is required. Therefore, the purpose of this work was to evaluate the safety of UltraSound Cavitation Treatment (USCTx) in a healthy porcine model using a modified Philips EPIQ with S5-1 as the focused source. We performed USCTx on eight healthy pigs and monitored health over the course of one week. We then performed an acute study of USCTx in order to evaluate immediate tissue damage. Contrast enhanced ultrasound exams were performed before and after each treatment to investigate perfusion changes within the treated areas and blood and urine were evaluated for liver damage biomarkers. We show through quantitative analysis of contrast enhanced ultrasound data, blood and urine analysis, and histology that this technique and the parameter space considered is safe within the timeframe evaluated. By confirming safety using a clinical-grade ultrasound scanner and contrast agent, USCTx could be easily translated into clinical trials for improvement of chemotherapy delivery. This represents the

[5] *Reprinted with permission from Keller, SB, et al. "Safety of image-guided treatment of the liver with ultrasound and microbubbles in an in vivo porcine model". Ultrasound Med. Biol. 2021. Copyright 2021 Elsevier B.V.*

first safety study assessing the bioeffects of microbubble cavitation from relevant ultrasound parameters in a large animal model.

6.1 INTRODUCTION

Ultrasound-mediated drug delivery with microbubbles has the potential to treat a wide variety of diseases, from cancer [1] to stroke [2]. In the presence of ultrasound, microbubbles oscillate nonlinearly. The resultant microbubble echoes can provide ultrasound signal enhancement while microbubble oscillations can cause microscale mechanical forces for targeted drug delivery [3]. Since microbubbles are able to be both visualized and activated for treatment procedures, they are suitable for performing image-guided interventions.

One of the most promising applications of ultrasound and microbubbles is for enhancing delivery of chemotherapeutics. Recent work from our group [4] and others [1], [5], [6] have shown that ultrasound and microbubbles have the ability to enhance drug penetration throughout tumors, ordinarily restricted due to inefficient blood flow and high tumor interstitial pressure [7]. It is hypothesized that ultrasound causes fluid streaming (both microstreaming and bulk flow) that can enhance the convective transport of small molecule drugs [6] and can also potentially alleviate tumor interstitial pressure [8]. Furthermore, we have shown that these outcomes are possible even when using a modified diagnostic ultrasound device to produce the necessary ultrasound conditions for therapy [4]. The use of microbubble cavitation for vascular disruption and drug penetration is defined in the present study as Ultrasound Cavitation Treatment (USCTx).

Despite promising studies both *in vitro* and *in vivo*, USCTx is still not approved for clinical use. Indeed, one of the few studies that has been published on the clinical outcomes of using ultrasound and microbubbles for cancer treatment was a small pilot study performed on ten patients with pancreatic cancer that utilized normal imaging modes to enhance gemcitabine delivery [9]. Although it suggested the potential clinical efficacy of this technique, more and larger clinical studies are necessary. Furthermore, the ultrasound parameters used in that study were limited to the ultrasound parameters available for imaging in order to comply with safety requirements. Another study from Huang et al. retrospectively evaluated survival outcomes of patients treated with focused ultrasound and SonoVue versus focused ultrasound and transarterial

chemoembolization (TACE) to treat hepatocellular carcinoma [10]. The authors did not find any significant differences between the two groups; however, the study was limited by the fact that it was a retrospective analysis and therefore utilized inconsistent ultrasound conditions. Finally, Eisenbrey, et al. combined microbubble destruction with transarterial radioembolization in a first-in-human clinical trial for treating hepatocellular carcinoma and observed preliminary results suggesting both improved tumor response and safety [11]. Although encouraging, that study also utilized standard imaging modes with moderate pressures and short cycle lengths, again possibly due to clinical limitations, despite the fact that longer pulse durations have been shown to have higher therapeutic efficacy [12]. None of the above-mentioned studies were true safety studies, in that histological analyses could not be performed, maximally effective parameters were not used, and most importantly, the studies were not performed on healthy individuals. It can be difficult to form meaningful conclusions about safety and efficacy of new clinical techniques on very sick patients.

A necessary requirement for making a new technique and device available for use in clinical trials is a relevant safety evaluation in a large animal model. Although there is a wide literature base evaluating the safety of blood-brain barrier opening, performed previously on non-human primates [13], [14] and humans [15], these studies are not necessarily applicable for tumors outside of the brain. In addition, the device used for the clinical study, the ExAblate Neuro (InSightec, Tirat Carmel, Israel) system has already been through the process of clinical safety evaluation since it is approved for the surgical treatment of essential tremors. While microbubble destruction as a chemotherapy sensitizer for abdominal applications is currently being pursued in the clinic both in the United States and around the world, the parameter space is often much different than what is seen in preclinical studies, which could explain some of the variable clinical results. For example, Di Ianni, et al. evaluated delivery of miRNA into the livers of healthy pigs using ultrasound and systemic injection of microbubbles with focal pressures up to 5.3 MPa, far exceeding the clinically allowable ultrasound dose, although they only evaluated safety 24 hours after ultrasound therapy [16]. Additionally, many studies in mice show efficacy with focal pressures of 3-5 MPa [17], [18]. This is in contrast to the MIs of 0.2 and 1.13 used clinically by Dimcevski et al. and Eisenbrey et al., respectively [9], [11].

The goal of this work was to evaluate the safety of USCTx on a healthy porcine model, using conditions previously proven effective at enhancing drug penetration in mice with a modified clinical scanner operating outside of the normal FDA limits and accounting for depth-dependent attenuation. To the best of our knowledge, this represents the first safety study assessing the bioeffects of ultrasound scanner-induced microbubble cavitation in the healthy liver of a large animal. Unlike the work from Dimcevski et al. and Eisenbrey et al. in which approved imaging modes were adapted for therapy [9], [11], the parameter space investigated in the present study would not be currently allowed for use in clinical trials for cancer therapy without a safety study. We performed a 7-day survival study on 8 female pigs while delivering the ultrasound conditions for USCTx with a Philips EPIQ with S5-1 phased array probe. The ultrasound conditions utilize both higher acoustic pressures and longer pulse durations than normally available on the clinical scanner for imaging [4]. We additionally evaluated immediate histological damage due to USCTx in an acute study. We implemented similar USCTx parameters as in our previous work [4] and show through quantitative analysis of contrast enhanced ultrasound data, blood and urine analysis, and histology, that this technique is safe within the timeframe evaluated. The use of a clinical-grade ultrasound scanner and microbubble contrast agent will support clinical trials in order to facilitate translation.

6.2 MATERIALS AND METHODS

6.2.1 *Animal model*

All animal work was conducted in accordance with national guidelines and was approved by the Institutional Animal Care and Use Committee (IACUC) at the University of Washington, Seattle. The animals were housed at a facility at the University of Washington that is fully accredited by Association for Assessment and Accreditation of Laboratory Animal Care International. The animals were cared for by a full-time veterinary staff. Eight 3-5-month-old healthy female pigs weighing between 45 and 55 kg were enrolled in the study. They were acclimatized for 1 week prior to the beginning of the study. Food was restricted 12 hours prior to administering anesthesia. Due to known scavenging of injected particles by pulmonary macrophages in pigs [19], animals were premedicated 24 and 12 hours before the beginning of the study with a combination of 3 mg/kg aspirin, and 3 mg/kg indomethacin, given orally [20], [21]. Two pigs received an additional

3.5 mg/kg of sodium salicylate administered intravenously 5 minutes prior to injection of contrast for treatment [22] as an added premedication dose when microbubble supply was still insufficient (confirmed by pre-treatment contrast imaging). Pigs were anesthetized with 4 mg/kg Telazol administered intramuscularly and then maintained under 2-5% isoflurane during the duration of treatment. While under anesthesia, heart rate, ECG, oxygen saturation, ventilation rate, and body temperature were continually monitored for premature ventricular contractions (PVCs), anaphylaxis, and other abnormalities that would require ending the treatment. Each animal underwent two separate days of USCTx, as shown in **Fig. 6.1**, described more in detail later.

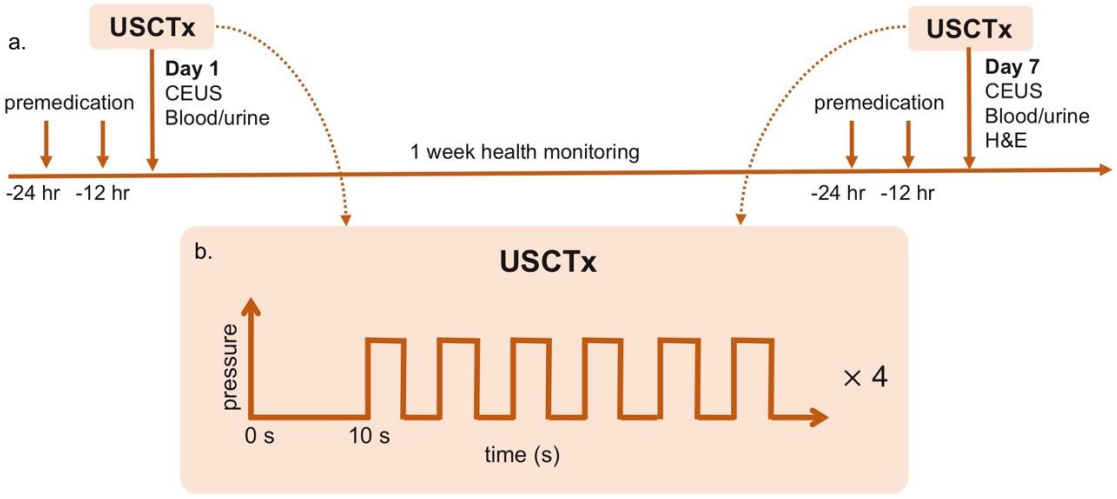

Fig. 6.1: Overview of experimental protocol.

(a) shows the weeklong experiment, with treatment on Days 1 and 7. CEUS, blood analysis, and urinalysis were readouts for the longitudinal study performed on Day 1, and H&E staining was the readout for the acute study on Day 7. Aspirin and indomethacin were given 24 hr and 12 hr prior to injection of contrast. (b) shows overview of UltraSound Cavitation Treatment (USCTx), in which ultrasound was applied at peak microbubble enhancement (10 s), and was "on" for a total of 30 s. This procedure was applied 4 times on Day 1 and 7.

6.2.2 *Ultrasound parameters for USCTx on the Philips EPIQ*

Focused ultrasound beams for USCTx were designed and implemented on a Philips EPIQ scanner (Philips Healthcare, Bothell, WA, USA) and S5-1 phased array operating in a modified PW Doppler mode as described previously [4]. Briefly, the focal length was selected to be 10 cm and the full aperture of the probe was utilized. The center frequency was 1.6 MHz. The pulse length

was increased to 200 cycles (which is substantially larger than what it is currently used in imaging) and the pulse repetition frequency (PRF) was reduced to 50 Hz. We matched the parameters in our previous murine efficacy study by increasing the transmit pressure of the S5-1 in order to account for added depth-dependent tissue attenuation, verified with focal hydrophone pressure measurements and attenuation adjustments. We additionally measured the spatial extent of the sound field in the azimuthal and elevation central planes using a 0.4 mm membrane hydrophone (UT1604, Precision Acoustics Ltd., Dorchester, UK), acquired using a DPO7054C Oscilloscope (Tektronix, Inc., Beaverton, OR, USA), and analyzed in MATLAB (The MathWorks, Inc., Natick, MA, USA).

6.2.3 *Contrast agent*

SonoVue (Bracco Suisse SA, Geneva, Switzerland), marketed in the United States as Lumason, was resuspended according to the manufacturer's instructions. Microbubble concentration was measured with a Multisizer 3 (Beckman Coulter, Brea, CA, USA), and found to be between 1-5×10^8 microbubbles/mL. Each microbubble injection for contrast enhanced ultrasound (CEUS) examination was 1.2 mL and each microbubble injection for USCTx was 2.4 mL, as these volumes provided appropriate contrast, as determined with preliminary contrast injections. A total of six injections were performed over the treatment timeline (two for CEUS imaging, and four for USCTx), and therefore 2 vials of SonoVue were used: half a vial for CEUS imaging and a vial and a half for USCTx. The SonoVue dosage used in this study exceeded the maximum clinical dose of 1 vial in order to qualitatively compensate for limited systemic delivery of injected particles, which usually manifested on CEUS exams as hyperenhancement in the lungs and reduced enhancement in systemic organs. This is in contrast to clinical studies in humans, in which the liver usually receives most of the injected dose. However, there were no adverse effects observed due to the dosage used.

6.2.4 *Ultrasound Cavitation Treatment (USCTx) procedure*

USCTx was performed as described previously [4], after contrast was administered via ear vein catheter. Briefly, pre-treatment CEUS exams were performed, in order to evaluate an appropriate acoustic window for treatment and bolus kinetics. The abdominal clinical setting of the C5-1 probe on the EPIQ was chosen for CEUS imaging. A non-destructive MI of 0.07 was utilized in contrast

side-by-side mode where the left image displays the contrast image and the right image displays the B-mode tissue image. The rest of the parameters were: 50 dB compression, 66% and 46% gain for contrast and tissue respectively, 12 cm depth, 10 cm focus, and the persistence was turned off. Four total USCTx treatments were performed, in which each individual treatment consisted of a 2.4 mL bolus injection of SonoVue followed by focused ultrasound. Focused ultrasound started 10 s after injection of SonoVue, in order to interrogate microbubbles at peak contrast enhancement. We chose 10 s instead of the 30 s used in our previous mouse study due to differences in time to peak contrast enhancement observed through CEUS imaging. Focused ultrasound was applied for 5 s "on" and 5 s "off", to allow for microbubble reperfusion (as confirmed with simultaneous CEUS imaging), with a total "on" time of 30 s (**Fig. 6.1b**). Then, post-treatment CEUS exams were performed to evaluate any immediate change in perfusion.

6.2.5 *Longitudinal study*

All pigs were anesthetized and placed supine (**Fig. 6.2a**). The abdomen of the pig was depilated and an ear vein catheter and bladder catheter were inserted. Both the ear vein catheter and bladder catheter remained inserted in the animal throughout the duration of the experiment and removed prior to revival of the animal. Blood and urine samples were taken prior to USCTx to evaluate blood liver enzymes including alkaline phosphatase (ALP), aspartate aminotransferase (AST), alanine transamerase (ALT) and γ-glutamyl transferase (GGT), as well as presence of proteins in urine at baseline. USCTx was then performed on all animals, in addition to pre- and post-USCTx CEUS exams. Specific anatomical landmarks seen through imaging were noted to ensure that this area was not treated during the acute study. Afterwards, blood and urine samples were taken again, at which point the catheters were removed. The pigs were then revived and returned to their housing. The pigs were monitored daily for food intake, urine and feces output, ambulation ability, and signs of lethargy over the following week by both study personnel and animal husbandry staff. On Day 7, the pigs were anesthetized, and the ear vein catheter and bladder catheter were inserted again for retrieval of blood and urine samples. A CEUS exam was performed to evaluate any changes in perfusion in the treated area. This concluded the longitudinal safety study. All blood and urine samples were sent to IDEXX BioAnalytics as part of their complete blood chemistry

panel (in addition to GGT) and urine analysis package (IDEXX Laboratories, Inc., Westbrook, ME, USA).

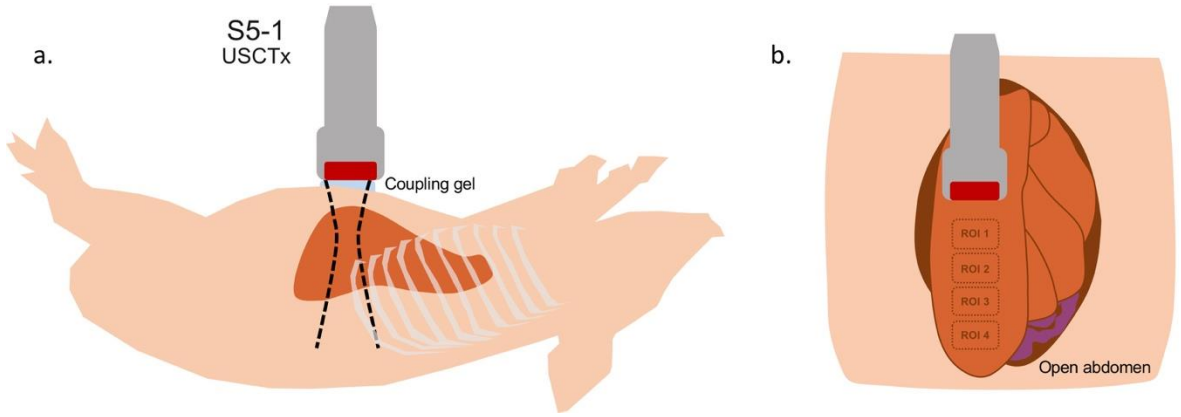

Fig. 6.2: Overview of experimental setup for the longitudinal and acute studies.

The EPIQ with S5-1 phased array probe was used as the focused source of ultrasound. The C5-1 was used for abdominal CEUS imaging pre- and post- USCTx. An acoustic window below the ribs was chosen, in order to minimize any bone-induced reverberations and attenuation (a). For the acute study in (b), the abdomen was surgically opened, and one lobe of the liver was gently removed and exposed. Four treatment areas (ROIs 1-4) were chosen and USCTx was performed at all locations.

6.2.6 *Acute study*

To evaluate immediate damage due to USCTx, on Day 7, the abdomens of the pigs were surgically opened, and the liver was exposed (**Fig. 6.2b**). USCTx was performed as described previously to four separate locations directly on a lobe of the liver that was not treated on Day 1. The same settings were used as in the longitudinal study. The distance in millimeters between the treated areas and the borders of the liver were noted for correct removal of tissue samples for each ROI. After treatment, the animals were euthanized and samples from each of the ROIs was collected and embedded in optimal cutting temperature (OCT) compound for histopathology.

6.2.7 *Quantitative CEUS evaluation*

Time-intensity curve analysis was performed on all pre- and post-USCTx (both Day 1 and Day 7) contrast loops to evaluate changes in perfusion [23] using a custom DICOM reader developed in our lab using MATLAB (The Mathworks, Inc., Natick, MA, USA). Regions of interest (ROIs)

were drawn as freeform polygons and chosen to encompass the entire treatment area. Contrast agent rise time (RT), which is inversely proportional to blood flow [24], was measured for all time points (before and after treatment on Day 1, and again on Day 7). Rise time was calculated manually as the peak time of the bolus intensity minus the start time and was calculated from the log-compressed image data. Although it is customary to use linearized data [23], [25], analysis of time parameters from the log-compressed data is sufficient here since we were not performing curve-fitting. Rise time was compared between pre-USCTx and both Day 1 and 7 post-USCTx using a paired Student's *t*-test.

6.2.8 *Preparation of histological samples*

Sections of 6 μm thickness were taken from OCT-embedded liver samples from treatment and control ROIs using a Leica CM 1950 Cryostat (Leica Biosystems, Wetzlar, Germany) and rapidly fixed in 95% ETOH. Four sections were taken at three locations throughout each tissue sample. The sections were then stained with hematoxylin and eosin (H&E) for anatomical morphology and gross morphological damage. Sections were evaluated by an expert evaluator (RSY) blinded to the treatment conditions.

6.3 RESULTS

6.3.1 *Measured acoustic sound field from clinical device*

Fig. 6.3 shows the measured sound field amplitude from the S5-1 in the central azimuth (**a**) and elevation (**b**) planes that was used for these studies. These measurements were taken in water; in order to estimate the in situ pressure, we must account for tissue attenuation, approximated to be about 0.5 dB/cm/MHz [26]. This corresponds to a loss of 4 dB, assuming 5 cm depth and 1.6 MHz frequency. Therefore, the in situ focal pressure at 5 cm would be about 2.2 MPa, given that the focal pressure in water was 3.5 MPa at this depth. It should be noted that standard clinical scanners approximate tissue attenuation to be 0.3 dB/cm/MHz, in which case, the "clinical pressure" would be 2.6 MPa. For the acute study, the central region of the liver was at approximately 3 cm in depth, which would correspond to a derated pressure of 2.3 MPa, given that the pressure measured in water at this depth was 3 MPa.

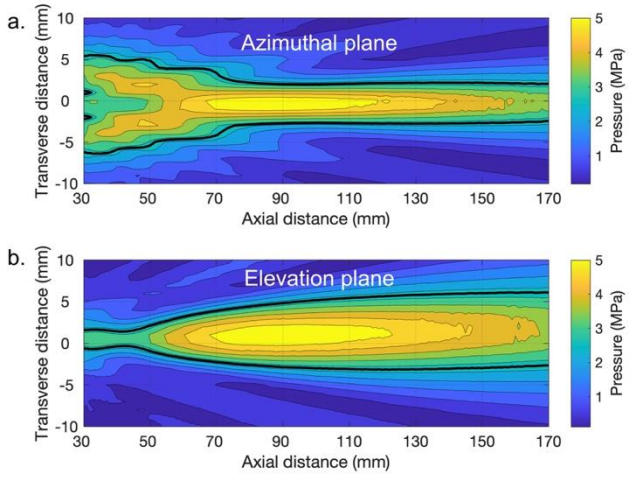

Fig. 6.3: Measured sound field from the S5-1 in the central (a) azimuthal and (b) elevational planes.

The dark line indicates the -6 dB down (half maximum pressure) zone. It can be observed that the focal pressures reached 3.5 MPa at 5 cm, which corresponds to a pressure of about 2.2 MPa, accounting for tissue attenuation.

6.3.2 *Overall safety*

All animals tolerated ultrasound treatment with no adverse clinical signs. Of the eight animals, one animal was euthanized 5 days prior to the study endpoint due to illness unrelated to treatment. From the results of an autopsy performed after euthanasia by UW Veterinarian personnel, it was determined that the pig suffered from bronchopneumonia with pleuritis, consistent with a "shipping fever" not uncommon in pigs following transportation. ALT, AST, ALP and GGT were not shown to significantly vary ($p > 0.05$) either immediately after USCTx or seven days after USCTx as compared to the initial baseline sample (**Fig. 6.4**). Summary statistics (mean ± standard deviation and p-value relative to baseline) can be seen in **Table 6.1**. The blue boxes in **Fig. 6.4** are standard values of pig liver enzymes taken from the Iowa State University Clinical Pathology Reference Intervals (ALP, AST, GGT) and Radostits et al. (ALT) [27]. All liver function enzymes fall within standard ranges, with minor deviations in ALT. No protein content was observed in urine samples. Three animals showed a small degree of blood in their urine, but this was likely due to placement of the bladder catheter given that it was observed both pre- and post-treatment.

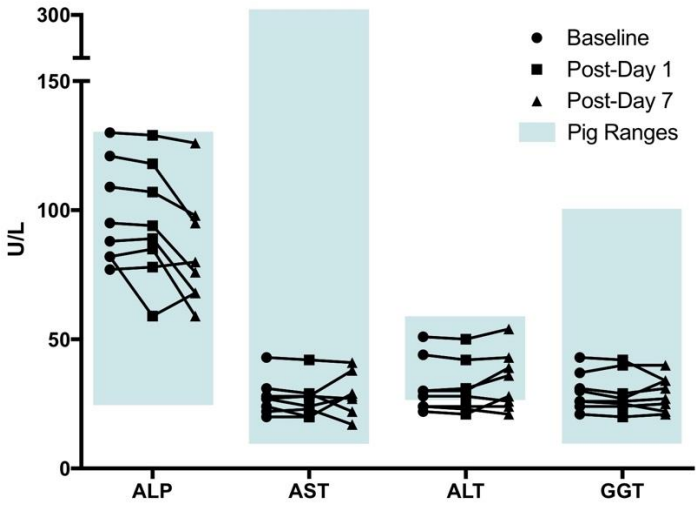

Fig. 6.4: Blood liver enzyme results from before treatment on Day 1, after treatment on Day 1, and 7 days post treatment.

No significant differences were observed ($p > 0.05$). The blue squares indicate ranges taken from the Iowa State University Clinical Pathology Reference Intervals (ALP, AST, GGT) and Radostits et al. (ALT) [27].

Table 6.1: Summary statistics for liver function tests at baseline, post-Day 1, and post-Day 7

	Baseline (U/L)	Post-Day 1 (U/L); *p*-value versus baseline	Post-Day 7 (U/L); *p*-value versus baseline
ALP	98.0 ± 19.8	94.9 ± 22.5; $p = 0.77$	83.8 ± 21.2; $p = 0.19$
AST	27.75 ± 7.1	26.8 ± 7.1; $p = 0.78$	28.9 ± 7.8; $p = 0.77$
ALT	31.6 ± 10.4	31.1 ± 10.0; $p = 0.92$	33.9 ± 11.2; $p = 0.68$
GGT	29.8 ± 7.2	29.1 ± 7.8; $p = 0.87$	29.2 ± 6.6; $p = 0.89$

6.3.3 *CEUS evaluation*

Shown in **Fig. 6.5a** is an example frame from the image intensity analysis performed in MATLAB. The ROI can be seen in both the contrast (bronze color) and fundamental (gray scale) images. The TIC of the contrast data from this example is shown in **Fig. 6.5b**, where RT is calculated as the difference between the start of the bolus to the time of peak enhancement. **Fig. 6.5c** shows RT values from all animals pre-USCTx (teal), immediately post-USCTx (magenta) and one-week post-USCTx (black). There is one missing point one-week post-USCTx which is from the animal that was euthanized prior to Day 7. No significant differences were observed between pre-USCTx

and either immediately post- or 7 days post-USCTx ($p > 0.05$). Summary statistics (mean ± standard deviation and *p*-value relative to baseline) are shown in **Table 6.2**.

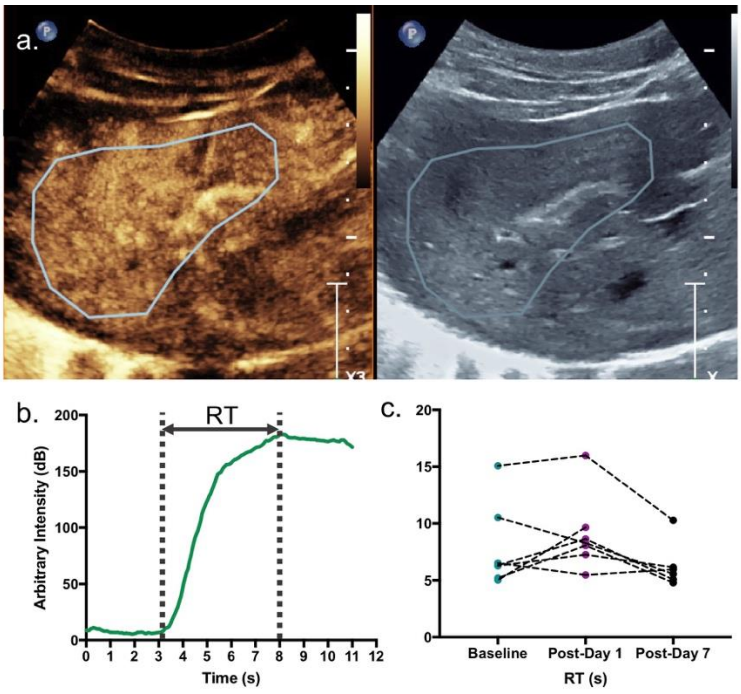

Fig. 6.5: Quantitative CEUS results.

(a) shows a representative DICOM image, with ROI outlined in blue. (b) shows a representative TIC, where RT is defined as the time of peak contrast enhancement minus the start time. (c) shows summary data from all animals. There were no significant differences between pre-USCTx and either immediately post-USCTx or 7 days post-USCTx.

Table 6.2: Summary statistics for rise time at baseline, post-Day 1, and post-Day 7

	Baseline (s)	Post-Day 1 (s); *p*-value versus baseline	Post-Day 7 (s); *p*-value versus baseline
Rise Time (RT)	7.8 ± 3.8	9.1 ± 3.3; $p = 0.22$	6.3 ± 2.0; $p = 0.07$

6.3.4 *Histologic examination*

Fig. 6.6 shows representative H&E stained slides from treated and untreated tissue areas from two different animals. The bottom rows show the regions indicated with the white boxes in the upper rows at higher magnification. No differences were observed between control and treated tissue samples. A variable degree of sinusoidal dilation was observed in both control and treated groups, which we attribute to the frozen preservation technique used in this study.

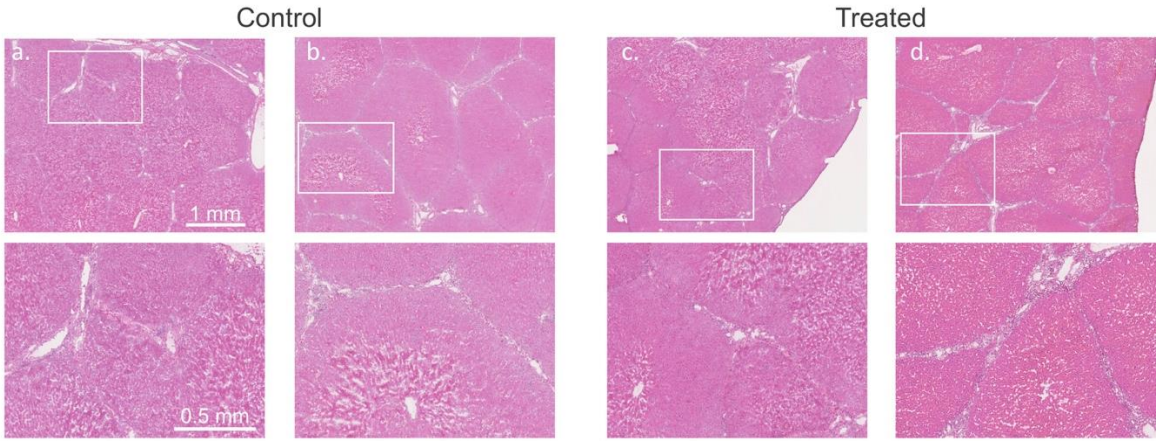

Fig. 6.6: Examples of H&E stained tissue sections from control (a-b) and treated (c-d) liver.

(a) and (c) are from Pig 3, while (b) and (d) are from Pig 4. The white boxes represent the zoomed in images shown in the bottom row. No tissue damage was observed in any slide.

6.4 DISCUSSION

The goal of the present work was to evaluate the safety of ultrasound cavitation treatment (USCTx) using optimized parameters with a clinical scanner in a healthy porcine model as a necessary step for moving to clinical trials. We performed treatments on Day 1 and evaluated health of all animals over the course of the following week. We then performed an acute study to investigate immediate tissue damage due to USCTx. We did not observe any statistically significant changes in blood liver enzymes, microvascular perfusion as measured through CEUS, or H&E stained slides, implying the safety of this technique.

Throughout the duration of the 7-day testing period, there were no observable signs of injury or adverse effects as a result of USCTx. As mentioned, only one of the animals was euthanized prior to the end of the experiment due to pneumonia unrelated to treatment. We also did not observe any significant differences in blood liver enzymes, although for most animals, alkaline phosphatase (ALP) slightly decreased on Day 7. Interestingly, liver damage (including toxicity due to anti-inflammatory drugs such as aspirin and indomethacin used in this study) is generally associated with elevated levels of ALP [28], [29]. That said, the changes between Day 1 and Day 7 are well within the standard range of ALP and were not statistically significant. We observed that the levels of ALT were slightly different than the standard veterinary values, but attribute this to differences

in reference range source (ALT was not provided by the Iowa State University Clinical Pathology values and instead we had to use an alternate source). Indeed, upon consultation with UW Veterinarian Staff, “standard” ranges often include very young animals with elevated enzyme levels, which can unfairly increase average values. Furthermore, ALT is often not even tested in pigs, because the serum blood levels in these animals are usually quite low [30]. Given that the animals were considered healthy on Day 1, the lack of significant relative change indicates no substantial effect of USCTx on liver function. The lack of significant change in liver function tests is consistent with the safety results observed by Eisenbrey et al. [11]. No unusual findings were observed through analysis of urine at any time point, further indicating that no harm was done to the liver as a result of treatment. Finally, previous studies have indicated that premature ventricular contractions (PVCs) are a possible side effect of microbubble imaging [31]. We note that no PVCs were observed in any animal during the study procedure.

In our previous work, we evaluated changes in perfusion as a result of USCTx using a similar acoustic condition [4]. However, in that study, we only observed perfusion changes within the tumor vasculature, and not healthy liver. We hypothesized that the specificity of this effect on tumors was due in part to their unique vascular morphology; where the vasculature of normal liver is well-organized, the vasculature of liver tumors is abnormal and exhibits irregular branching patterns and tortuous geometries [32], [33]. The fragile neovessels of tumors are known to be more vulnerable to cavitation-induced mechanical damage [17], [34]. Furthermore, tumors are fed almost entirely by the hepatic artery [35]. The liver parenchyma fed by the just hepatic artery has been shown in previous work to suffer more intense damage (as compared to the portal vein) as a result of microbubble cavitation within an *ex vivo* perfused liver [36], which could also explain tumor vascular sensitivity. That study also showed insignificant changes in RT as a result of pressures near 2 MPa, even with a much higher duty cycle (8%), suggesting no microvascular damage. Given that we performed these experiments on healthy pigs, it is reasonable to conclude that we did not see perfusion changes in the liver because healthy blood vessels are less sensitive to cavitation bioeffects. This is further confirmed by the lack of acute tissue damage observed through analysis of H&E stained tissue sections.

It is useful also to consider the parameter space used in this study in comparison with other ultrasound cavitation techniques, including histotripsy and sonothrombolysis. Histotripsy utilizes extremely high peak negative pressures, on the order of 10-20 MPa and pulse durations ranging from a single cycle to hundreds of cycles [37], to induce fast focal boiling that may cause mechanical changes in tissue [38] and enhanced drug penetration [39]. In the absence of external cavitation nuclei, high pressures are required for cavitation-induced mechanical effect. On the other hand, the MIs used in the current study are slightly higher than what is used for sonothrombolysis with clinical devices [40], which utilizes MIs on the order of 1.1-1.3 and short pulse durations, both due to scanner limitations and fear of undesired bioeffects, such as endothelial disruption within the heart. These parameters are similar to the current clinical adaptation of ultrasound-mediated drug delivery for abdominal oncology applications [9], [11]. However, as seen in preclinical work, some degree of endothelial disruption is actually desired to facilitate enhanced drug diffusion and/or vascular disruption, and therefore a higher ultrasound dose would be beneficial. Indeed, Goertz, et. al used a focal pressure of 1.65 MPa and 100 cycles for chemotherapy delivery [1] and Di Ianni, et. al used a focal pressure as high as 5.3 MPa and 10 cycles for miRNA delivery [16]. The main concerns in this case are cavitation-induced damage to non-tumorous tissue and vascular disruption limiting drug delivery. For the first, both our results in this study and prior studies have indicated that cavitation damage within the currently studied parameter space of ultrasound-mediated drug delivery is usually constrained to the tumor tissue [17]. For the second, many groups have observed simultaneous vascular disruption and drug penetration [1], [4], [5]. This could possibly be explained by cavitation-induced small pores in the extracellular matrix that reduce interstitial fluid pressure to create more favorable conditions for drug diffusion [8]. Ultimately, the ideal parameter space for ultrasound-mediated drug delivery (excluding cardiology applications) is, in general, somewhere between what is used in histotripsy and what is used in sonothrombolysis.

We acknowledge a few limitations to the study. First, since our goal was to evaluate the safety of USCTx implemented with a clinical scanner, investigating efficacy of drug delivery was beyond the scope of the present work. In addition, we only evaluated USCTx on healthy animals. Although pig tumor models have been previously mentioned [41], they are costly and difficult to establish. However, given that our previous work in mice showed enhanced drug penetration and some

degree of vascular modulation, it is reasonable to conclude that the same effects would be seen in large animals with liver cancer. Furthermore, we implemented the highest transmit voltage available on the ultrasound system, resulting in focal pressures exceeding what is currently allowed on clinical ultrasound scanners for imaging (accounting for attenuation), and still did not see any harm. We also chose to evaluate this technique only in females. This was to ensure a sample size with sufficient statistical power based on our preliminary work [4]. For future clinical approval, a male cohort will need to be tested as well. Finally, despite the premedication regimen used prior to injection of contrast agents, the microbubble supply was qualitatively still less than what is observed during clinical liver CEUS exams due to the pig immune response. We compensated for this by injecting a larger dose of microbubbles, but from our experience, it was still lower than what would typically be seen in humans. That said, the ultrasound dose supplied was still quite high and despite the reduced microbubble supply, the lack of damage observed is still an important finding for validating the safety of this technique.

6.5 CONCLUSION

We evaluated the safety of UltraSound Cavitation Treatment (USCTx) in a large animal model. We performed both a longitudinal safety study (spanning over a week) and an acute safety study using a clinical scanner programmed to produce the following ultrasound conditions: 1.6 MHz transmit frequency, 2.2 MPa focal pressure, and 200 cycles. We did not observe any adverse effects from treatment as measured by analysis of blood liver enzyme levels, quantitative CEUS, and H&E staining. This represents a necessary first safety study in a large animal model assessing microbubble cavitation for treatment of the liver and our results indicate that the treatment regimen is safe within the timeframe evaluated.

6.6 ACKNOWLEDGEMENTS

This work was supported by a grant from the United States Department of Defense (CA160415/PRCRP). We also gratefully acknowledge Dr. Dingjie Suo and Frank (Rusty) Starr as well as the UW Animal Care and Research Facility veterinary staff for their help in performing the animal experiments.

6.7 REFERENCES

[1] D. E. Goertz *et al.*, "Antitumor Effects of Combining Docetaxel (Taxotere) with the Antivascular Action of Ultrasound Stimulated Microbubbles," *PLoS One*, vol. 7, no. 12, p. e52307, Dec. 2012.

[2] C. A. Molina *et al.*, "Microbubble administration accelerates clot lysis during continuous 2-MHz ultrasound monitoring in stroke patients treated with intravenous tissue plasminogen activator.," *Stroke*, vol. 37, no. 2, pp. 425–9, Feb. 2006.

[3] K. Ferrara, R. Pollard, and M. Borden, "Ultrasound Microbubble Contrast Agents: Fundamentals and Application to Gene and Drug Delivery," *Annu. Rev. Biomed. Eng*, vol. 9, pp. 415–47, 2007.

[4] S. B. Keller, D. Suo, Y.-N. Wang, H. Kenerson, R. S. Yeung, and M. A. Averkiou, "Image-Guided Treatment of Primary Liver Cancer in Mice Leads to Vascular Disruption and Increased Drug Penetration," *Front. Pharmacol.*, vol. 11, p. 1526, Sep. 2020.

[5] Y.-J. Ho, T.-C. Wang, C.-H. Fan, and C.-K. Yeh, "Spatially Uniform Tumor Treatment and Drug Penetration by Regulating Ultrasound with Microbubbles," *ACS Appl. Mater. Interfaces*, vol. 10, no. 21, p. acsami.8b05508, May 2018.

[6] S. J. Grainger, J. V. Serna, S. Sunny, Y. Zhou, C. X. Deng, and M. E. H. El-Sayed, "Pulsed Ultrasound Enhances Nanoparticle Penetration into Breast Cancer Spheroids," *Mol. Pharm.*, vol. 7, no. 6, pp. 2006–2019, Dec. 2010.

[7] R. K. Jain and T. Stylianopoulos, *Delivering nanomedicine to solid tumors*, vol. 7, no. 11. Nature Publishing Group, 2010, pp. 653–664.

[8] A. Mohammadabadi *et al.*, "Pulsed focused ultrasound lowers interstitial fluid pressure and increases nanoparticle delivery and penetration in head and neck squamous cell carcinoma xenograft tumors," *Phys. Med. Biol.*, vol. 65, no. 12, p. 125017, Jun. 2020.

[9] G. Dimcevski *et al.*, "A human clinical trial using ultrasound and microbubbles to enhance gemcitabine treatment of inoperable pancreatic cancer," *J. Control. Release*, vol. 243, pp. 172–181, Dec. 2016.

[10] L. Huang *et al.*, "Efficacy and safety of high-intensity focused ultrasound ablation for hepatocellular carcinoma by changing the acoustic environment: microbubble contrast agent (SonoVue) and transcatheter arterial chemoembolization," *Int. J. Hyperth.*, vol. 36, no. 1, pp. 243–251, Jan. 2019.

[11] J. R. Eisenbrey *et al.*, "US-triggered Microbubble Destruction for Augmenting Hepatocellular Carcinoma Response to Transarterial Radioembolization: A Randomized Pilot Clinical Trial," *Radiology*, vol. 298, no. 2, pp. 450–457, Feb. 2021.

[12] T. van Rooij *et al.*, "Viability of endothelial cells after ultrasound-mediated sonoporation: Influence of targeting, oscillation, and displacement of microbubbles," *J. Control. Release*, vol. 238, pp. 197–211, 2016.

[13] N. McDannold, C. D. Arvanitis, N. Vykhodtseva, and M. S. Livingstone, "Temporary Disruption of the Blood-Brain Barrier by Use of Ultrasound and Microbubbles: Safety and Efficacy Evaluation in Rhesus Macaques," *Cancer Res.*, vol. 72, no. 14, pp. 3652–3663, Jul. 2012.

[14] M. E. Downs *et al.*, "Long-Term Safety of Repeated Blood-Brain Barrier Opening via Focused Ultrasound with Microbubbles in Non-Human Primates Performing a Cognitive Task," *PLoS One*, vol. 10, no. 5, p. e0125911, May 2015.

[15] T. Mainprize *et al.*, "Blood-Brain Barrier Opening in Primary Brain Tumors with Non-

invasive MR-Guided Focused Ultrasound: A Clinical Safety and Feasibility Study," *Sci. Rep.*, vol. 9, no. 1, p. 321, Dec. 2019.
[16] T. Di Ianni *et al.*, "Ultrasound/microbubble-mediated targeted delivery of anticancer microRNA-loaded nanoparticles to deep tissues in pigs," *J. Control. Release*, vol. 309, pp. 1–10, Sep. 2019.
[17] J. Wang *et al.*, "Selective depletion of tumor neovasculature by microbubble destruction with appropriate ultrasound pressure," *Int. J. Cancer*, vol. 137, no. 10, pp. 2478–2491, Nov. 2015.
[18] Z. Liu *et al.*, "Disruption of tumor neovasculature by microbubble enhanced ultrasound: A potential new physical therapy of anti-angiogenesis," *Ultrasound Med. Biol.*, vol. 38, no. 2, pp. 253–261, Feb. 2012.
[19] J. Øistensen, R. Hede, Y. Myreng, T. Ege, and E. Holtz, "Intravenous injection of Albunex R microspheres causes thromboxane mediated pulmonary hypertension in pigs, but not in monkeys or rabbits," *Acta Physiol. Scand.*, vol. 144, no. 3, pp. 307–315, Mar. 1992.
[20] J. H. Nederhoed, J. Slikkerveer, K. W. Meyer, W. Wisselink, R. J. P. Musters, and K. K. Yeung, "Contrast-enhanced sonothrombolysis in a porcine model of acute peripheral arterial thrombosis and prevention of anaphylactic shock," *Lab Anim. (NY).*, vol. 43, no. 3, pp. 91–94, Mar. 2014.
[21] J. P. Kilroy, A. H. Dhanaliwala, B. R. Wamhoff, A. L. Klibanov, D. K. Bowles, and J. A. Hossack, "Neointima reduction with IVUS and rapamycin microbubbles: In Vivo swine model results," in *2014 IEEE International Ultrasonics Symposium*, 2014, pp. 13–16.
[22] H. Wang *et al.*, "Quantitative Assessment of Inflammation in a Porcine Acute Terminal Ileitis Model: US with a Molecularly Targeted Contrast Agent.," *Radiology*, vol. 276, no. 3, pp. 809–17, Sep. 2015.
[23] C. F. Dietrich, M. A. Averkiou, J.-M. M. Correas, N. Lassau, E. Leen, and F. Piscaglia, "An EFSUMB introduction into dynamic contrast-enhanced ultrasound (DCE-US) for quantification of tumour perfusion," *Ultraschall der Medizin*, vol. 33, no. 4, pp. 344–351, Aug. 2012.
[24] C. Strouthos, M. Lampaskis, V. Sboros, A. Mcneilly, and M. Averkiou, "Indicator dilution models for the quantification of microvascular blood flow with bolus administration of ultrasound contrast agents," *IEEE Trans. Ultrason. Ferroelectr. Freq. Control*, vol. 57, no. 6, pp. 1296–1310, Jun. 2010.
[25] M. A. Averkiou *et al.*, "Evaluation of the Reproducibility of Bolus Transit Quantification With Contrast-Enhanced Ultrasound Across Multiple Scanners and Analysis Software Packages—A Quantitative Imaging Biomarker Alliance Study," *Invest. Radiol.*, vol. 55, no. 10, pp. 643–656, Oct. 2020.
[26] F. A. Duck, *Physical properties of tissue : a comprehensive reference book*. Academic Press, 1990.
[27] O. M. Radostits, C. C. Gay, D. C. Blood, and K. W. Hinchcliff, *Veterinary medicine: a textbook of the diseases of cattle, sheep, pigs, goats, and horses*, 9th Editio. W.B. Saunders Company Ltd, 2000.
[28] D. H. Vroon and Z. Israili, *Alkaline Phosphatase and Gamma Glutamyltransferase*. Butterworths, 1990.
[29] H. J. Zimmerman, "Effects of Aspirin and Acetaminophen on the Liver," *Arch. Intern. Med.*, vol. 141, no. 3, pp. 333–342, Feb. 1981.

[30] K. S. Latimer, *Duncan and Prasse's Veterinary Laboratory Medicine Clinical Pathology 5th Edition*. 2011.
[31] P. A. van der Wouw, A. C. Brauns, S. E. Bailey, J. E. Powers, and A. A. A. Wilde, "Premature Ventricular Contractions During Triggered Imaging with Ultrasound Contrast," *J. Am. Soc. Echocardiogr.*, vol. 13, no. 4, pp. 288–294, Apr. 2000.
[32] D. Fukumura and R. K. Jain, "Tumor microvasculature and microenvironment: Targets for anti-angiogenesis and normalization," *Microvasc. Res.*, vol. 74, no. 2–3, pp. 72–84, Sep. 2007.
[33] D. Semela and J. F. Dufour, "Angiogenesis and hepatocellular carcinoma," *Journal of Hepatology*, vol. 41, no. 5. pp. 864–880, Nov-2004.
[34] J. H. Hwang, A. A. Brayman, M. A. Reidy, T. J. Matula, M. B. Kimmey, and L. A. Crum, "Vascular effects induced by combined 1-MHz ultrasound and microbubble contrast agent treatments in vivo," *Ultrasound Med. Biol.*, vol. 31, no. 4, pp. 553–564, Apr. 2005.
[35] A. Rammohan *et al.*, "Embolization of liver tumors: Past, present and future.," *World J. Radiol.*, vol. 4, no. 9, pp. 405–12, Sep. 2012.
[36] C. P. Keravnou, I. De Cock, I. Lentacker, M. L. Izamis, and M. A. Averkiou, "Microvascular Injury and Perfusion Changes Induced by Ultrasound and Microbubbles in a Machine-Perfused Pig Liver," *Ultrasound Med. Biol.*, vol. 42, no. 11, pp. 2676–2686, 2016.
[37] K. B. Bader, E. Vlaisavljevich, and A. D. Maxwell, "For Whom the Bubble Grows: Physical Principles of Bubble Nucleation and Dynamics in Histotripsy Ultrasound Therapy," *Ultrasound in Medicine and Biology*, vol. 45, no. 5. Elsevier USA, pp. 1056–1080, 01-May-2019.
[38] E. Vlaisavljevich, Z. Xu, A. Arvidson, L. Jin, W. Roberts, and C. Cain, "Effects of Thermal Preconditioning on Tissue Susceptibility to Histotripsy.," *Ultrasound Med. Biol.*, vol. 41, no. 11, pp. 2938–54, Nov. 2015.
[39] T. Li *et al.*, "Pulsed high-intensity focused ultrasound enhances delivery of doxorubicin in a preclinical model of pancreatic cancer," *Cancer Res.*, vol. 75, no. 18, pp. 3738–3746, Sep. 2015.
[40] W. Mathias *et al.*, "Sonothrombolysis in ST-Segment Elevation Myocardial Infarction Treated With Primary Percutaneous Coronary Intervention," *J. Am. Coll. Cardiol.*, vol. 73, no. 22, pp. 2832–2842, Jun. 2019.
[41] X. Li, X. Zhou, Y. Guan, Y.-X. J. Wang, D. Scutt, and Q.-Y. Gong, "N-nitrosodiethylamine-induced pig liver hepatocellular carcinoma model: radiological and histopathological studies.," *Cardiovasc. Intervent. Radiol.*, vol. 29, no. 3, pp. 420–8, 2006.

Chapter 7. CONCLUSIONS

7.1 SUMMARY

The challenge of targeted and efficient drug delivery to solid tumors can be partly attributed to the unique tumor microenvironment that constitutes a major barrier to drug delivery. Many solid tumors show irregular vascular architecture, desmoplasia within the extracellular matrix, and increased stiffness and interstitial fluid pressure, all of which are associated with reduced drug efficacy. Ultrasound-mediated cavitation from microbubbles has been investigated in this body of work as a method of image-guided therapy to solid tumors, in which the same tools (ultrasound and microbubbles) used to localize a lesion can also be used for treatment and subsequent monitoring. We chose to evaluate ultrasound-mediated drug delivery in a "grounds up" approach, beginning with an evaluation of microbubble dynamics during therapy and imaging and leading to preclinical efficacy and safety studies. The use of a clinical ultrasound system and commercial contrast agents throughout this work will enable future translation efforts, further explained below.

When microbubbles experience an acoustic wave, they undergo volumetric oscillations. These oscillations result in nonlinear echoes that can be detected by an ultrasound system. Depending on the desired therapeutic outcome, different types of cavitation, stable or inertial, may be preferred, and therefore it is useful to monitor cavitation frequency activity in real time. The first goal of this work was to characterize the behavior of commercial microbubbles during therapy. This was done using cavitation detection of common commercial formulations in bulk solution using a single element receiver and an array receiver. We quantified inertial cavitation thresholds using two previously reported techniques and one that we developed. We found the specific frequency content of different microbubble formulations oscillating stably or inertially. The spectral signatures of these microbubble formulations, despite being similar overall, still exhibited a variable degree of uniqueness that could be utilized in characterization studies. We then utilized this information to implement cavitation detection on a diagnostic ultrasound device and were able to observe inertial cavitation in real time. The simplicity of this technique could enable rapid adoption of real-time cavitation monitoring in the clinic.

Next, we investigated microbubble dynamics during contrast-enhanced ultrasound imaging, and specifically the phase response of commercial microbubbles during amplitude modulation. Segmentation based on phase information from microbubble echoes is currently being investigated as a method of increasing contrast in contrast-enhanced ultrasound images. We defined the phase difference between the echoes from the full and half amplitude pulses of amplitude modulation as $\Delta\Phi_{AM}$, which refers to the phase of the echo of the full amplitude pulse minus the phase of the echo of the half amplitude pulse. We first investigated $\Delta\Phi_{AM}$ through microbubble dynamics simulations. We observed that both shelled and unshelled microbubbles produce a noticeably negative $\Delta\Phi_{AM}$. However, where the $\Delta\Phi_{AM}$ of unshelled microbubbles was mostly dependent on pressure amplitude, the $\Delta\Phi_{AM}$ of shelled microbubbles was mostly dependent on size and was in fact generally more pronounced at lower pressures. Using simulations of nonlinear propagation of ultrasound, we found that tissue also generates a small $\Delta\Phi_{AM}$ during amplitude modulation at high acoustic amplitudes (but still within FDA limits) which suggests the possibility of nonlinear echo segmentation based on phase during tissue harmonic imaging. Furthermore, although low, the presence of phase difference in tissue has a strong implication on parameter selection for optimal segmentation based on echo phase. We then validated our results with *in vitro* experiments and found that all commercial contrast agents exhibited a negative $\Delta\Phi_{AM}$, confirming the theoretical work. Similar to the cavitation work, $\Delta\Phi_{AM}$ was similar between all contrast agents, with some slight deviations that could be attributed to differences in size and composition.

We then evaluated microbubble activity during sonoporation pulse sequences in common *in vitro* cell enclosures. Traditionally, therapeutic ultrasound was hypothesized to enhance drug delivery through "sonoporation", defined as the creation of pores in cell membranes due to ultrasound-induced microbubble oscillations. To evaluate these mechanisms, it was standard to use small, water-tight enclosures seeded with cancer or endothelial cells, in which microbubbles were then added and the whole system was exposed to ultrasound. We fully characterized the resulting acoustic environment in these "cell enclosures" during typical (from parameters suggested in literature) sonoporation pulse sequences. We observed that the propagation of ultrasound through a bulk solution of microbubbles within cell enclosures created a complex acoustic environment that was a result of spatially and temporally varying acoustic fields and bubble concentrations. We concluded that the confounding environment and transient spatiotemporal bubble and pressure

variations within these cell enclosures would make it challenging to study sonoporation in a standardized and reproducible way because microbubble oscillation near cells is very likely not the dominant mechanism in this scenario. Although the use of cell enclosures continues to be an active area of research in other groups, we decided that the use of more realistic models would be a more relevant testbed for our work.

Finally, we utilized the knowledge gained from observing microbubble behavior through spectral analysis and imaging to evaluate acute efficacy and safety of image-guided cavitation treatment *in vivo*. We began with an acute efficacy study of ultrasound cavitation treatment in a genetically engineered mouse model of hepatocellular carcinoma. To facilitate translation, we adapted a clinical ultrasound device into a focused beam for therapy. We observed that there were significant and immediate perfusion changes following ultrasound cavitation treatment in the tumors of mice. Interestingly, these effects were specific to the tumor and did not occur in healthy tissue, implying an inherent vulnerability in the tumor microvasculature that could be exploited as a therapeutic target. We also observed concurrent drug penetration. These outcomes were perceived as contradictory at first but were hypothesized to be a result of an interaction with the tumor microenvironment and/or a reduction in tumor interstitial fluid pressure. Since we hope to eventually move this to clinical practice, we then performed both a longitudinal safety study (spanning over a week) and an acute safety study of this treatment in healthy pigs. Although there exist clinical studies utilizing microbubble cavitation for drug delivery, we noted that these studies have primarily used normal imaging modes for therapy instead of the higher intensity ultrasound parameters used in successful preclinical work. This is because the required safety evaluations for adapting these parameters have not been performed. When we applied our optimized ultrasound settings to the livers of healthy pigs, we did not observe any adverse effects from treatment as measured by analysis of blood and urine, quantitative CEUS, and H&E staining. We concluded that this treatment is safe within the timeframe evaluated.

With the increasing prevalence and global burden of cancer, the development of novel technologies will be of high economic and clinical value. We have investigated many aspects of image-guided therapy for cancer treatment, from microbubble cavitation dynamics and detection to preclinical safety and efficacy. We have adapted tools that are readily available in hospitals to

perform this work. First, we modified a standard abdominal imaging probe to be a tool for real-time cavitation detection and characterized the cavitation characteristics of several commercial microbubbles. We then measured the phase change of microbubbles with a clinical device with the eventual goal of implementing phase segmentation. Finally, we modified a phased array probe to be a tool for enhanced drug delivery. Collectively, we hope that the outcomes from this work enable clinical translation of ultrasound-mediated drug delivery to improve chemotherapy outcomes.

7.2 FUTURE DIRECTIONS

There are several interesting investigations that could stem from the outcome of this work. First, we confirmed that we could optimize a clinical ultrasound device to be a real-time inertial cavitation detector; however, it would be necessary to evaluate this technique in a more realistic model before moving to clinical implementation. We have expertise in *ex vivo* machine-perfused pig liver experiments, which would be an ideal testbed for evaluating real-time inertial cavitation detection during therapy. Another exciting avenue for the inertial cavitation threshold work would be to evaluate cavitation signatures in various biologically relevant environments, such as the high-pressure tumor microenvironment. Establishing differences in cavitation response as a result of pressure could inform better diagnostic methods of evaluating interstitial fluid pressure in real time as a therapy monitoring tool.

Secondly, although we were able to evaluate the parameters required for effective $\Delta\Phi_{AM}$ through microbubble dynamics and nonlinear propagation simulations, the logical next step would be to implement these findings during imaging. One outcome that we found from the inertial cavitation work was that Sonazoid had a higher inertial cavitation threshold than the other microbubbles, which means that it provides better signal at higher ultrasound pressures. These higher ultrasound pressures could in theory result in nonlinear propagation. It would therefore be interesting to evaluate bubble segmentation based on phase using this particular microbubble to improve the CTR. Secondly, since $\Delta\Phi_{AM}$ had a strong dependence on microbubble size, evaluating phase segmentation in monodisperse microbubble populations could be an interesting validation of our simulation work and could also improve parameter selection for segmentation based on phase. Finally, we theorized that segmentation based on phase could be used for tissue harmonic imaging

at high mechanical indexes. It would be interesting to evaluate the amount of linear signal cancellation using phase segmentation for tissue harmonic imaging.

The exciting results from our murine efficacy study indicated that we caused immediate vascular change and concurrent drug penetration due to ultrasound cavitation treatment. Although encouraging, we were unable to determine the exact mechanisms for these phenomena. It would be of high importance to follow up this work with both a longitudinal survival study and a longer-term efficacy study to determine the duration of vascular damage. The use of interstitial fluid pressure measurements either through the use of pressure catheters inserted into the tumor, pressure-based cavitation detection as described above, or shear wave elastography would help explain biological mechanisms. Concurrently, the use of super-resolution imaging techniques performed before and after therapy would be an extremely interesting addition to the standard contrast-enhanced ultrasound imaging already performed. Through the use of novel Doppler processing, we could possibly separate out microvascular structure based on flow velocities, which could provide information on vascular sensitivity as a result of therapy. Further, we could evaluate other "mechanomodulating" drugs in addition to cavitation treatment and chemotherapy. This could potentially be used as an augmentation of the mechanomodulatory effects of microbubble cavitation. Finally, a long-term survival study could allow us to optimize therapeutic ultrasound parameters and drug dosing for maximally effective therapy.

7.3 LIST OF PUBLICATIONS AND PRESENTATIONS

Peer-reviewed publications

1. **Keller, SB,** Lai, TY, Averkiou, MA. "Investigation of the phase of the fundamental component of nonlinear echoes during amplitude modulation." *[in prep]*
    - Chapter 3
2. **Keller, SB,** Averkiou, MA. "The Role of Ultrasound in Modulating Interstitial Fluid Pressure in Solid Tumors for Improved Drug Delivery." *[in review]*
3. **Keller, SB,** Wang, Y-N, Totten, S, Yeung, RS, Averkiou, MA. "Safety of image-guided treatment of the liver with ultrasound and microbubbles in an *in vivo* porcine model." *[accepted] Ultrasound Med. Biol.* 2021
    - Chapter 6

4. **Keller, SB,** Sheeran, PS, Averkiou, MA. "Cavitation therapy monitoring of commercial microbubbles with a clinical scanner." *IEEE Trans Ultrason Ferroelectr Freq Control*, 2021 Apr;68(4):1144-1154
    - Chapter 2
5. **Keller, SB,** Suo, D, Wang, Y-N, Kenerson, H, Yeung, RS, Averkiou, MA. "Image-Guided Treatment of Primary Liver Cancer in Mice Leads to Vascular Disruption and Increased Drug Penetration." *Front. Pharmacol.* 11:584344. doi: 10.3389/fphar.2020.584344
    - Chapter 5
6. **Keller, SB**, Bruce, M, Averkiou, MA. "Ultrasound Imaging of Microbubble Activity During Sonoporation Pulse Sequences." *Ultrasound Med. Biol.* 2019 Mar;45(3):833-45
    - Chapter 4
7. Juang, E, De Cock, I, Keravnou, C, Gallagher, M, **Keller, SB**, Zheng, Y, Averkiou, MA. "Engineered 3D microvascular networks for the study of sonoporation and ultrasound-microbubble-mediated drug delivery." *Langmuir* 2019;35:10128-10138

<u>Presentations at national and international conferences</u>

1. **Keller, SB,** Wang, Y-N, Suo, D, Yeung, RS, Averkiou, MA. "Safety of image-guided ultrasound cavitation treatment for liver cancer in an *in vivo* porcine model." 26th European Symposium on Ultrasound Contrast Imaging (poster presentation)

2. **Keller, SB,** Suo, D, Wang, Y-N, Kenerson, H, Yeung, RS, Averkiou, MA. "Vascular disruption and enhanced drug penetration performed in a mouse model of hepatocellular carcinoma with a clinical scanner." 25th European Symposium on Ultrasound Contrast Imaging (poster presentation)

3. **Keller, SB,** Sheeran, PS, Averkiou, MA. "Cavitation therapy monitoring of commercial microbubbles with a clinical scanner." 25th European Symposium on Ultrasound Contrast Imaging (poster presentation, *best poster award*)

4. **Keller, SB,** Suo, D, Wang, Y-N, Kenerson, H, Yeung, RS, Averkiou, MA. "Vascular disruption and enhanced drug penetration performed in a mouse model of hepatocellular carcinoma with a clinical scanner." 2019 International Ultrasonics Symposium (poster presentation)

5. **Keller, SB,** Bruce, M, Averkiou, MA. "High Resolution Ultrafast Imaging of Microbubble Destruction During Sonoporation" 23rd European Symposium on Ultrasound Contrast Imaging (poster presentation, *best poster award*)

6. **Keller, SB**, Zong, R, Hannah, A, Bruce, M, Averkiou, MA. "High Resolution Ultrafast Imaging of Microbubble Destruction During Sonoporation" IEEE International Ultrasonics Symposium 2017 (poster presentation)